

Aus dem Institut für Transfusionsmedizin und Immunologie
der Medizinischen Fakultät Mannheim
(Direktor: Prof. Dr. med. Harald Klüter)

Flow Cytomorphometry for Assessment of Red Blood Cell Storage Lesion

Inauguraldissertation
zur Erlangung des akademischen Grades Doctor scientiarum humanarum (Dr.sc.hum.)
der
Medizinischen Fakultät Mannheim
der Ruprecht-Karls-Universität
zu
Heidelberg

vorgelegt von
Diego Andrés Sierra Fajardo

Aus
Bogotá, Kolumbien
2016

Dean: Prof. Dr. Sergij Goerdts

Advisor: Prof. Dr. rer. nat. Karen Bieback

TABLE OF CONTENTS

ABREVIATIONS.....	1
1 INTRODUCTION	4
1.1 Red Blood Cells	4
1.2 Red Cell Storage and Storage Lesion	6
1.3 Morphometric Analysis of RBCs	8
1.4 In situ Microscope	9
1.5 Aim of the Study	11
2 MATERIALS AND METHODS	13
2.1 Materials.....	13
2.1.1 Devices, Accessories and Substances.....	13
2.2 RBC Morphometry with in situ Microcopy.....	14
2.2.1 Fluidic Principle.....	14
2.2.2 Flow Dynamics: laminar Flow and Shear Stress	15
2.2.3 In situ Microscope Setup	17
2.2.4 Mechanical Adaptation of in situ Microscopy to Flow Cytomorphometry	18
2.2.5 Image Filtering for Recognition of sharp Objects.....	19
2.3 Software Platform	20
2.3.1 ISM Viewer	20
2.3.2 MATLAB	21
2.4 Blood Collection and Storage	21
2.4.1 Sample Preparation, morphological and biochemical Assessment.	22
2.5 Morphological Categorization of RBCs.....	22
3 RESULTS.....	23
3.1 Setup for Flow Morphometry of RBCs	23
3.2 Housing Design and Component Assembly.....	23
3.3 Fluidic Operation	27
3.4 Discocyte Orientation: optimal Flow Rate and focal Plane Height	29
3.5 RBC Morphology Categorization and morphological Features	33
3.6 Algorithm Development.....	35
3.6.1 Cell Segmentation	35
3.6.2 Feature Extraction	46
3.6.3 Classification.....	55
3.7 Monitoring of RBC Units.....	60
3.7.1 Percentage of Echinocytes, Spherocytes and morphological Index over Time.....	60

3.7.2	Donor Group 1.....	62
3.7.3	Donor Group 2.....	66
3.7.4	Donor Group 3.....	69
3.7.5	Inter-Group Correlation between Morphological and biochemical Assessments	71
3.7.6	Estimation of Hemolysis through morphometric Assessment.....	73
3.7.7	Morphological Response of RBCs to Heat Damage.....	78
3.8	Statistical Uncertainty	80
3.8.1	Measurement Variability.....	80
3.8.2	Number of analyzed RBCs for Data Point Generation.....	82
4	DISCUSSION	85
4.1	Physical Operation of the System	85
4.2	Flow Conditions and RBC Imaging.....	87
4.3	Image Capture and Processing Time	89
4.4	Image Processing and RBC Classification	90
4.5	Sample Preparation	92
4.6	Monitoring of RBC Units.....	93
5	SUMMARY	96
6	REFERENCES	98
7	APPENDIX	103
8	CURRICULUM VITAE	119
9	ACKNOWLEDGMENTS	121

ABREVIATIONS

A	Area
AS	Additive Solution
ATP	Adenosine 5-triphosphate
b	Channel Width
BR	Border Roughness
BSA	Bovine Serum Albumin
C	Cell Border Point
°C	Grad Celsius
CAD	Computer-Aided Design
CCD	Charge-Coupled Device
CFUE	Erythroid Colony-Forming-Units
cm	Centimeter
CO₂	Carbon dioxide
CPD	Citrate Phosphate Dextrose
3D	Three Dimensional
D	Discocyte
DEHP	Diethyl-Hexyl Phthalate
dl	Deciliter
DOF	Depth of Field
dyn	Dyne
E	Echinocyte
E I	Echinocyte type 1
E II	Echinocyte type 2
E III	Echinocyte type 3
ED	Equivalent Diameter
EN	Entropy
F	Flow rate
FD	Fourier Descriptor
F-MFCs	First Medium Frequency Components
fps	Frames per Second
FUE	Erythroid Forming Units
g	Gramm
G	3x3 Pixel Region
Gy	Gray
h	Channel height
H	Hemolysis
Hb	Hemoglobin
HFC	High Frequency Component

HSC	Hematopoietic Stem Cell
Hz	Herz
I_{AVR}	Average Image
I_B	Binary Image
I_{BG}	Background Image
I_{COM}	Brightness-Compensated Image
I_{DIV}	Division Image
I_{HP}	High-Pass Filtered Image
I_{IN}	Input Image
I_{LP}	Low-Pass Filtered Image
I_{SC}	Scaled Image
I_{TH}	Binary Image after High Thresholding
I_{TL}	Binary Image after Low Thresholding
ISM	In Situ Microscope
l	Liter
LED	Light-Emitting Diode
LFC	Low Frequency Component
L-MFCs	Last Medium Frequency Components
LPG	Light Pulse Generator
μl	Microliter
μm	Micrometer
ml	Milliliter
mm	Milimeter
min	Minute
mOsm	Milliosmole
M	Gray-Scale Cell Micrograph
M_B	Binary Cell Micrograph after Thresholding
M_E	Entropy Cell Micrograph
M_K	Binary Cell Micrograph after Morphological Operations
M_{LP}	Low-Pass Filtered Cell Micrograph
M_H	Binary Cell Micrograph after Contour Fitting
M_{HP}	High-Pass Filtered Micrograph
M_{TI}	Entropy-Masked Cell Micrograph
M_V	Variance Micrograph
MFC	Medium Frequency Component
MI	Morphological Index
NC	Non-Circularity
O₂	Oxygen
pO₂	Partial Pressure of Oxygen
PVC	Polyvinyl Chloride
r	Radius
R	Interval of Radial Distances
RBC	Red Blood Cell
RCC	Red Cell Concentrate

Re	Reynolds Number
RNA	Ribonucleic Acid
rRNA	Ribosomal Ribonucleic Acid
rpm	Revolutions per Minute
rps	Revolutions per Second
S	Spherocyte
SD	Standard Deviation
SE	Sphero-Echinocyte
SAGM	Saline-Adenine Glucose Mannitol
SMA	Subminiature Version A
τ	Shear Stress
γ	Shear Rate
T	Texture Inhomogeneity
T_{ED}	Equivalent Diameter Threshold
v	Mean Flow Velocity
w	Channel Width
WBC	White Blood Cell
xor	Exclusive OR

1 INTRODUCTION

1.1 Red Blood Cells

The main function of the circulatory system is the transport of substances through the body. One of the most important processes is the transport of oxygen (O_2) to the organs and tissues and the return transport of carbon dioxide (CO_2) to the lungs through the blood stream [1]. The blood consists of plasma (~55%), erythrocytes or red blood cells (RBCs) (~45%), white blood cells and platelets (<1%). Oxygen (O_2) has a low solubility in water and therefore only 2% of the O_2 is carried in the plasma and RBC water [1]. Almost all of the O_2 circulating through the body is carried by the protein hemoglobin (Hb) contained within the RBCs [1]. The hemoglobin molecules bind the O_2 as RBCs pass through the lungs to be released to the tissues. One molecule of hemoglobin can bind up to four molecules of oxygen (oxyhemoglobin) and this carrying capacity is associated with the oxyhemoglobin dissociation curves that describe the loading and unloading of O_2 [2]. This occurs at high partial pressure of O_2 (pO_2) in the lungs and low pO_2 in the microcirculation, respectively [2].

Around 10 trillion erythrocytes are produced in the human body every day. This process is called erythropoiesis and starts in the hematopoietic stem cells (HSCs) [3, 4]. The maturation of erythrocytes occurs through cell differentiation in the bone marrow, where HSCs undergo a succession of transformations (erythropoiesis stages). The erythropoiesis begins with the transformation of HSCs into precursor cells (erythroid burst forming units – BFU-E and subsequently erythroid colony forming units – CFU-E). In this stage, the protein hormone erythropoietin stimulates the differentiation of these cells into erythroid precursor cells (erythroid pronormoblasts and subsequent normoblasts). Around 90% of this hormone is produced in the interstitial cells of the kidney and 10% in the liver and other organs. From the pronormoblasts, a sequence of progressively smaller normoblasts are formed through cell division. They contain an increasing amount of hemoglobin in the cytoplasm, which reaches around 65 % of the total synthesized hemoglobin before the cell nucleus is expelled. In the final phase of transformation in the bone marrow, the last normoblasts expel the nucleus, resulting in reticulocytes that still contain ribosomal ribonucleic acid (rRNA) and can still synthesize hemoglobin. Reticulocytes are slightly larger than mature erythrocytes and remain in the bone marrow for two or three days and then they enter the blood stream, where the remaining RNA disappears. As result, reddish-pink colored erythrocytes without nucleus are formed. From one individual pronormoblast, 16 mature erythrocytes are usually produced. Erythropoiesis is permanently regulated by the hormone erythropoietin. In case of reduction of the O_2 levels, the

kidney increases the production of erythropoietin which elevates the production of erythrocytes and consequently the O₂ levels.

Erythrocytes exhibit a biconcave disc shape (average diameter of 7.5 µm and 3 µm thickness). One of the principal characteristics is their deformability, which is associated with several factors such as membrane elasticity, internal viscosity and a high area/volume ratio [5]. This deformability allows erythrocytes to navigate through small capillaries of up to 3µm diameter to deliver O₂ to the tissues. The normal erythrocyte concentration in blood ranges between 4.5 - 6.2 million per microliter in adult males and 4 - 5.5 million per microliter in adult females. The Hb concentration ranges about 14-19 g/dl and 12-16 g/dl, respectively. Red blood cells circulate for about 120 days before being removed from circulation by macrophages located predominantly in the spleen and liver.

The appropriate oxygenation of the tissues depends on the Hb concentration and the saturation affinity of Hb [6]. For this reason, red blood cells are transfused upon blood loss during surgeries or in certain medical conditions (e.g. anemia) to increase the hemoglobin levels or carrying capacity of oxygen and therefore, prevent the hypoxia of the tissues [6]. Around 85 million of RBC units are transfused worldwide every year [7]. The criterion for RBC transfusion is not only based on a specific hemoglobin concentration or hematocrit threshold. Various clinical guidelines recommend considering the patient's clinical conditions and symptoms [7]. This strategy is intended to improve the treatment outcomes and avoid unnecessary RBC transfusions that increase the risk of possible post transfusion complications [7].

In vitro generation of erythrocytes derived from hematopoietic cells is theoretically possible [8]. However, the high required volumes of cells to supply the current demand and the associated costs do not make this method a viable solution up to now [8]. Therefore, blood donation and the subsequent storage constitutes the only effective source of erythrocytes for transfusion until the present. RBC infusion can be life-saving, however there has been discussion regarding when to transfuse (transfusion trigger) to minimize side effects [9] and the impact of the duration of storage and thus age on RBC quality [10]. Currently, there is no consensus on the side effects associated with red cell transfusion and there is still not enough evidence that supports this findings [11]. However, a correlation between mortality and the age of the transfused RBCs has been previously shown [12] as well as the incidence of pneumonia and acute lung injury after transfusion of older RBCs [13, 14]. Moreover, multiple organ failure in trauma patients has also been related to the duration of the storage of transfused RBCs [15]. The adverse effects of larger transfusions and older RBCs on the immune system has also been linked to a decreased immune defense due to the clearing of nonfunctional erythrocytes

[16]. Considering the above, the functional alterations of transfused RBCs suggest the benefit of preventing their deterioration and hence, improving their quality prior to transfusion [17].

1.2 Red Cell Storage and Storage Lesion

The preservation technique of stored red blood cells (RBCs) has progressively evolved during the last century, giving rise to a regulated standard for blood banks at a global level [8]. This progress has mainly been focused on the development of storage solutions that are intended to maintain the metabolic functions of the cells during the hypothermic storage, increasing the *in vivo* recovery fraction of RBCs and minimizing the patient complications after transfusion [17]. Nowadays, whole blood is mainly collected into citrate phosphate dextrose (CPD) solution; this is an anticoagulant with a mixture of glucose and phosphate that supports the red cell metabolism and improves the pH for the maintenance of 2,3-DPG levels [18]. Additional mixtures of nutrients have been developed to provide longer storage and protection to the cell membrane. The most used additive solution in Europe is saline-adenine glucose mannitol (SAGM). The adenine of this formulation slows the adenosine 5-triphosphate (ATP) depletion in stored RBCs and the mannitol acts as a membrane stabilizer, reducing the hemolysis [19-21].

Other advances include improvements of the material composition of the plastic bags, which is a combination of polyvinyl chloride (PVC) and commonly diethyl-hexyl phthalate (DEHP) as plasticizer. This latter was found to enter in the cell membrane, reducing the microvesiculation of RBCs and consequently the hemolysis [22, 23]. Additionally, white blood cells (WBCs) are separated from RBCs as routine procedure (leucoreduction) in order to reduce the RBC damage caused by the enzyme release from destroyed WBCs under hypothermic conditions [24, 25].

Currently, all these developments enable a storage time of up to 6 weeks [26]. Despite this progress in the conservation technique of stored blood, changes called storage lesions occur at physical and metabolic level in the RBCs during the hypothermic storage [27, 28]. Physical changes involve modifications of rheological properties such as aggregability, deformability and osmotic fragility [29]. Typical metabolic alterations show reduced pH, decreased concentration of ATP and 2,3-DPG [30], leading to membrane alterations in RBCs.

The RBC membrane consists of a fluid phospholipid bilayer tethered to a two dimensional network, mainly composed of spectrin and actin protein [31]. It has been previously shown that this protein network can be biochemically affected by ATP and calcium. Both can remodel the cytoskeleton and therefore the shape and the mechanics of RBCs [32]. A particular

characteristic of young RBCs is the high membrane area to volume ratio, as only about 50% of the total surface area would be sufficient to contain the regular total volume of typically 90fL [33]. This extra membrane area is very crucial for the RBCs deformability which allows the volume redistribution for squeezing through small capillaries in the vascular system [33].

Under storage conditions, RBCs undergo depletion of ATP-levels and increased concentration of calcium. These processes are associated with membrane loss via micro vesiculation [34]. The erythrocytes change gradually from smooth biconcave disc shapes called discocytes (D) to spherical forms (spherocytes, S), passing through intermediate morphological stages such as bumpy discs associated with early microvesiculation (echinocytes, E) and more spherical and spiky forms (sphero-echynotes, SE) [35] (see figure 1). Another, but more sporadic form (stomatocytes), is characterized by an oval-shaped central area of pallor, and is associated with an increase of the inner leaflet area relative to the outer leaflet [36], which can be caused by lower pH.

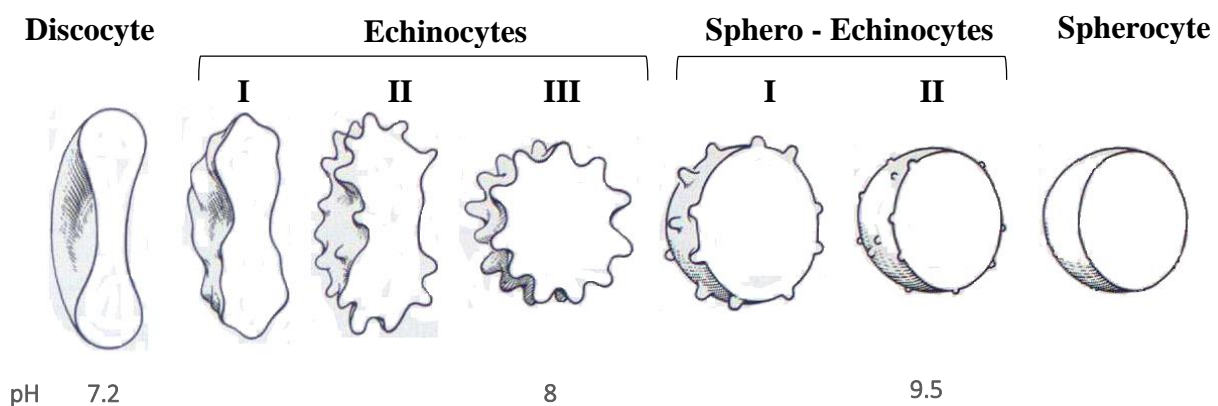


Fig 1. Morphological transformation of erythrocytes associated with pH changes according to Bessis [35]. The morphological stages from discocyte to sphero-echinocyte II are defined in [35]. For this study, the spherocyte category is introduced and describes the further cell stage corresponding to complete smooth spherical cells. For practical effects in this study, the type sphero-echinocyte II and spherocyte are grouped in the same category (spherocytes).

The aging process leads to alterations in the deformation ability and thereby in the cell-rheology. The deterioration of RBCs can be reversed in early stages by restoring the ATP levels with adenosine [37]. Beyond the sphero-echinocyte stage, RBCs do not have any mechanism to replace the lost membrane and consequently, the deterioration becomes irreversible. In general, after prolonged storage periods, the regeneration potential of RBCs diminishes and the mechanical properties e.g. osmotic fragility and deformability are not completely reversible [38]. The ability of RBCs to reverse the storage lesion effects is a useful measure of RBC function during transfusions: that the proportion of recovered RBCs after stabilization of ATP levels is correlated with the post-transfusion RBC survival [39, 40].

The key indicator of the deterioration of stored RBCs is the hemolysis, which represents the release of hemoglobin (Hb) into the suspending fluid due to cell rupture or shedding of micro-vesicles from RBCs [41]. Transfused free hemoglobin leads to medical complications [42, 43]. For that reason, regulatory agencies have established a maximal hemolysis limit for stored blood bags in order to prevent medical consequences after transfusion. The hemolysis is measured as the percentage of free Hb in relation with the total Hb contained in the red cell concentrate (RCC) scaled by the hematocrit factor. Currently in Europe, a damage-threshold of 0.8% hemolysis is set for RBC units [44, 45], above which they have to be discarded. The corresponding threshold in the USA is 1% [46]. However, the hemolysis measurement is not standardized between quality laboratories since there are different methods to measure the Hb concentration by using reagents and spectrophotometry (e.g. Drakin's or Harbour method; see e.g. [47]) and varying decision thresholds which make the hemolysis determination variable and not a straightforward method (e.g. [48]). Given the complexity, the absence of standardization and the labor intensive procedure for the hemolysis evaluation, RBC units are commonly only visually inspected to infer the degree of hemolysis according to the red color intensity in the RBC unit before the transfusion [49]. However, the visual assessment was demonstrated to be unreliable by comparing it with the spectrophotometric measurement [50]. It showed a high inaccuracy caused by inter-operator variability and dependence on the sample type. In some cases, high concentrations of bilirubin may hide the hemolysis by visual inspection, leading to underestimation of hemolysis with implications for the patients. In general, the visual inspection shows the tendency to overestimate the amount of existing hemolysis, leading to erroneous discard of RBC units and therefore waste of blood bags [50].

1.3 Morphometric Analysis of RBCs

Morphometric measurements based on the analysis of RBC shapes provide an alternate possible assay for the estimation of the quality of RBCs [35]. In this respect, microscopic analysis of RBCs has also been carried out in the context of hemolytic diseases in which morphological alterations of RBCs are associated with several medical conditions [51, 52]. However, the procedure is subjective, not automated, requires a considerable effort and is statistically limited by a low number of evaluated cells.

As initial approach to quantify the cell shape, some studies have developed methods for classification of RBCs from blood smears [53, 54]. One study proposed the morphometric parameterization of different RBC morphologies by automatically analyzing microscope images of RBCs by means of an image processing software [55]. In this study, the shape of regular erythrocytes was artificially modified by incubation in specific media and morphometric

parameters were subsequently assessed for characterization and classification of RBCs into seven defined types [56]. Beyond the automated image analysis, the image capture was subjected to conventional light microscopy which limits the acquisition of a large number of images for significant statistical analysis.

One recent study undertook the morphometric image analysis of stored RBCs moving in a single-cell layer into a custom made flow chamber [57]. The system was capable of generating large numbers of cell images for classification of RBCs according to pre-established morphological classes based on the cell diameter [35], but was not systematically tested as a measure of the RBC storage lesion and not compared to standard assays. The system had the additional disadvantage that it required the addition of a blocking agent to prevent interaction of RBCs with the chamber walls; the problem with this is that the blocking agent affects the RBC morphology [58] and would therefore change the results.

In recent years, digital holographic microscopy has been tested as a non-invasive and label-free diagnostic method [59, 60]. Based on the interference patterns (digital holograms) of the light during the induced rotation of individual RBCs, three-dimensional (3D) shapes of the cells were reconstructed [61]. The measured volumes of normal and modified RBC shapes agreed well with theoretical models and allowed the differentiation between normal, crenate and quasi-spherical RBCs. However, the principal limitation of this method is the low acquisition rate of information which hinders the fast and large amount of data acquisition for significant statistical analysis.

1.4 In situ Microscope

Two decades ago, first in situ microscopes (ISMs) were presented for real time monitoring of microorganisms in agitated bioreactors [62, 63]. The advantage of non-invasive in situ microscopy is that it enables the image capture of cells directly in a flowing suspension (Fig. 2). This technique enables both the large-scale virtual sampling of cells, and simultaneous online analysis by means of image processing. This way, a considerable advantage in terms of automation is achieved, removing the need for sample extraction and enabling large data acquisition for fast statistical analysis. The image processing is based on the analysis of morphological characteristics of the cells which can be correlated with biochemical and metabolic cell changes. These changes are conventionally measured through biochemical methods based on sample preparation and the use of dyes or reagents.

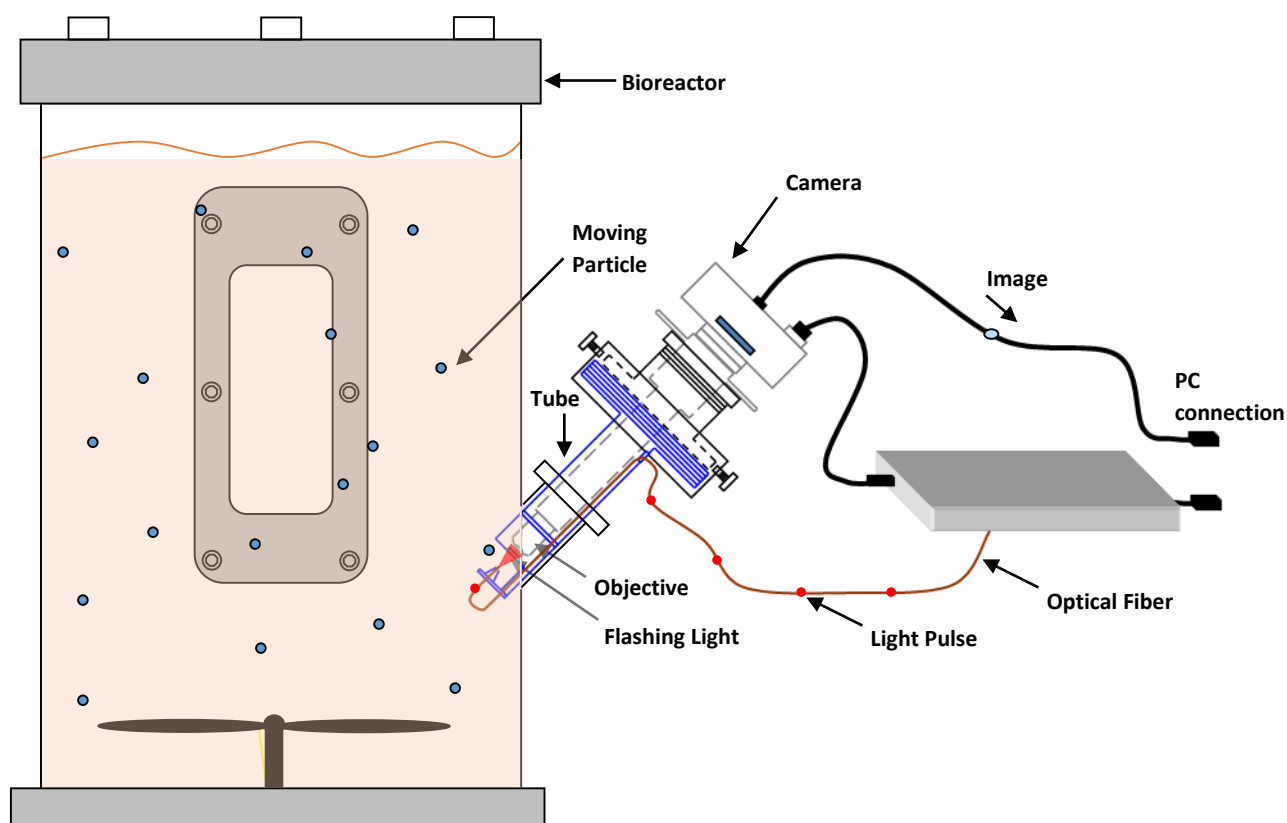


Fig 2. In situ microscope principle. Images of moving cells are capture directly into the flowing suspension. Short light flashes are emitted to capture sharp moving objects without blur effect. Depth of field principle allows to capture sharp objects in a focal range of approximately 7 μm .

The principle of the ISM does not need cell labeling which simplifies the technique to a large extent so that noninvasive probing of suspended cells within flowing suspension can be realized.

The ISM overcomes the negative effect of motion blur at the moment of capturing moving objects (cells) by controlling the exposure time of the camera sensor (shutter time) and the duration of the illumination. Due to the generation of short light pulses (about 1 μs), the setup captures images of moving cells without blur. The light pulses are synchronized with the frame capture according to a desired acquisition rate.

The optical principle of the microscopic imaging is based on depth-of-field, i.e. only cells within a certain focal range of typically 7 μm objects are sharply imaged. In this regard, the image processing discriminates blurred cells captured from outside the focal plane. The image stream is permanently sent to the computer for image analysis.

The suitability of the in situ microscope system has been previously tested for noninvasive assessment of viability of animal cells [64]. The system was able to estimate with high precision

the viability in hybridoma and other cultures by evaluating the texture inhomogeneity of the cells, which was found to be a typical marker of death in mammalian cells. More recently, the field of application of in situ microscopy was expanded to the detection and quantification of filamentous bacteria in sludge processes in order to eliminate the subjectivity of conventional methods using light microscopes. The results of in situ microscopy showed good correlation with reference methods [65].

1.5 Aim of the Study

In view of the absence of an automated standardized method for morphological assessment of RBCs, it is desirable to develop a robust and automated assay to quantify erythrocyte storage lesion based on morphological analysis. Such an assay should provide sufficient statistics in a short time for sensitive detection of morphological changes and the assay conditions should not influence or be selective for cell shape. Furthermore, it is essential for the assay to correlate with established measures of RBC storage quality.

The objective of this study is to build and test a simple, fast and automated flow cytomorphometry system to measure the storage lesion in RBC units. For this purpose, images of erythrocytes under in vitro flow conditions are to be captured and subsequently evaluated by image processing to extract relevant morphological features. The proposed system is based on an in situ microscope, which is coupled to a commercially available flow chamber specially designed for microscopic analysis. In contrast to blood-smears or other non-flow techniques, the rapid laminar flow of RBC aliquots in the flow channel provides a fast exchange rate of cells in the capture field of the camera, enabling the acquisition of large numbers of uncorrelated cell images. This is the basis for a statistically relevant assessment of damage related with the cell morphology.

The development of this system requires the design of a robust structure for the integration of new fluidic and mechanical parts into the existing in situ microscopy system. The system should be mechanically stable and the flow conditions must be controllable and characterizable as much as possible to ensure the experiment's reproducibility. The design should also ensure the exchangeability of fluidic the parts and the sterility of the sample (if necessary).

The development of an algorithm for image analysis of erythrocytes under flow condition is essential to parameterize morphological changes caused by the storage lesion. In this respect, a set of feature values is defined to characterize erythrocyte morphology. These parameters should also describe the pre-established morphological stages of erythrocytes according to [35] (see figure 1).

Based on this cell parameterization, a morphological classification of RBCs is carried out to evaluate the morphological distribution of RBCs in analyzed samples, which is supposed to change during the storage time. This implies the definition of a suitable metric that describe the proportion of the different erythrocyte types in RBC samples. This metric must be sufficiently sensitive to reflect morphological changes, allowing to infer the degree of damage in RBC units. The morphological assessment is compared to reference biochemical measurements (hemolysis, ATP and other standard measures) in order to validate the proposed method in this study.

The system is to be tested on samples of RBC units, obtained from collected blood of several donors and stored according to conventional protocols. Additional RBC units will be monitored in order to investigate the influence of gamma irradiation and heat treatment, two procedures known to advance the morphological aging of stored RBCs.

Taking into account the importance of hemolysis for inferring the degree of RBC-damage, this study attempts to demonstrate a convincing correlation between that biochemical marker and damage-assessment through flow cytomorphometry.

2 MATERIALS AND METHODS

The combination of in situ microscopy by depth of field [62] with a flow chamber is a new method developed for the purpose of this study and gives rise to the concept of *flow cytomorphometry*. For that reason, it also belongs to the results of the present study. However, methodological aspects of the system are the basis for the current development and therefore are mentioned in this chapter. Section 2.2 (RBC morphometry with in situ microscopy) describes technical aspects of the proposed method. For this scope, this section is divided into: fluidic principle and flow conditions (see 2.2.1 and 2.2.2), system setup (see 2.2.3 and 2.2.4) and image processing principle (see 2.2.5).

2.1 Materials

2.1.1 Devices, Accessories and Substances

Devices, Accessories and Substances	Reference	Manufacturer
Syringe Pump	Legato 270	KD Scientific Inc, Holliston, MA, USA
Automated Blood Separator	Compomat G4	Fresenius Kabi Deutschland GmbH, Germany
Hematology Analyzer	CELL-DYN Ruby	Abbott GmbH & Co. KG, Wiesbaden, Germany
Centrifuge	Rotina 38	Hettich GmbH & Co. KG, Tuttlingen, Germany
Spectrophotometer	DR 5000	Hach Lange GmbH, Düsseldorf, Germany
Gamma Irradiator	Biobeam GM 300	Gamma-Service Medical GmbH, Leipzig, Germany
Waterbath	WB 7	Memmert GmbH + Co. KG, Schwabach, Germany
In Situ Microscope - Light Pulse Generator		Hochschule Mannheim, Mannheim, Germany
In Situ Microscope - Camera	A102f	Basler, Ahrensburg, Germany
Dovetail Optical Rail, 12" Length	54-401	Edmund Optics, Barrington, USA
Dovetail Carrier 75mm Width	55-340	Edmund Optics, Barrington, USA
3D printer	Object260v Connex	Stratasys, USA
Flow Chamber	I ^{0.1}	Ibidi GmbH, Martinsried, Germany
Female Luer Lock Connector	10825	Ibidi GmbH, Martinsried, Germany

Male Luer Connector	10824	Ibidi GmbH, Martinsried, Germany
Silicon Tube (1.6mm inner diameter)	TYGON ND 100-65	Reichelt Chemietechnik GmbH + Co, Heidelberg, Deutschland
Plastic Syringe 2.5ml		Terumo Deutschland GmbH, Eschborn, Germany
Blood collection bag system	CompuFlow	Fresenius Kabi AG, Homburg, Germany
In Situ Microscope- Water Immersion Objective	40x - NA 0.75	Lomo, St.Petersburg, Russia
Pigtailed Luminescence Diode	650nm/2A	DieMOUNT, Wernigerode, Germany
ATP Hexokinase FS	1 6201 R	DiaSys Diagnostic Systems GmbH, Holzheim, Germany
Buffer Solution	fHb	Bioanalytic GmbH, Freiburg, Germany
Sodium Chloride	NaCl 0.9%	B. Braun Melsungen AG. Melsungen, Germany

Table. 1. List of used devices, accessories and substances in this study

2.2 RBC Morphometry with in situ Microcopy

2.2.1 Fluidic Principle

The experimental technique presented in this study is based on imaging of RBCs moving in a flowing suspension. Similarly to conventional flow cytometry, one obtains a fast exchange of cell samples so that a large data set becomes possible.

As shown in figure 3, RBC suspensions are pumped through a flow chamber type I^{0.1} (ibidi GmbH, Martinsried, Germany) especially designed for microscopic analysis of cell cultures and flow applications. The bottom of the flow chamber is made of a thin hydrophobic plastic sheet (180µm) with a high optical quality for microscopy, similar to coverslips of glass and with a low birefringence [66]. The two channel inlets allow an easy connection with pumping systems through Luer connectors. The dimensions of the channel are 50 x 5 x 0.1mm ($l \times w \times h$) and assure a large area of uniform hydrodynamics. The two Luer channel inlets located at each side of the chamber are connected to two 2.5ml syringes by silicone tubes (1.6mm Ø). One of the syringes is used as reservoir, within which a 1.5ml diluted RBC sample is introduced. The second syringe is mounted into the holder of a syringe pump (Legato 270, KD Scientific Inc, Holliston, MA, USA). The mechanical action of the syringe compartment of the pump applies a push-pull force over the syringe plunger. In this way the solution repeatedly flows back and forth from one syringe to the other through the chamber (Fig. 3). Due to the quick passage of

the cells through the capture area of the microscope at a configured flow rate, a fast image acquisition rate can be set up without repeated imaging of individual RBCs on consecutive frames. Additionally, the fast flow speed avoids sedimentation of the cells by keeping the suspension in motion.

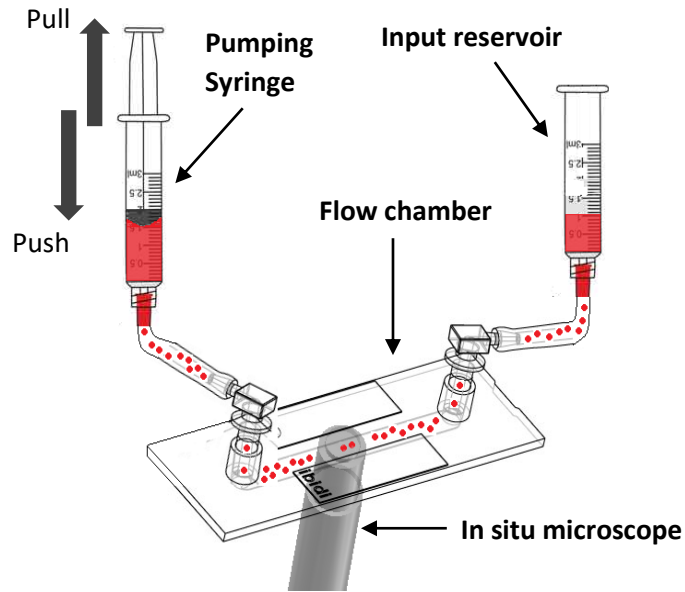


Fig. 3. Experimental setup. Principle of flow cytometry using in situ microscopy. Erythrocytes flow cyclically between syringes through a microfluidic channel and are imaged by an inverted microscope. The microscope captures images of moving erythrocytes illuminated by microsecond light flashes emerging from an optical fiber above the flow chamber (optical fiber shown in figures 8 and 9). Flow chamber illustration: ibidi GmbH.

2.2.2 Flow Dynamic: laminar Flow and Shear Stress

In this study, suspended RBCs were subjected to a laminar flow through the flow chamber. A flow is laminar if the Reynolds Number (Re) of the fluidic structure is well below 2000 [67]. The Reynolds number is computed as:

$$Re = \frac{\rho v D_h}{\eta} \quad (\text{eq. 1})$$

Where:

$\rho \approx 1 \text{ g/cm}^3$	Density of the medium (NaCl concentration 0.9%; 22°C)
$v = 1.67 \text{ cm/s}$	Mean flow velocity
$\eta = 0.01 \text{ dyn} \cdot \text{s/cm}^2$	Dynamic viscosity (sodium chloride NaCl)
$D_h = 2 \cdot w = 1 \text{ cm}$ for $w \gg h$	Hydraulic diameter

Here, the numerical values correspond to the fluidic conditions in this study ("standard values"). From these values, a corresponding $Re=137$ was obtained. Therefore, the suspension moves in streamlines parallel to the bounding plates. Figure 4 shows the velocity as function of height across the flow channel (Fig. 4a). The velocity gradient causes a shear stress on the RBCs which increases inversely proportional to the distance from the walls. Due to the flat channel (height \ll width), only the gradient of velocity along the channel height is relevant for the flow conditions, while the shear stress generated by the lateral walls is negligible for the image capture area.

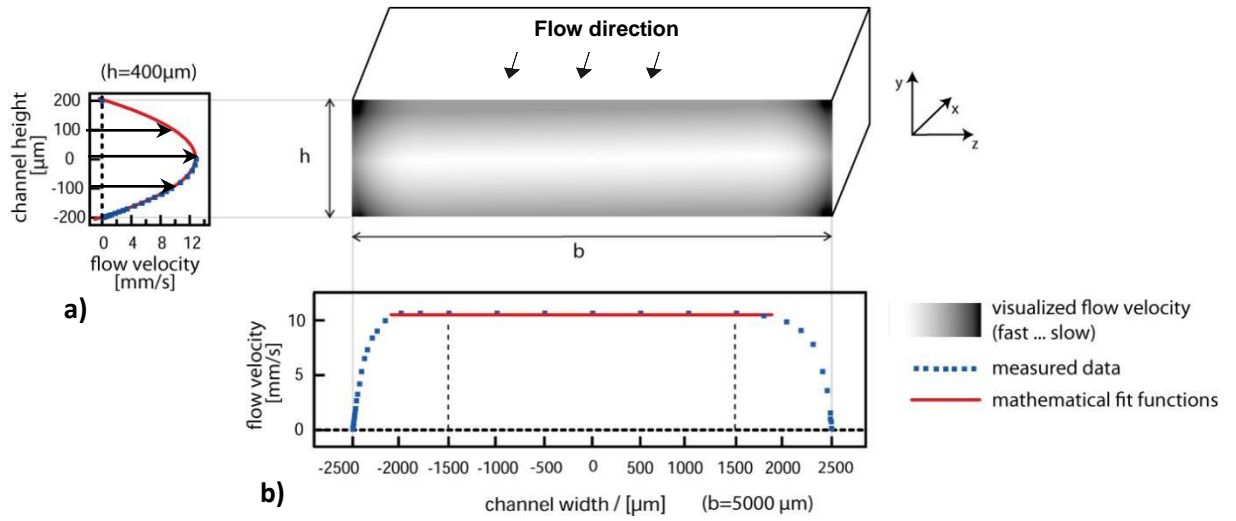


Fig. 4. Flow velocity profile in a flow chamber (400μm height) a) along the channel height and b) along the channel width under laminar flow conditions. Flow velocity is homogeneous along the channel width. (Illustration: ibidi GmbH, altered)

According to [68], the flow velocity v as function of the height position y is defined for a given flow rate F , channel height h and width b as follow:

$$v(y) = \frac{6F}{b \cdot h^3} (hy - y^2) \quad (\text{eq. 2})$$

For Newtonian fluids, the shear stress τ is proportional to the velocity gradient in the channel and to the dynamic viscosity of the medium. In a two plate parallel channel like the one used in this study, the shear stress is given by:

$$\tau(y) = \eta \frac{dv}{dy} = \eta \frac{6F}{b \cdot h^3} (h - 2y) \quad (\text{eq. 3})$$

and the corresponding shear rate is given by:

$$\gamma = \frac{\tau}{\eta} \quad (\text{eq. 4})$$

Given the conditions of the measurements, it is expected that a range of stress values will be generated at different heights in the flow chamber. Under certain shear stress values in laminar flow, RBCs tend to orient themselves and rotate as if they roll on a surface parallel to the chamber wall in the direction of the suspension flow [69].

Disc-shaped RBCs move in two different modes depending on the existing fluidic forces [69]. Based on a medium viscosity of $0.07 \text{ dyn} \cdot \text{s}/\text{cm}^2$, discocytes flip and deform without a regular pattern at low shear stress ($\approx 45 \text{ dyn}/\text{cm}^2$) [69]. However, increased shear rates force the cells to roll with their rotation axis perpendicular to the flow direction and parallel to the chamber bottom (see figure 12 for visual reference). Considering the zero shear stress at half channel height, fresh RBCs symmetrically exhibit the rolling mode far side of this height. This orientation property is used for the imaging of RBCs. The setting of the flow conditions required for this effect is explained as part of the results in section 3.4.

2.2.3 In situ Microscope Setup

The in situ microscope provides a continuous image stream of moving cells in suspension as for example in agitated bioreactors [62, 63]. Limited by the optical depth of field (DOF) of the microscope, the focal range is approximately $7.4 \mu\text{m}$. Therefore, only cells within this focal range are sufficiently sharply imaged to be detected by the automatic image evaluation. This allows the non-invasive observation of small virtual probe volumes within the cell suspension without mechanical borders [63, 64]. The free motion of the cells requires short light flashes for imaging moving cells without blur. A light pulse generator (LPG) generates short light flashes emitted by a luminescent diode (LED). These pulses are synchronized with the exposure signal of the camera sensor. An optical fiber coupled to the LED conducts the light coming from the LPG to the image capture field.

For the imaging, a water immersion objective (40x, NA 0.75; Lomo, St.Petersburg, Russia) is used. This determines the depth of the probe volume (i.e. the effective focal range) along the optical axis, which is approximately $7 \mu\text{m}$. The probe volume cross section perpendicular to the optical axis (i.e. the object field) is given by the format of the CCD-chip and the objective's imaging. The acquired images (resolution 1392×1040 pixels; pixel size $0.16 \times 0.16 \mu\text{m}^2$) are analyzed by means of an algorithm which selectively detects the sharp cells within the depth

of field. The position of the focal range can be adjusted with micrometer resolution within the total height (100 μ m) of the flow channel. This permits the observation of RBCs at different specific distances from the bottom of the chamber.

The objective of the in situ microscope is connected to the camera (A102f, Basler, Ahrensburg, Germany; CCD-Size 2/3") through an extension tube and positioned below the flow chamber, realizing an inverted high resolution microscope. From the top, an optical fiber ending (diameter =1mm) coupled to a custom made light pulse generator (LPG) provides the pulsed illumination to the flow chamber by means of short flashes ($\approx 3 \mu$ s/1A) which are generated by a pigtailed luminescence diode (DieMOUNT, Wernigerode, Germany; 650nm/2A). The light pulses are synchronized with the frame acquisition of the camera. The electronics permits the acquisition of images at a maximal frame rate of 15 Hz. Given this rate and the capture area of the camera (225 x 167.7 μ m²), particles must move faster than 3.4mm/s to avoid being captured more than once between consecutive frames.

2.2.4 Mechanical Adaptation of in situ Microscopy to Flow Cytomorphometry

The method presented in this study is based on the adaptation of *in situ microscopy* to the capture of images of moving cells in a flow chamber. For that reason, the fluidic and mechanical parts had to be coupled and positioned with respect to the optics in an efficient way in order to ensure functioning and an optimized operability of the system. For this purpose, an aluminum housing was designed by using the 3D-CAD-Software Inventor® (Autodesk Inc.). This software offers a large set of tools specially designed for mechanical 3D-constructions and component simulation. The housing was intended as the main structure for the assembly of all parts (optical, mechanical and fluidic) providing stability, robustness and micrometric precision in order to ensure the reproducibility of the experiments and therefore the data consistency. The manufacturing of the housing was made by a specialized mechanical engineering company (Hallstein Maschinenbau GmbH, Hemsbach, Germany). The existing components of the in situ microscope and the adapted parts are listed as follows:

FLOW CYTOMORPHOMETRY SYSTEM - HOUSING		
Existing in situ microscope parts	Adaptation to in situ microscope	
	Fluidic parts	Mechanical adapters
<ul style="list-style-type: none"> • Camera • Light pulse generator • Extension tube • Objective • Optical fiber • ISM-Viewer software interface 	<ul style="list-style-type: none"> • Syringe pump • Pumping syringe • Flow chamber • Input reservoir • Luer connectors • Immersion water syringe • 3D-printed immersion water cap 	<ul style="list-style-type: none"> • X-Y-Z stage for flow chamber micro positioning • Linear translation stage rail • 3D-printed flow chamber holder

Table 2. List of existing components of the in situ microscope and new fluidic and mechanical parts for the adaptation of the microscope to flow morphometry.

2.2.5 Image Filtering for Recognition of sharp Objects

Specific detection of sharp objects in the images takes place by suppressing low spatial frequencies in the image which correspond to blurred objects. Images have a frequency representation in which their frequency components depend on changes of contiguous pixel intensities. The more abrupt the transition of pixel intensities, the more high frequency components in the image. Intensity changes occur normally in the boundary region of objects due to the contrast between the object contour and the image background. Blurred objects show diffused contours with gradual transition from the object to the background, corresponding to low frequency components. Since blurred cells contain insufficient amount of information for contour and texture analysis (Fig. 5), a high frequency filtering of the image eliminates them and keeps only cells with sharp intensity changes.

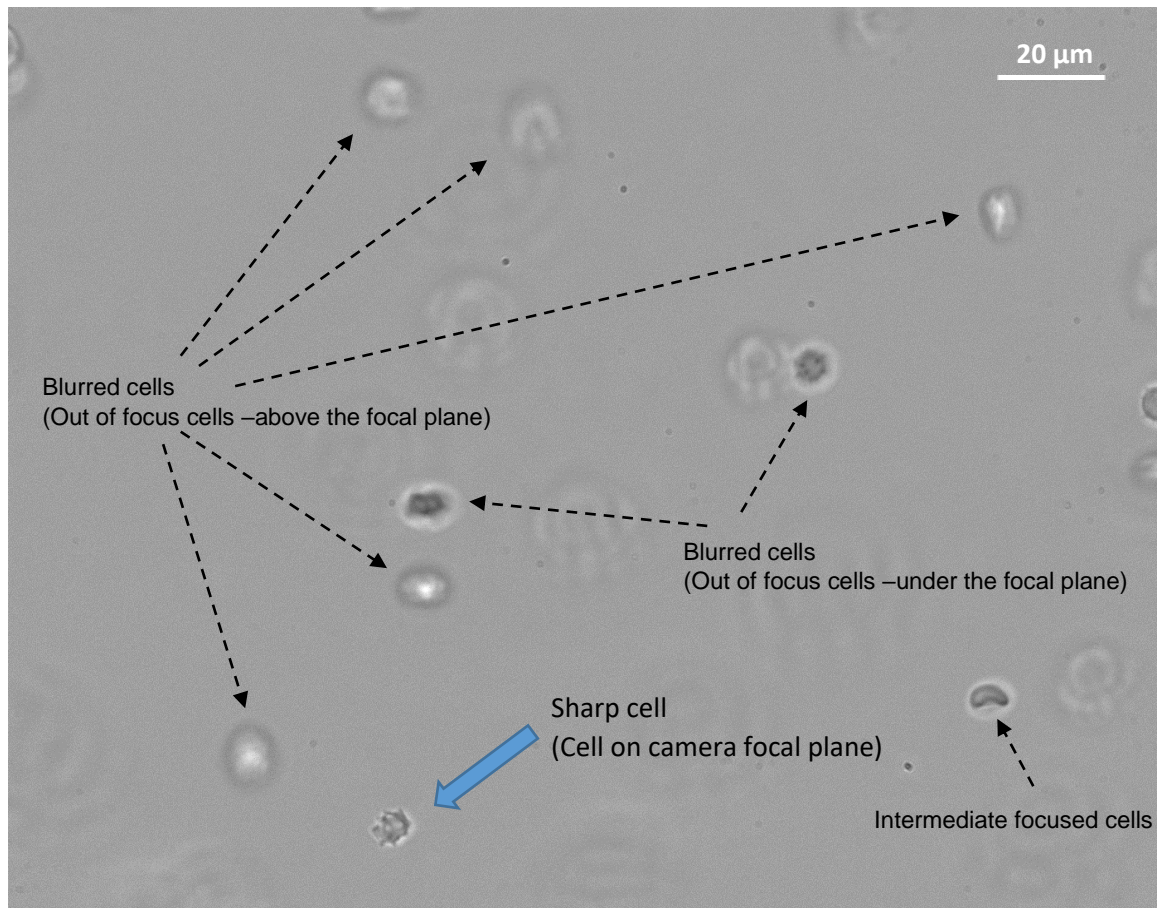


Fig 5. Typical cell image with focused and unfocused RBCs. These latter appear as bright and dark blurred objects located above and under the focus plane respectively.

2.3 Software Platform

2.3.1 ISM Viewer

The operation of the ISM system for the image acquisition is carried out by the software platform *ISM Viewer* [70] (Hochschule Mannheim, Germany). It provides a graphic user interface for parameter adjustment of the camera and light pulse generator and allows the synchronization between them at the desired capture frame rate. The software is written in C# programming language and runs in the most recent Windows versions (32 or 64 bits, Windows XP/7 and 10).

2.3.2 MATLAB

The image analysis algorithm was developed in the matrix-based MATLAB language (version R2015a, MathWorks Inc, Natick, MA, USA). MATLAB offers a software environment with prebuilt libraries for technical computing and data analysis in different engineering and scientific areas. It allows the development of custom-made algorithms by using the MATLAB components and functions. For this study, the set of functions for image processing called *image processing toolbox* were employed to pretreat the cell images and perform some part of the analysis. Calculation, data visualization and statistical analysis were carried out by using the standard module of MATLAB *Math, Statistic and Optimization*.

2.4 Blood Collection and Storage

Venipuncture from voluntary healthy adult donors aged between 19 and 59 was performed at the Institute for Transfusion Medicine and Immunology Mannheim. All donors submit informed consent that their blood may be used for quality control or research purposes aiming to improve the safety of hemotherapy. The Ethical Committee of the University Medical Centre Mannheim (UMM) assured that no specific ethical vote was required to perform this study. The extracted blood ($500\text{ml} \pm 10\%$) was collected in a quadruple bag system (CompuFlow, Fresenius Kabi AG, Homburg, Germany) and immediately mixed with 70ml of anticoagulant citrate phosphate dextrose (CPD). Whole blood components were separated by centrifugation for 15 minutes at 3500 rpm followed by leucofiltration of RBCs and addition of 110ml of saline adenine glucose mannitol (SAGM, 376mOsm/l) using an automated blood separator (Compomat G4, Fresenius Kabi Deutschland GmbH, Germany) prior to final storage at 4°C.

Three sets composed of 5, 7 and 5 fresh RBC units from donors who had provided informed consent were selected for this investigation. All sets comprised RBC units from donor groups with mixed age, gender and blood groups. The sampling was carried out for 13 weeks in intervals of one to three weeks; monitoring periods started 23rd September 2014, 24th February 2015 and 29th January 2016, respectively.

Irradiation of one RBC unit of the third set was carried out by using a gamma irradiation device (Biobeam GM 300, Gamma-Service Medical GmbH, Leipzig, Germany) with a middle dose of 30 Gy for 11 minutes. No point of the unit was irradiated below the minimal established dose of 25 Gy. [45]

One RBC unit was heated to 44°C for 20 minutes within a waterbath (WB 7, Memmert GmbH + Co. KG, Schwabach, Germany).

2.4.1 Sample Preparation, morphological and biochemical Assessment.

Before sampling, the units were agitated for 20 minutes by rotating at 0.1 rps. Samples of 12ml were extracted from each unit for biochemical and morphological analysis. From this volume, 1.5µl were sub-sampled for flow morphometry, and diluted 1000 times in sodium chloride (0.9% NaCl) to avoid overlapping of cells on the images and were immediately subjected to analysis. The dilutions were performed as a series of three steps with a dilution factor of 10 per step, for a final dilution factor of 1000. For hemolysis measurements, the hemoglobin of a 4ml sample was measured with a hematology analyzer (CELL-DYN Ruby, Abbott GmbH & Co. KG, Wiesbaden, Germany). For the measurement of free hemoglobin, 2ml samples were centrifuged at 4000rpm for 10 minutes (Rotina 38, Hettich GmbH & Co.KG, Tuttlingen, Germany). From this, 50µl supernatant was diluted in 500ul buffer solution (fHb, Bioanalytic GmbH, Freiburg, Germany) and analyzed spectrophotometrically (DR 5000, Hach Lange GmbH, Düsseldorf, Germany). In the same device, ATP levels were analyzed using ATP Hexokinase FS (DiaSys Diagnostic Systems GmbH, Holzheim, Germany) according to the instructions of the manufacturer.

2.5 Morphological Categorization of RBCs

For this work, three morphological stages (classes) were defined, based on the progressive changes of the cell membrane during storage (Fig. 16). RBCs in the first stage are called discocytes (D) since they can be described as smooth biconcave discs. In the second stage, RBCs are called echinocytes (E) and are characterized by the appearance of bumps, which gradually become more numerous and finer, while the cells become more spherical. Echinocytes comprise a set of several sub-types, which are described in [35]. RBCs in the third morphological stage are called spherocytes (S) since they have a spherical shape. In addition, there is a small number of false classifications due to the fact that stomatocytes were not specifically take into account. Relative to the high frequency of typical D, E and S types, stomatocytes were very rarely seen in the images. Their influence on the overall statistics is therefore expected to be small and their classification is not included in this first investigation. This scheme with three morphological classes constitutes a lower classification resolution as compared to previous work [35, 57]. However, it reduces the effort in signal processing and it is an adequate starting point.

3 RESULTS

3.1 Setup for Flow Morphometry of RBCs

As above described, the flow cytomorphometry system is an adaptation of the in situ microscope to new flow conditions of the cells. Figure 6 shows the schematic diagram of the system concept in which a new fluidic module is coupled to the conventional in situ microscope.

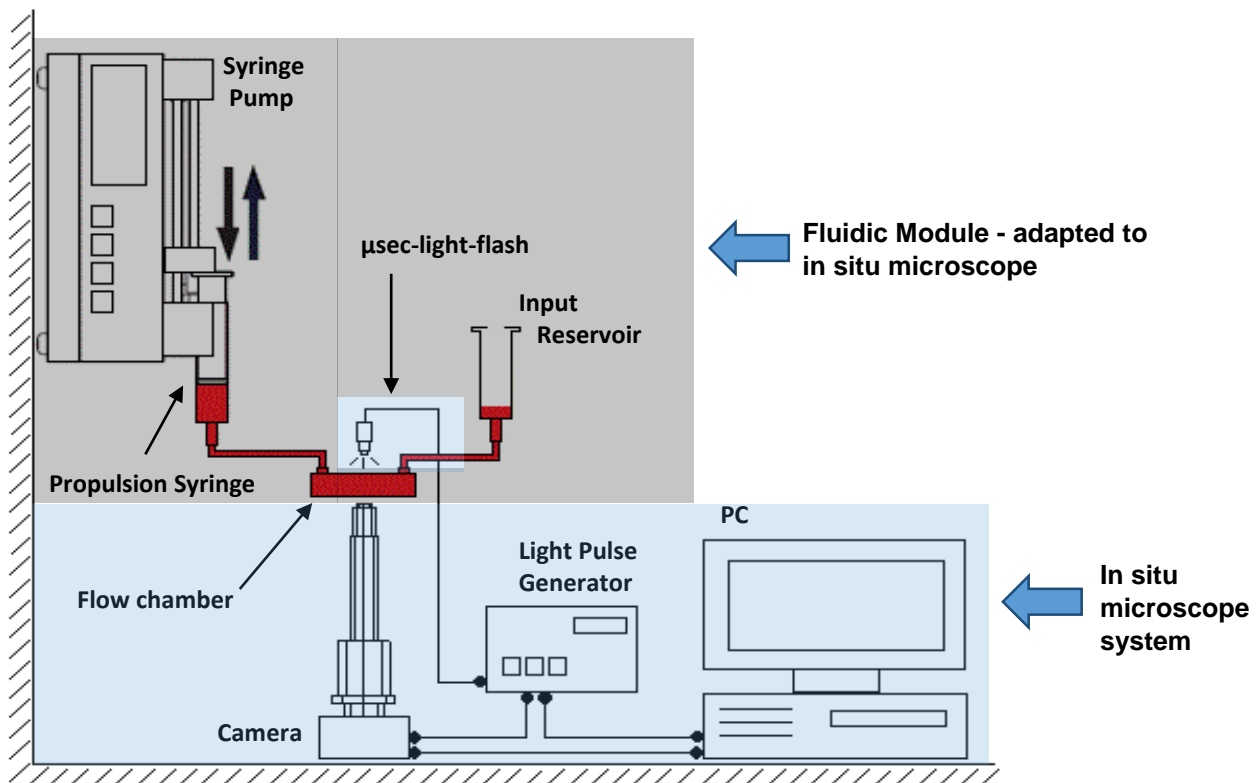


Fig. 6. Experimental setup. Erythrocytes flow through a microfluidic channel and are imaged by an inverted microscope. The microscope captures still images from the depth of field within the suspension flow illuminated by microsecond light flashes emerging from a optical fiber above the flow chamber.

3.2 Housing Design and Component Assembly

The housing consists of five plates made of aluminum (1cm thickness). They hold all components of the system and allow an easy connection between parts ensuring stability against vibration (Fig. 7). The housing design was conceived to keep the fluidic parts close together to minimize the flow path between syringes and therefore reduce the required sample volume. The camera (6) is positioned below the flow chamber (7) pointing upwards for looking at the flow chamber from the bottom side. The syringe pump (9) is positioned at the same elevation as the flow chamber to ensure a short distance from the pumping syringe (10) to the chamber.

The vertical orientation of the pump enables vertical orientation of the syringes and thus minimizes the sedimentation area inside the pumping syringe (Fig. 8). The plunger flange is fixed in the retaining bracket (36) of the pusher block (15, allowing the transfer of the mechanical action of the pusher block to the syringe plunger. The pusher block travels up and down along the precision lead screw (16) that is driven by the stepping motor of the syringe pump. The syringe plunger is fully inside the barrel as initial position, so that the subsequent pull action of the plunger withdraws the fluid contained in the input reservoir (20) which then passes through the flow channel to the barrel of the pumping syringe. The opposite push action re-infuses the fluid in the input reservoir. A 2.5ml syringe barrel is used as input reservoir.

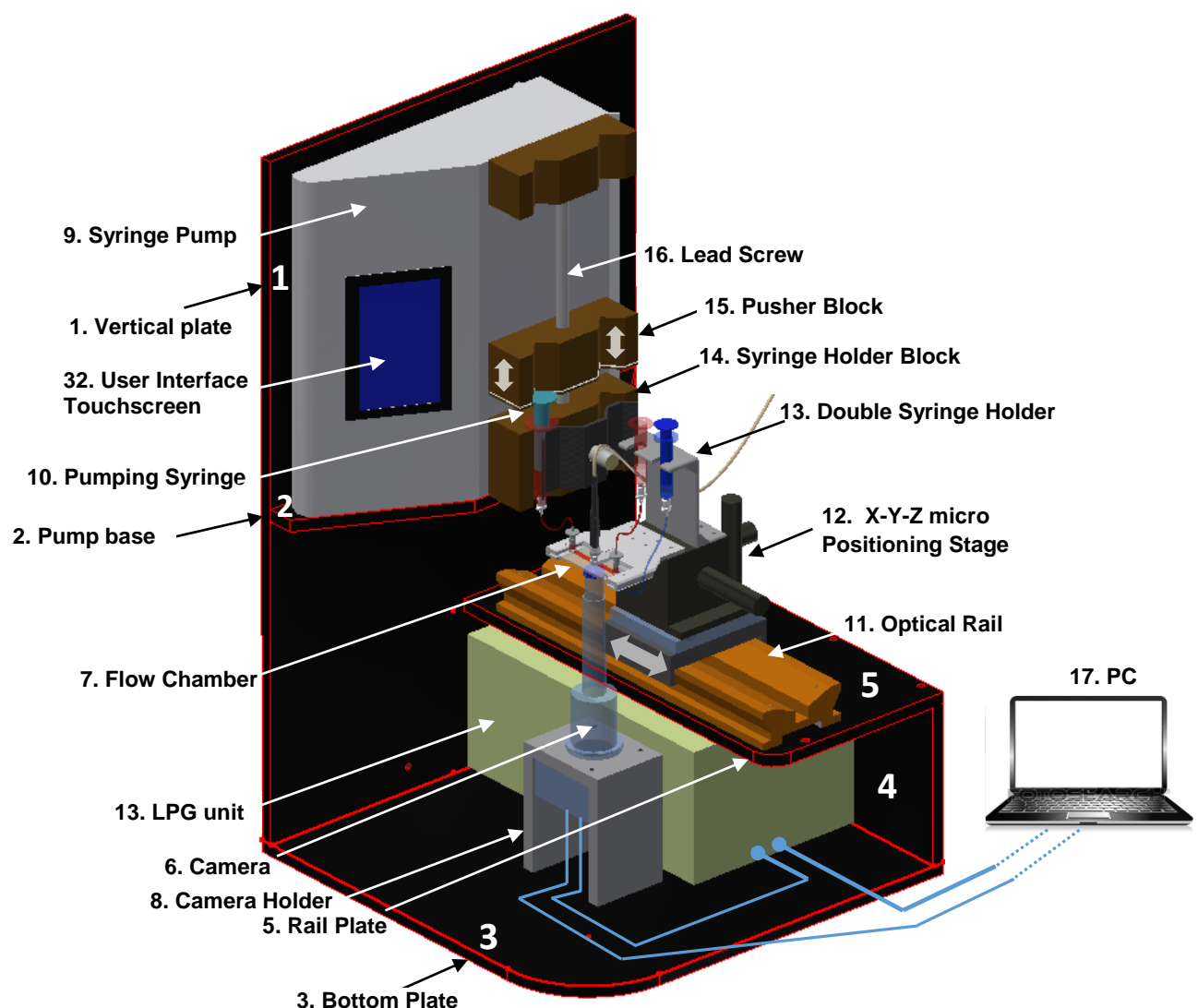


Fig 7. Housing-CAD of the microscope system with all mechanical, electronic and fluidic components.

The flow chamber is positioned in a custom made holder (18) designed in AutoCAD and manufactured by means of an in-house 3D printer. The optical fiber (26) is connected to the chamber holder from above to provide the flash illumination for the imaging. The chamber holder is fixed to the micro positioning stage so that the flow chamber can be three-dimensionally displaced.

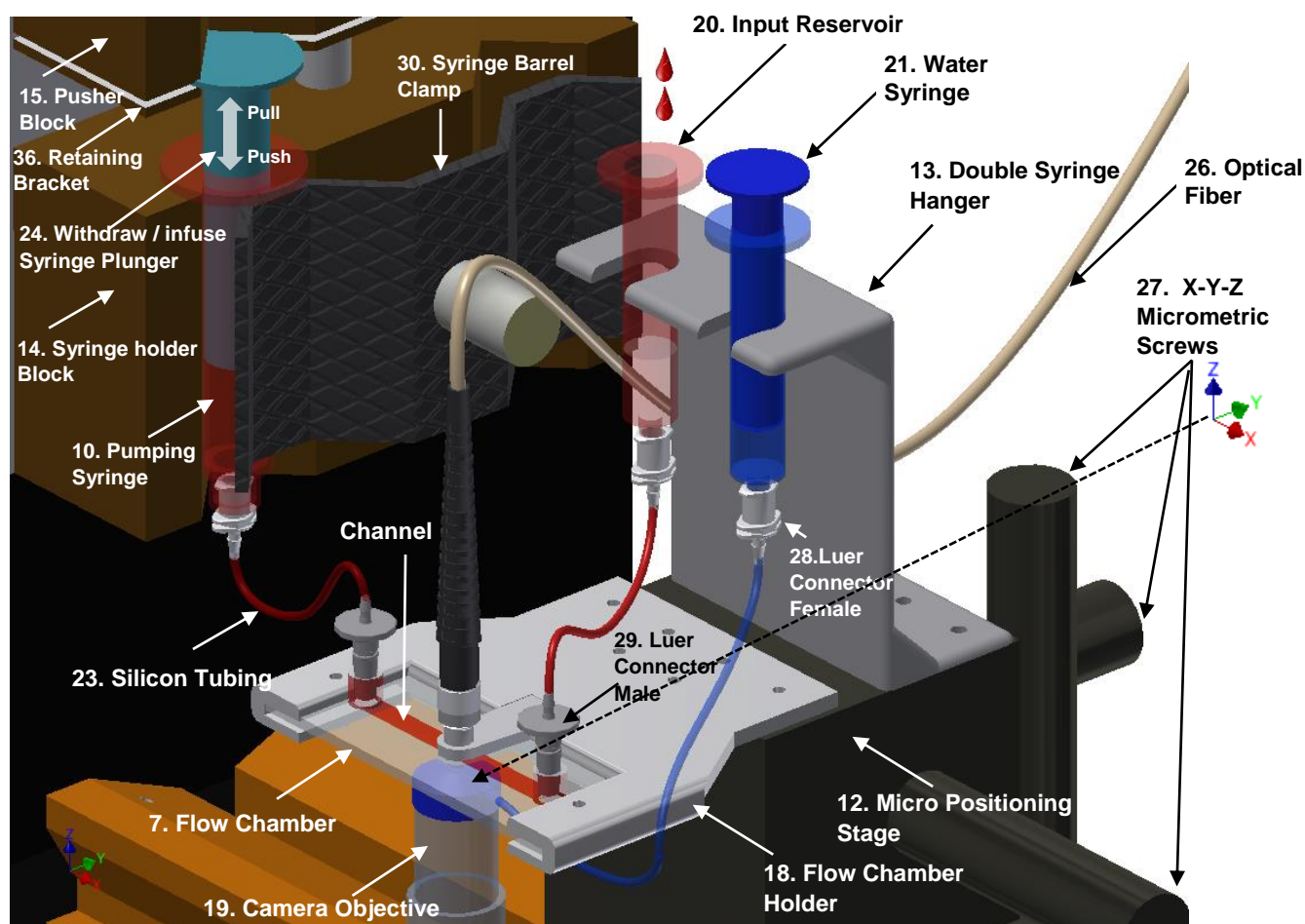


Fig 8. Positioning of fluidic parts. Syringes are vertically oriented to minimize sedimentation.

The X-Y micrometric screws (27) allow the adjustment for the vertical alignment between the optical fiber and the objective lens. The Z micrometric screw (27) sets the focal plane height by moving the chamber along this axis. The double syringe holder (13) is also fixed to the micro positioning stage and sustains the input reservoir and the water syringe. Input reservoir, flow chamber and pumping syringe are interconnected through short segments (10cm) of silicone tubings (23),(34). Female and male Luer Lock connectors (28),(29) are used to connect both sides of the silicone tubings with the syringes' barrels and the flow chamber inlets respectively (Fig 9). In the same way, the water syringe is connected to the inlet of the objective cover cap (31) through a larger silicone tubing (33) that conducts the water for the immersion objective (19).

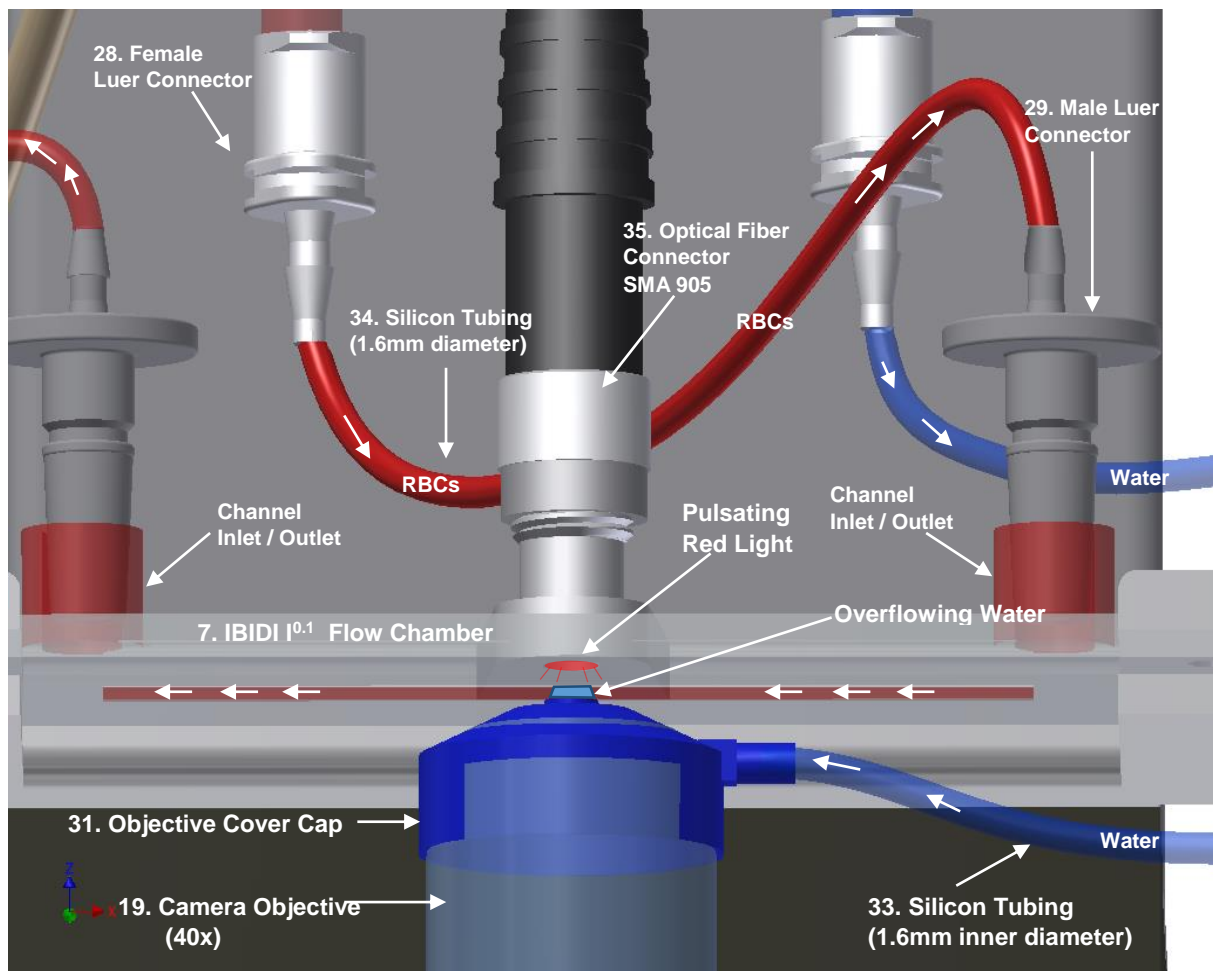


Fig 9. Water immersion mechanism for the camera objective through the custom made cover cap and water injection principle. Illustration shows the optical fiber, flow chamber and tubing connections. Moving RBCs are indicated only in one direction corresponding to the withdraw cycle of the pump (pumping syringe pulling).

In order to achieve the high resolution needed for the measurements, the inverted microscope had to be made compatible with the application of imaging through a water immersion. To enable a stable water immersion of the objective, an objective cover cap was constructed. It generates a compartment above the camera objective where the required immersion water between the objective lens and the bottom of the ibidi flow chamber acting as cover slip can be contained (Fig. 9). The empty space above the objective is filled with water by using a syringe (21). Due to the small gap between the cover slip ($\approx 1\text{mm}$) and the cover cap upper hole, the overflowing water wets the coverslip surface. This arrangement and the adhesion of the water establishes a stable immersion for up to two hours. As with the flow chamber holder, the objective cover cap was CAD-designed and generated by a 3D printing process. The circular upper hole of the objective cover cap is aligned with the objective lens so that the flashing light passes directly through the flow chamber and the water without cover cap material interference (Fig. 10). The optical fiber ending consists of an SMA connector allowing

an easy and stable connection with the flow chamber holder through the screw system. An optical rail (11) permits the mounting and dismounting of the microscope assembly. The housing and positioning of components was conceived to minimize the footprint of the device (36cm x 36cm).

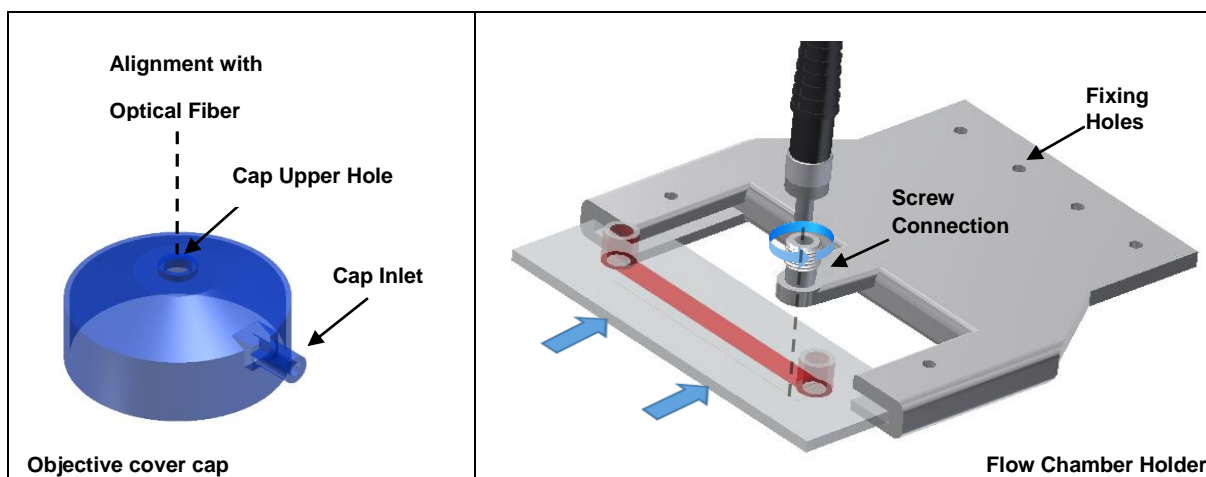


Fig 10. Objective cover cap (left) and flow chamber holder (right). Both parts were CAD-designed and manufactured by an in-house 3D printer.

3.3 Fluidic Operation

Prior to image acquisition, the fluidic parts are interconnected and mounted in their respective holders. 1.5ml diluted RBC samples are introduced into the input reservoir. From this sample, approximately 500µl are required to fill the two silicone tubings and the flow chamber. In order to avoid emptying of the channel during image acquisition, the chamber and the tubes are filled prior to the pumping activation. This assures a symmetrical volume exchange between input reservoir and pumping syringe and keeps the channel permanently filled during operation. The filling of the fluidic parts is performed by using the *Fast Reverse* function of the pump. This movement corresponds to the *Withdraw* mode of the syringe pump. The opposite direction of the pusher block is called *Infuse* (Fig. 11)

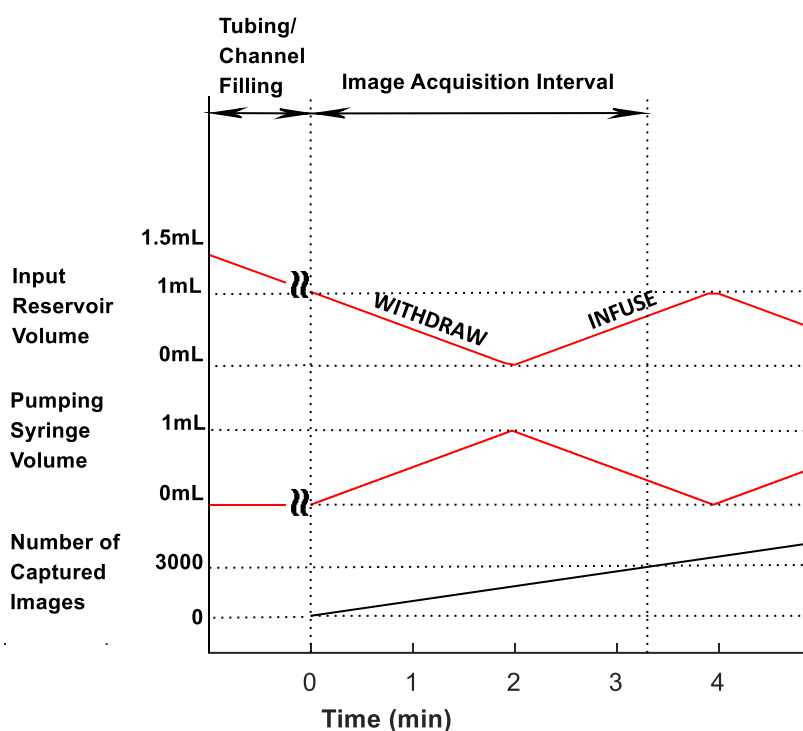


Fig 11. Volume of the input reservoir and pumping syringe during the Withdraw/Infuse cycle of the syringe pump.

After filling the tubing and flow chamber, the information about the target volume (1ml), syringe volume (2.5ml) and flow speed (0.5ml/min, see section 3.4) must be entered in the pump. Based on this information, the syringe pump calculates the total advance of the pusher block for the withdraw and infuse actions. The pump is configured to perform a continuous Withdraw/Infuse cycle so that the sample flows repeatedly between input reservoir and pumping syringe. Meanwhile, RBCs move constantly through the flow chamber in the direction determined by the momentary pump mode.

During the RBC motion, images are captured at a frame rate of 15 Hz (900 images per minute). This frequency is synchronized with the flashing of the red light coming from the LPG unit. Simultaneously, the images are saved to be subsequently analyzed by the image processing algorithm.

The number of detected RBCs in each image is proportionally related to the concentration of cells in the suspension medium. A low concentration of RBCs avoids cell overlapping in the images, a problem that leads to loss of crucial information for the cell border recognition. In order to minimize the overlapping, a low concentration (5×10^6 cells/ml) was adjusted to obtain a moderate rate of cells per image (< 10). On average, one in twenty RBCs is captured on the camera focal plane. The rest of RBCs appear out of the focal plane as blurred shapes (Fig. 5)

and hence they are not analyzed by the algorithm. With this concentration, only one RBC in every two images was recognized as a sharp cell for morphological analysis. This cell concentration can be doubled without risk of significant variation in the results. A minimum of 2500 images per sample are taken, so that more than 1000 RBCs were analyzed for each data point

This quantity of images can be obtained only during the first withdraw action of the pump without requiring the opposite cycle (infuse) by working with a bigger input volume (>2ml). Nevertheless, this leads to a larger pump cycle and consequently the cells tend to sediment in the syringes, making the cell concentration progressively more irregular during the flow. This is reflected in a variable rate of cells per image and can lead to agglomeration of cells in short time intervals under very extreme sedimentation conditions. Working with smaller volumes implies more pump cycles with fluctuation of the flow speed during the flow reversal.

3.4 Discocyte Orientation: optimal Flow Rate and focal Plane Height

According to [69], cells in a rolling motion should be observed at specific shear stress. Indeed, at a shear stress of approximately 8 dyn/cm^2 , occurring at $12 \mu\text{m}$ above the channel bottom, a large proportion of discocytes were observed in the rolling mode. This effect occurs in proximity to either the top or bottom channel walls of the flow chamber where the shear stress is maximal due to the greater velocity gradient. Before the measurement, the setting of the focal plane takes place by initially letting the cells settle down and then focusing them on the channel bottom. This allows to find the zero point of the channel height. Subsequently, the desired focalization height is adjusted by using the Z control of the micro positioning stage (see section 3.2). From the camera perspective, a rolling discocyte appears as an oval contour seen from the channel bottom. For morphometric recognition of discocytes, this effect was taken into account since the oval profile facilitates the recognition process. Only discocytes and very early echinocytic stages of erythrocytes (E I) are observed in the rolling mode. Mature echinocytes and spherocytes cannot exhibit any orientational preference since their morphology is isotropic. In this study, the appearance of the rolling mode is demonstrated by measuring the orientation of the RBCs. The orientation is measured as the angle (β) between the major axis of the RBC contour and the flow direction. β -values around zero indicate that the discocytes are moving vertically with their rotation axis perpendicular to the flow direction. This means they roll aligned with the flow direction (Fig. 12b). Orientation unequal to zero ($\beta > 5^\circ$) corresponds to non-rolling cells with random orientation (Fig. 12c and 12d).

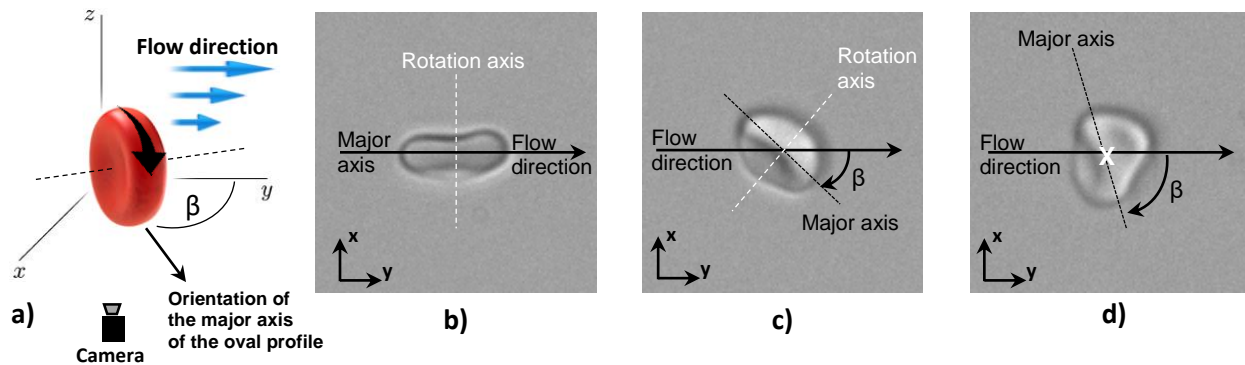


Fig. 12. Cell micrographs of one day stored discocytes captured from channel bottom at different flow conditions. Flow direction from left to right. The major axis corresponds to the line intersecting the two more distant border points of the cell contour. **b)** Vertically oriented discocyte. Major axis is aligned with the flow direction ($\beta=0^\circ$). Flow rate = 0.5ml/min. Focal plane height (FPH) = 12 μ m. **c)** Flipping discocyte captured at a higher focal plane under the same flow rate. $\beta= -45^\circ$. **d)** Deformed discocyte captured at 2ml/min. ($\beta= -80^\circ$). Rotation axis is perpendicular to the plane of the graph (x).

Figure 13 shows histograms of the angle β at specific height levels in the channel at a flow rate of 0.5ml/min for a one day stored RBC unit. Highest fractions of vertical oriented discocytes are obtained in proximity to either the top or bottom of the flow chamber wall indicating a symmetry in the distribution of the cell orientation with respect to the middle level of the channel height (50 μ m). This corresponds to the symmetry of the velocity profile and thus to the symmetry of the shear stress profile along the channel height. A different β -distribution but with the same symmetry occurs between the second and third quarter of the channel height, where β adopts a wider distribution of angle values which correspond to a lesser proportion of aligned (rolling) discocytes.

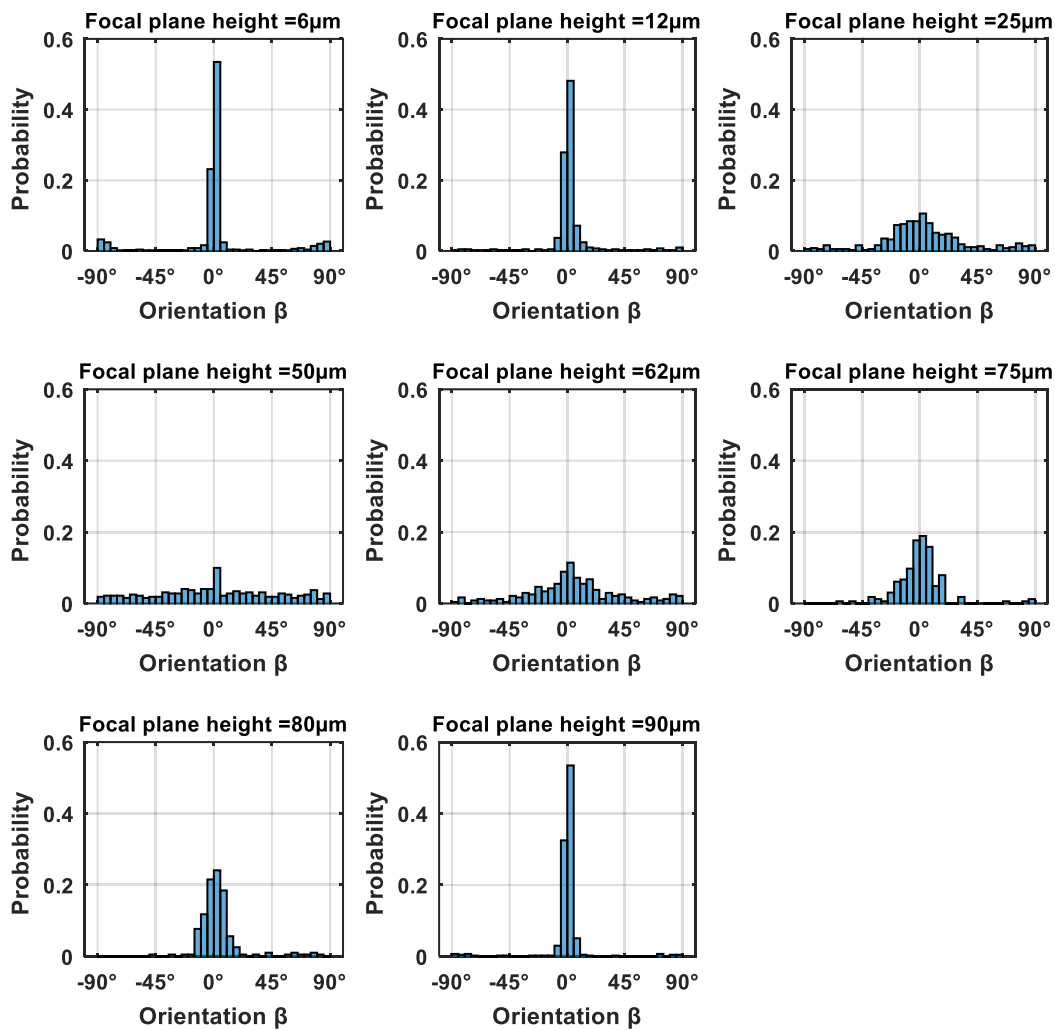


Fig. 13. Cell-orientation distribution in a one-day stored RBC unit at eight different heights in the flow chamber (ibidi I^{0.1}) under laminar flow (Flow rate = 0.5ml/min). Focal plane heights (FPH) are referred to the bottom wall. The more uniform orientation is observed near the bottom (FPH=6 μ m and 12 μ m) and top wall (FPH=90 μ m).

The cell orientation changes according to the flow rate and hence to the flow speed. Figure 14 shows histograms of the cell orientation at 12 μ m above the channel bottom for six different flow rates. For the flow chamber with the dimensions employed here ($w=5$ mm, $h=0.1$ mm), the maximal orientation of discocytes occurs at 0.5 ml/min. This flow chamber was also used for the morphometry of RBCs. In order to ensure maximal orientation of RBCs, the flow rate was adjusted to 0.5 ml/min throughout all measurements.

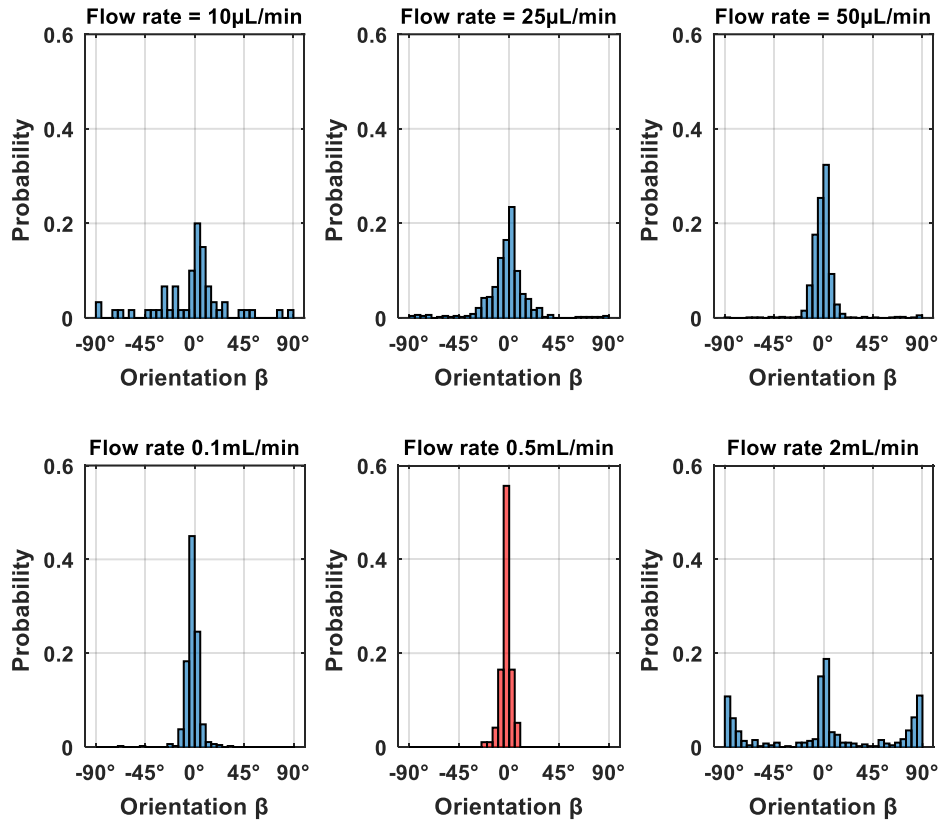


Fig. 14. Cell-orientation distribution in a one-day stored RBC unit at six different flow rates in the flow chamber (ibidi I^{0.1} channel width = 5mm). The focal plane height is adjusted to 12 μ m with respect to the bottom wall. The most uniform orientation is observed at 0.5ml/min (red).

The smaller the cross sectional channel area, the lower the flow rate required to orient the discocytes. This is evidenced in the similar orientation distributions obtained by using a flow chamber with a fifth of the standard channel width (Fig. 15). The cell orientation histogram at a flow rate of 0.1ml/min in the smaller flow chamber shows the same distribution pattern as the histogram at 0.5ml/min in the regular flow chamber. This is consistent with the theoretical shear rate depending proportionally on the flow rate and inversely on the cross-sectional area.

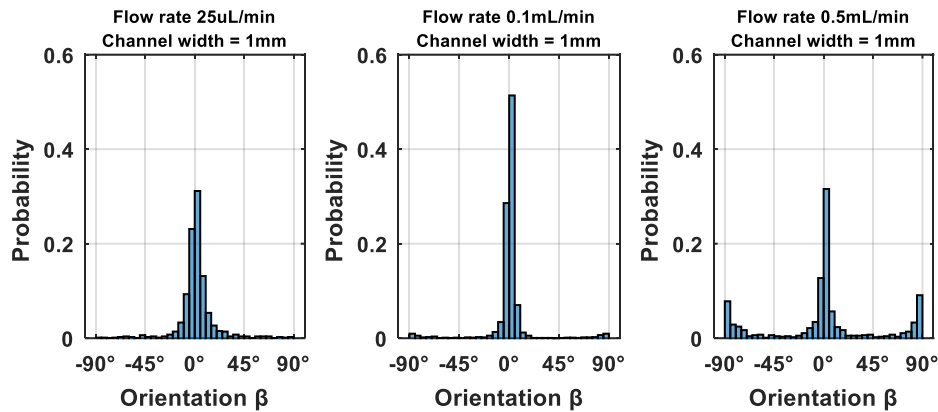


Fig. 15. Cell-orientation distribution in a one-day stored RBC unit at three different flow rates in a flow chamber (ibidi VI^{0.1} height = 100 μ m, width = 1mm). The focal plane height is adjusted to 12 μ m with respect to the bottom wall. The most uniform orientation is observed at 0.1ml/min s⁻¹.

According to this observations, a focal plane of 12 μ m above the channel bottom and a flow rate of 0.5 ml/min were chosen for the imaging and flow conditions of RBCs since the major proportion of discocytes rolled under these conditions.

3.5 RBC Morphology Categorization and morphological Features

During the RBC storage, progressive morphological changes were observed by imaging of samples periodically extracted using the setup described in 3.2. A set of characteristic erythrocytes captured by the microscope is shown in the figure 16. These cell micrographs represent the progressive morphological changes of stored RBCs. In particular, specific morphological markers of the cell membrane characterize the deterioration states of RBCs. The deterioration is categorized in three RBC stages (Fig. 16). The first stage corresponds to RBCs characterized by the regular smooth biconcave disc shape called discocytes (D). The second stage includes the manifestations of storage lesion in which bumps appear on the cell surface, become more numerous and finer, and the cells become more rounded. This stage comprises a set of several echinocyte sub-types E, which are described in [35]. Erythrocytes corresponding to the first echinocytic stage (E I) could not be always distinguished from D because they can still roll and their immature bumps are not always recognizable under flow conditions. Advanced deterioration of RBCs manifested through the loss of spikes, smooth sphericity and reduced cell diameter (third stage; spherocytes (S)). For parameterization of these characteristics, a customized algorithm developed in MATLAB (MathWorks Inc, version R2015a) processes micrographs by contour recognition and feature extraction. Border roughness (BR), texture inhomogeneity (T), non-circularity (NC) and equivalent diameter (ED) are calculated. From these, a feature vector of four coefficients is obtained that describes the

cell morphology and allows the association of each individual RBC with one of the three defined states.

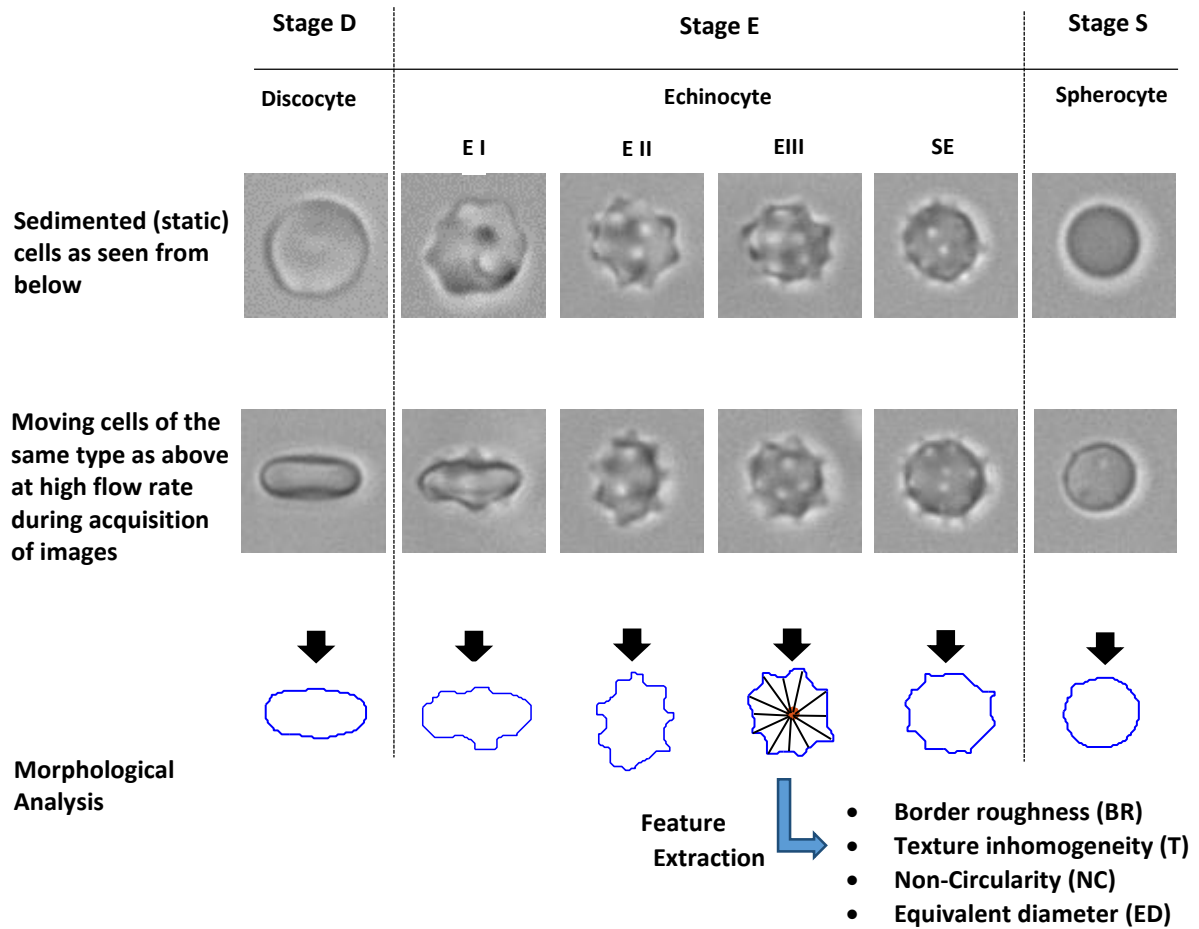


Fig. 16. RBCs showing the progression of morphological damage (from left to right) captured by the flashed microscope. The first row shows immobile sedimented (flow stopped) RBCs in optimized focus. The second row shows cells which move freely through the focus range centered on a position 12 μm above the flow channel's bottom. In the flowing state, the discocytes orient themselves perpendicular to the channel bottom, so that the observed profile is oval. E I, E II E III and SE are represented in this figure, however they are subsumed under class E.

The presence of spikes is detected through the border roughness of the cell outline in conjunction with texture inhomogeneity. The border roughness is measured by calculating the Fourier coefficients of the two-dimensional spatial cell contour. The texture inhomogeneity is determined by the entropy of the pixel intensities within the inner cell region [71]. Discocytes in rolling mode are recognized by their oval contour which is measured through the non-circularity feature. Aged RBCs (E III, SE and S) appear as a circular form in any perspective. Discocytes (D) can also appear circular depending on their momentary orientation during imaging but can be distinguished by their size, measured as equivalent diameter feature. This is calculated as the analogous diameter that defines a circle with the same area that is contained in the cell outline.

3.6 Algorithm Development

The developed algorithm has two main functions: image processing and classification. The image processing consists of the recognition of sharp RBCs in the images with the subsequent extraction of their morphological features. These tasks are called *cell segmentation* and *feature extraction* and form the basic modules of the image processing. Features, representing numerically morphological characteristics of RBCs, are then used to classify RBCs into one of the three defined morphological classes after the image processing. The following diagram (Fig. 17) shows the generated structure of the algorithm:

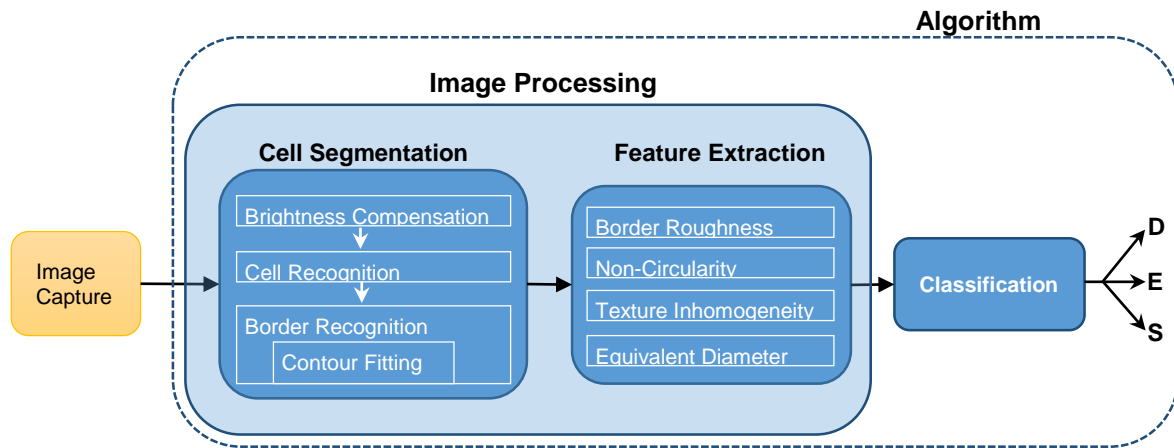


Fig. 17. Algorithm structure. Image processing and classification are performed by the algorithm. Cell Segmentation and Feature Extraction comprise the image processing task. Each of them is subdivided into modules of analysis. (D: Discocytes, E: Echinocytes and S: Spherocytes)

3.6.1 Cell Segmentation

The cell segmentation consists of three modules. The first module (brightness compensation) compensates the brightness inhomogeneity in the image and standardizes the mean pixel intensity to make the analysis invariant to differences in the illumination intensity (Fig. 18). The second module (cell recognition) recognizes sharp objects on the image which correspond to moving RBCs captured in the focus range of the in situ microscope. Sharp RBCs are thus first located in the image and then extracted as small RBC micrographs (140-by-140 pixels). The rest of image information is discarded. Finally, the third module (Border Recognition) performs a fine border recognition of the cell prior to the feature extraction.

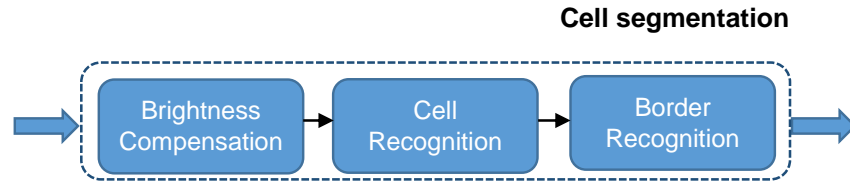


Fig. 18. Cell segmentation module with the corresponding subtasks.

3.6.1.1 Brightness Compensation

The variable cell locations between consecutive frames make it possible to obtain the illumination inhomogeneity pattern of the image background (e.g., vignetting) by computing the average of a significant number of images (>30). In this way, a background image I_{BG} is generated for brightness compensation of each incoming image I_{IN} (Fig.19). The background image replicates the same illumination pattern of the cell images but without any object on it (Fig. 20a and 20b). The following block diagram describes in detail the process of this compensation.

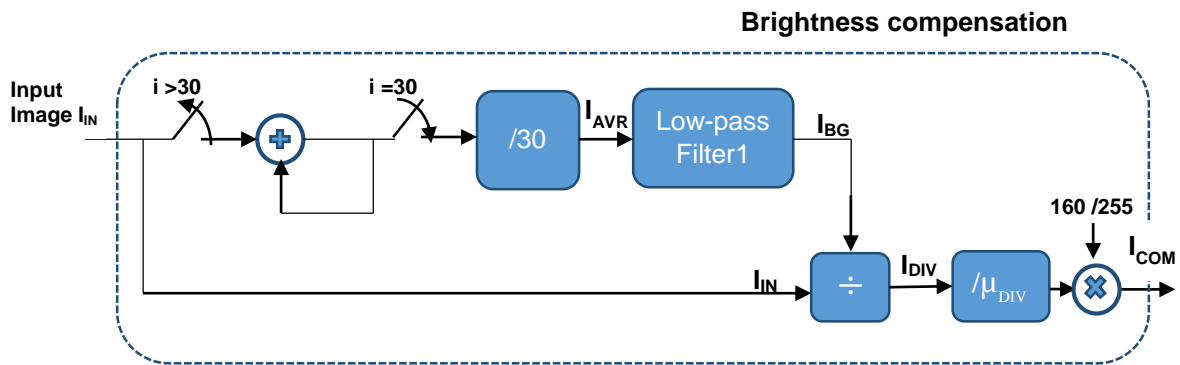


Fig. 19. Brightness compensation method. The first thirty input images are averaged (I_{AVR}) to obtain a background image (I_{BG}) after previously being filtered through a low pass filter. The module $/\mu_{DIV}$ divides the incoming image I_{DIV} into its mean value μ_{DIV} . I_{COM} is the resulting compensated input image.

The pixel values of the first thirty acquired cell images are averaged and the resulting image I_{AVR} is passed through a low pass filter to eliminate subtle traces of cells. For this purpose, a Gaussian smoothing (kernel size: 30×30 , $\sigma = 20$) over I_{AVR} is carried out. Considering that the illumination inhomogeneity pattern remains constant during the measurements, a unique background image is used for the compensation for each sample analysis.

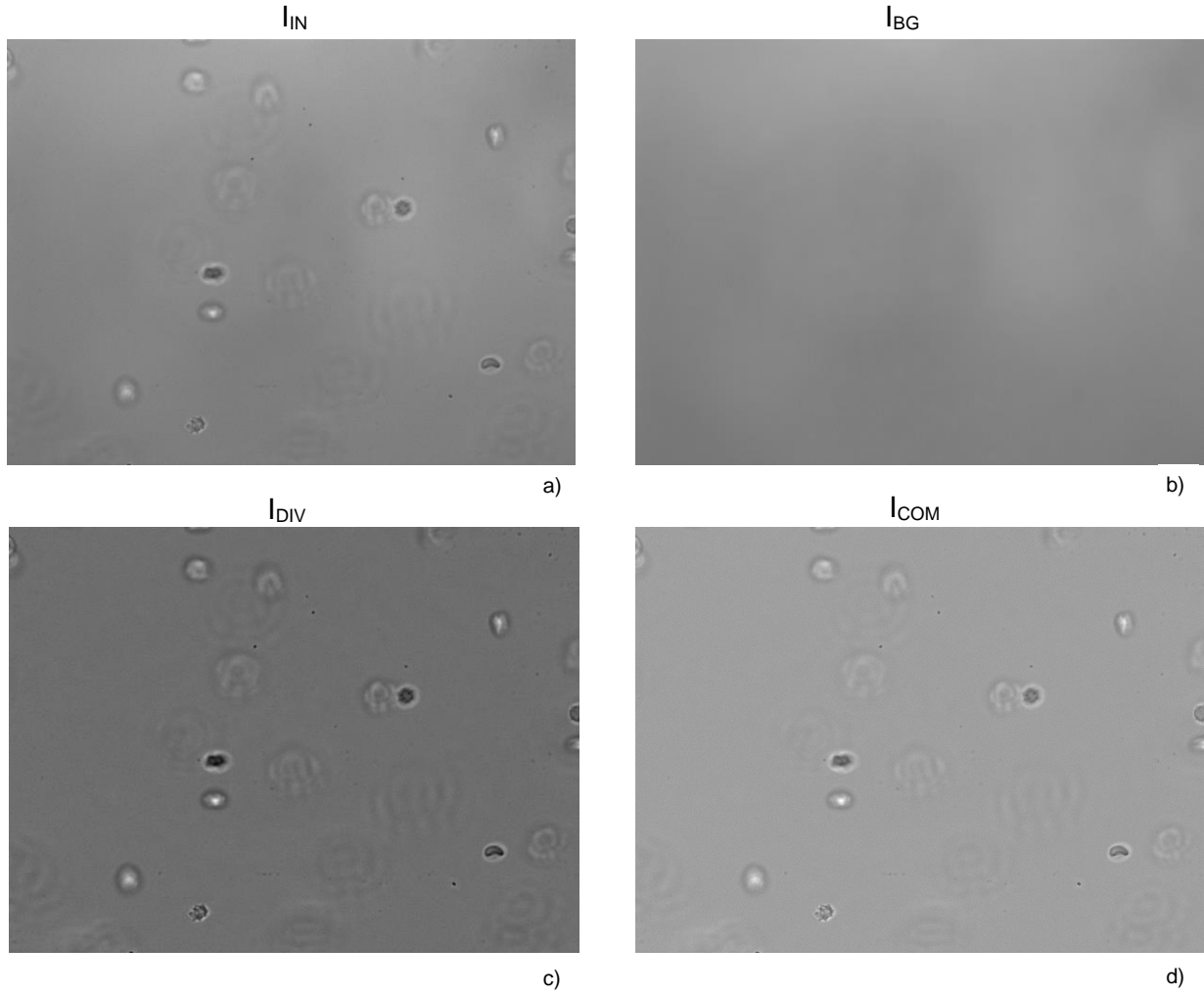


Fig. 20. Image processing for brightness compensation. a) Input image I_{IN} . b) Background image I_{BG} . c) Division image $I_{DIV}=I_{IN}/I_{BG}$. d) Compensated image I_{COM}

The division of the input image by the background image results in a new image I_{DIV} with uniform background intensity (Fig. 20c). In the case of cell pixels in I_{IN} , they are also proportionally compensated with respect to the background intensity in their corresponding image location in I_{BG} . This ensures a correct compensation of cell pixels. Afterwards, the mean intensity of the image I_{DIV} is standardized to 160 so that the image analysis is consistent with the gray intensity levels of all images. This chosen value corresponds to a medium gray scale brightness intensity suitable for the visual representation of the images. The resulting compensated cell image I_{COM} is computed as follows:

$$I_{COM} = \left(\frac{160}{255} \right) \frac{I_{DIV}}{\mu_{DIV}}$$

Where μ_{DIV} is the mean intensity of I_{DIV} .

3.6.1.2 Cell Recognition

After brightness compensation, the cell recognition module selects all sharp cells in the image and generates small cell micrographs (140x140 pixels) in order to be processed by the feature extraction module.

The homogeneity of the cell distribution into the flow chamber leads to minimal variation in the percentages of morphological stages at different focal planes along the channel height. For this reason, the set of all recognized sharp cells at a specific channel height represents statistically the morphological state of the corresponding sample. Figure 21 shows the cell recognition process.

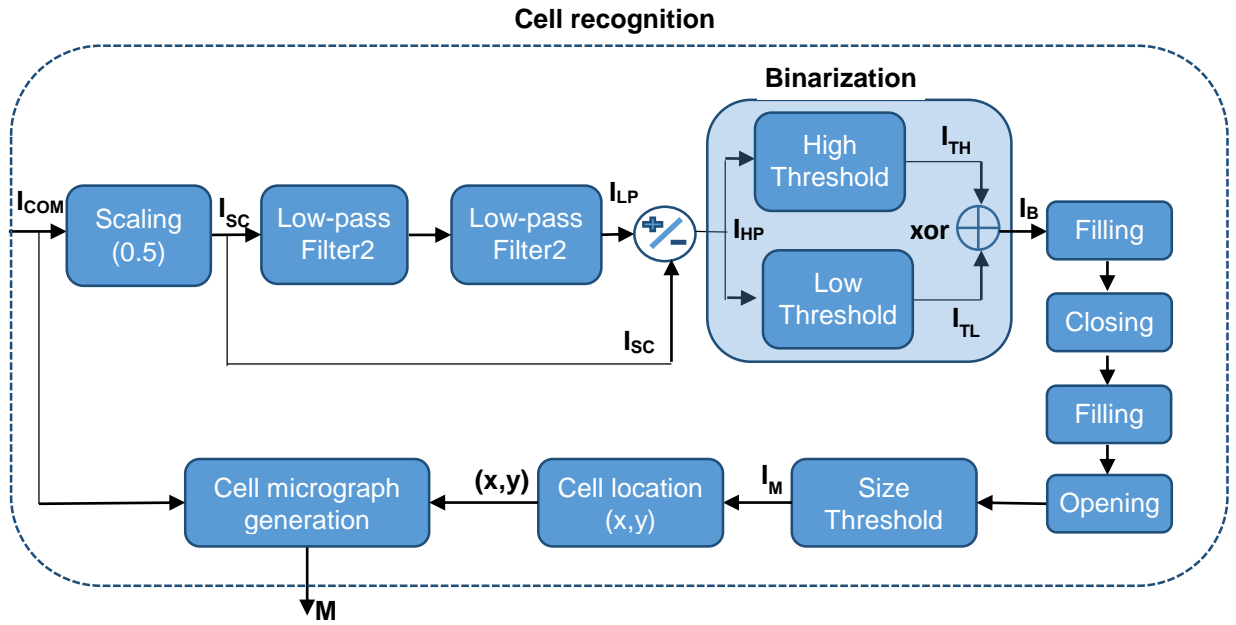


Fig. 21. Cell recognition process. Brightness-compensated image I_{COM} is scaled (I_{SC}) and high-pass-filtered (I_{HP}) for binarization. (XOR performs the logical operation exclusive OR between the two binary input images I_{TH} and I_{TL}). Morphological operations are performed over the binarized image I_B (Filling, Closing and Opening). Cell micrograph M is obtained after the calculation of the central point (x,y) of the cell area in the resulting binary image I_M after morphological operations.

The purpose of this module is the spatial location of sharp cells in the image, so that each such cell can be cut out as one individual micrograph. For that purpose, the compression of information is advantageous in order to speed up the image processing and reduce the computational load during this process. The input image is thus resized by a factor of 2 in each dimension by which the information is compressed to a quarter of its original size. The scaled image (I_{SC}) is then passed twice through a Gaussian low pass filter (Kernel Size 5x5, Sigma 1). The first filtering blurs the image to eliminate high frequency noise. The second filter

intensifies the effect of the first smoothing by blurring again the image. The subtraction of low-pass-filtered image (I_{LP}) from the resized image (I_{sc}) results in a high-pass-filtered version (I_{HP}) of the original image. This image contains the traces of the high contrast regions (high frequencies) commonly located at the edge of the sharp cells. The I_{HP} is represented by positive and negative decimal values with respect to the brightness of the background.

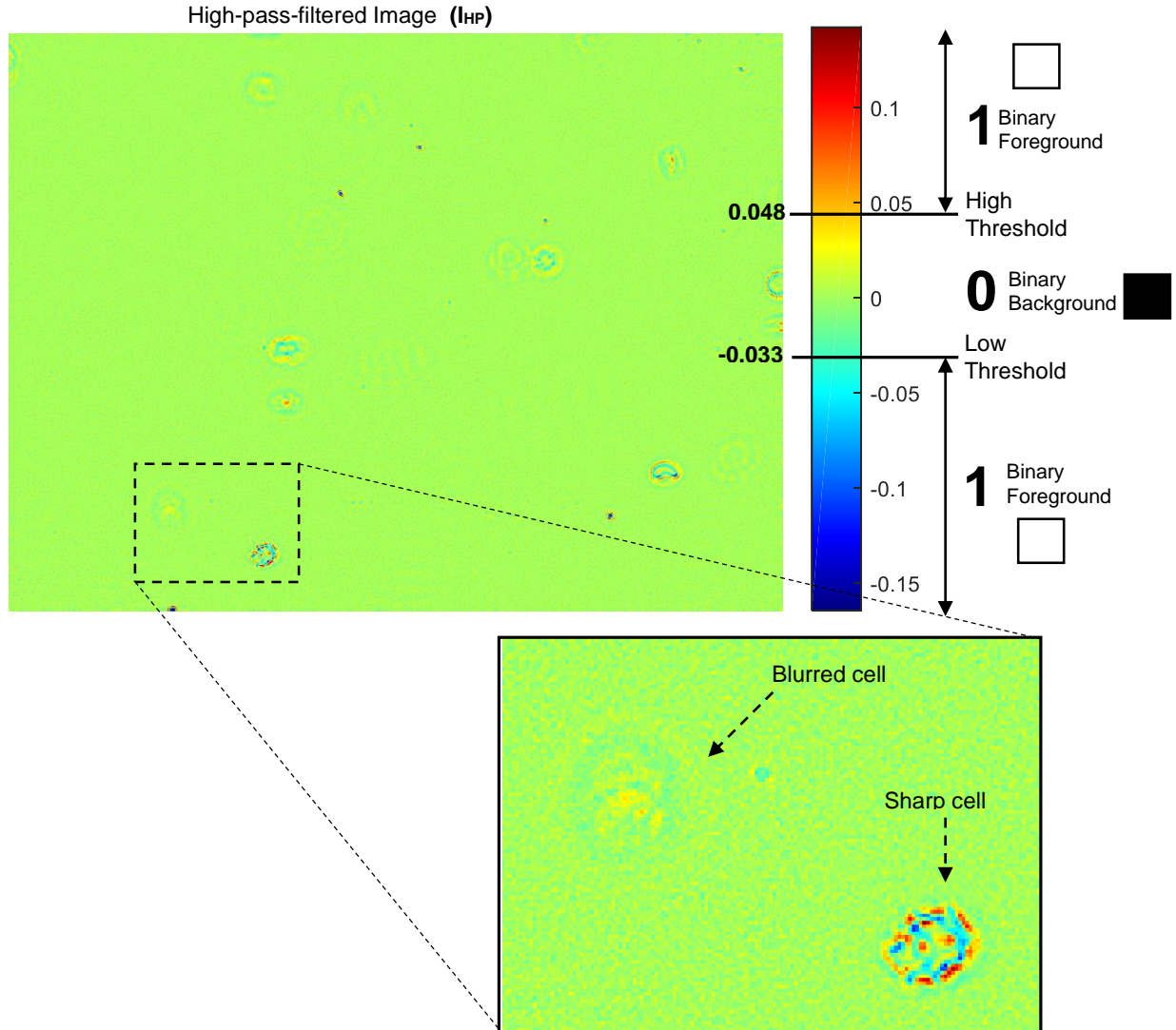


Fig. 22. One channel high-pass-filtered image I_{HP} and threshold values for binarization with color representation. Upper threshold: 0.048. Lower threshold: -0.033. Between these values pixels are set to zero.

Therefore, I_{HP} is binarized by setting pixels of interest (cell pixels) to “1” and the rest to “0” according to two pre-established threshold values for positive and negative pixels respectively as shown in the figure 22. The binarized image I_B allows the creation of regions of interest corresponding to the cell body to be recognized as an object. Instead of using a single threshold value operating over the pixel values of I_{HP} , threshold values were defined for positive and negative values of I_{HP} in order to have a better binarization adjustment. That implies that

two binary images (I_{TH} and I_{TL}) are generated representing positive and negative brightness changes in the original image I_{SC} . In this way, positive values of I_{HP} above a upper-threshold of 0.048 (representing normally sharp cell borders and internal cell changes) are set to the binary state “1” (*foreground-points*), otherwise they are set to “0” (*background-points*). Similarly, negative values of I_{HP} below a lower-threshold of -0.033 are set to “1”, otherwise to “0”. In order to obtain a single binary image (I_B) with all information, both binary images are added by means of the logical XOR operation (Fig. 23).

The white foreground pixels are not completely connected and do not form closed cell boundaries due to sections of mild contrast between the cell contour and the image background. In addition, small isolated foreground structures in I_B which correspond to pixels of blurred cells cannot be suppressed at all because they override the threshold limits. For that reason, a sequence of binary morphological operations must be applied to close and fill areas based on foreground-point connections and to remove small isolated structures.

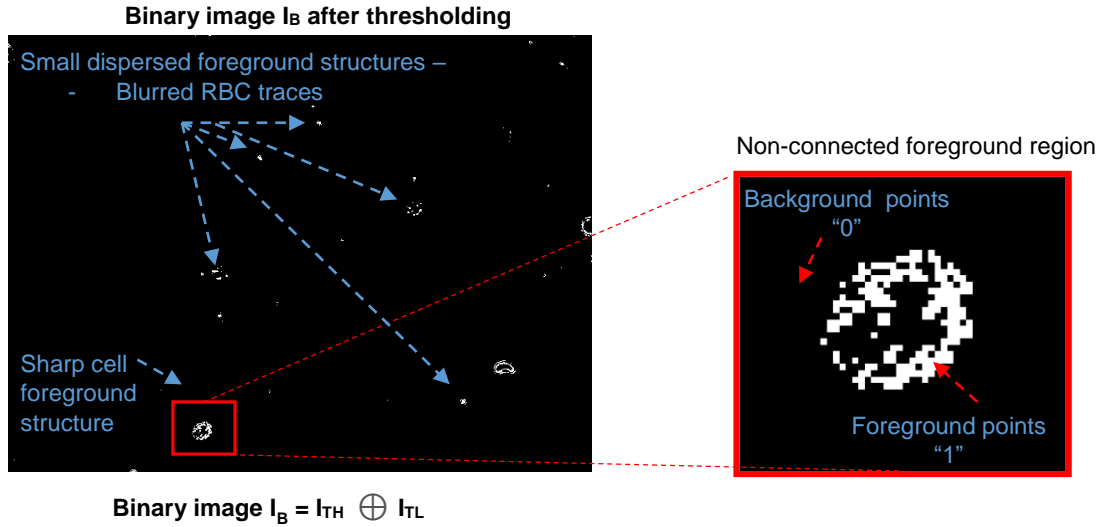


Fig. 23. Binary Image I_B with remaining traces of blurred RBCs (left). Resulting foreground points of a sharp RBC (right).

The morphological operator “*filling*” fills holes within closed boundaries contained in I_B . A subsequent morphological “*closing*” performs the enclosure of the remaining open structures by using a square 7x7 matrix as structural element. The size of this matrix assures the enclosure of almost all open boundaries of objects in the binary image and the filling of the same. Subsequently, an “*opening*” operation removes all small fragments dispersed in the binary image e.g. weak traces of blurred cells. Finally, a size thresholding completes the removal of medium-sized foreground structures that are associated with traces of bright blurred cells or intermediate focused cells. As the result, a “clean” binary image I_M is obtained that

contains only full foreground areas (blobs) as shown in the figure 24. A Blob is a group of connected pixels forming a single entity representing the object to be analyzed, i.e. sharp cells located in the same spatial location of the gray-scale image I_{SC} .

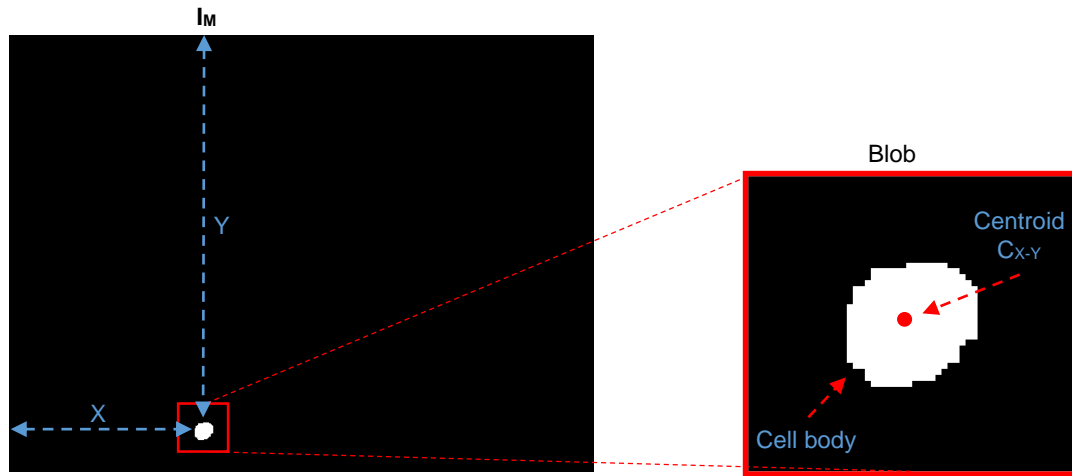


Fig. 24. Resulting binary Image I_M after morphological operations (left). Isolated foreground points were removed and the large concentration of foreground points were connected to form the cell blob (right).

As last step of this module, a cell micrograph M (140x140 pixels) is extracted from the full size input image I_{COM} by using the X-Y coordinates of the central point $C_{X,Y}$ of the cell area as center of the micrograph. This point is calculated as the mean value of the pixel coordinates belonging to the cell area. The result of this process is shown in the figure 25.

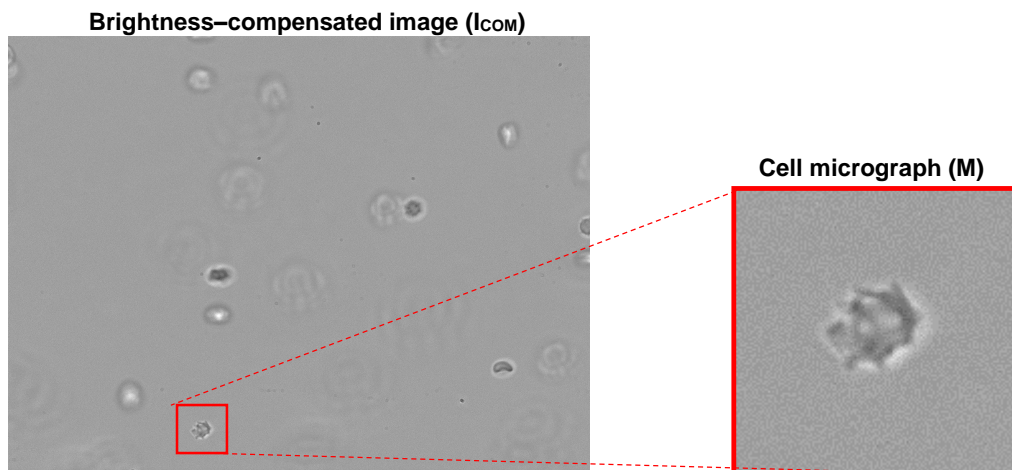


Fig. 25. Cell micrograph generation based on the X-Y coordinates of the binary blob.

3.6.1.3 Border Recognition

The border recognition module operates only over individual cell micrographs. In this way, the cell border can be more accurately determined than in the first segmentation process that was only used for the localization of the cells. From the cell border, morphological features such as border roughness, non-circularity and size are calculated. For this purpose, a similar set of frequency filtering, thresholding and binary operations as described above is performed in this module (Fig. 26).

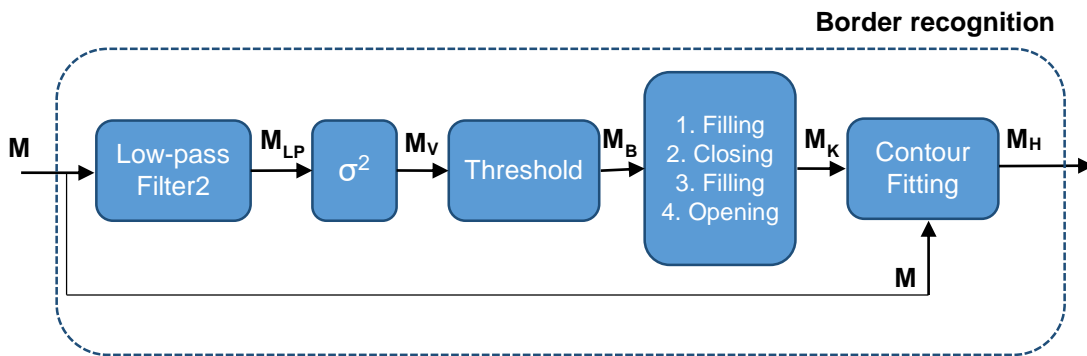


Fig. 26. Border recognition process. A variance transformation σ^2 over the low-pass-filtered cell microgram M_{LP} is carried out to obtain the variance micrograph M_V . After thresholding, morphological operations over the binary micrograph M_B are performed to obtain the resulting binary micrograph M_K representing the cell area. Contour fitting operator performs the fine calculation of the cell contour. M_H is the output binary micrograph of this process

First, noise filtering in the cell micrograph is applied by using a Gaussian filter (Kernel size 5x5, Sigma1). Subsequently, high frequency filtering is implemented in the form of variance transformation of the smoothed micrograph (M_{LP}) (Fig. 27). The local variance of pixel intensities within 5x5 square regions in M_{LP} is calculated and assigned to the center pixel of the region. The resulting variance micrograph M_V emphasizes pixels where strong brightness changes occur. In this sense, the variance transformation operates similarly to a high pass filter.

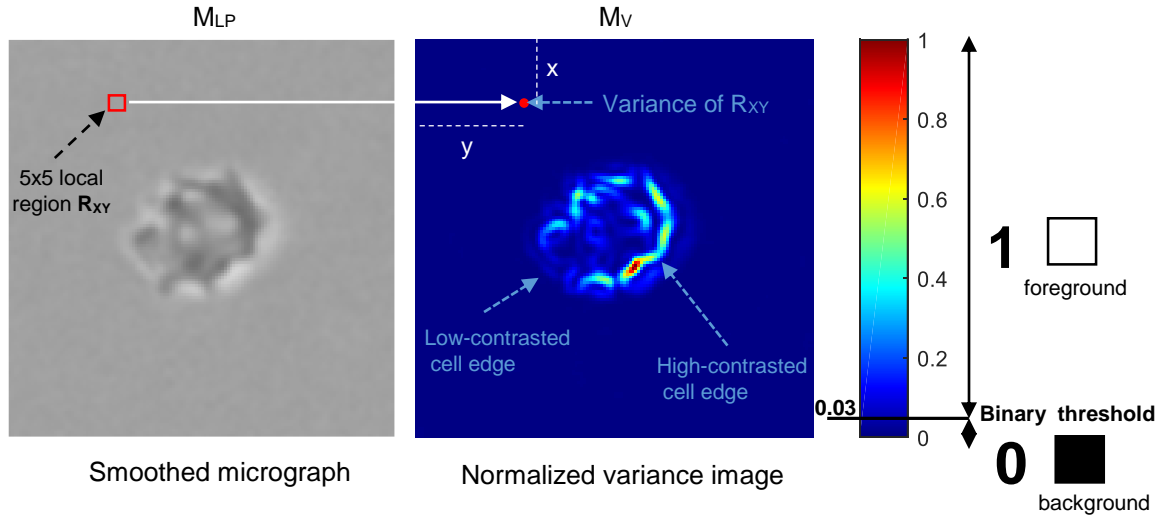


Fig. 27. Low-pass filtered cell micrograph (left) and normalized variance transformation. Threshold value for binarization: 0.03.

Areas of homogeneous pixel intensities in M_{LP} are equivalent to variance values close to zero. The largest values of variance in M_V correspond to cell contour regions. The binarization of the normalized variance image is made by setting the binary threshold to 0.03. This threshold value allows to obtain a foreground structure that describe the general cell body minimizing the area over estimation. As described in the previous section, morphological operations are then used at this point to generate compact foreground structures representing the cell bodies. For this, the same sequence of operations as in the previous section is applied to the binary micrograph M_B and subsequently a preliminary cell contour is calculated from the resulting blob of the binary micrograph M_K (Fig. 28). The contour corresponds to the boundary pixels that outline the blob.

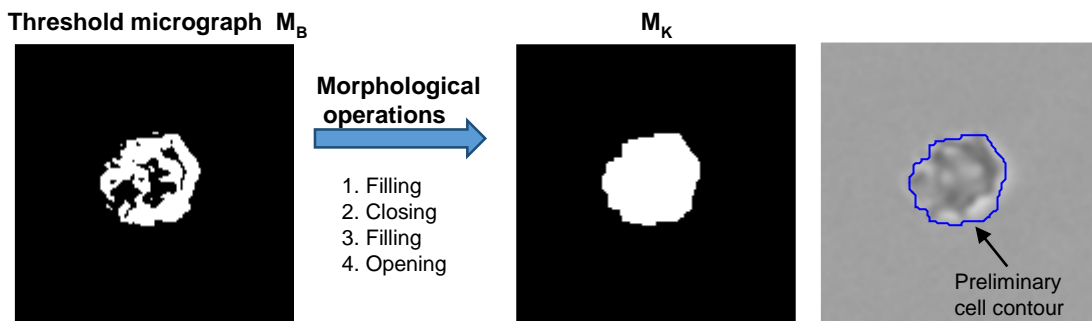


Fig. 28. Cell micrograph binarization and contour recognition.

This cell contour is only preliminary, since a more precise cell contour detection must take into account irregularities of the cell border contrast and additional optical effects around the cell boundary.

Discontinuities of the cell border in the image are usually present in the original micrograph and no threshold value alone can therefore delineate perfectly the real cell contour. An additional factor hindering the finding of the true cell contour is the halo effect around the cell contour. The halo consists of a bright or dark edge around the object caused by light diffraction. This effect is more evident in unfocused cells but it is still present in focused cells. Commonly, cells located between the focal plane and the objective are imaged as darker objects with bright halos, while cells beyond the focal plane exhibit the opposite image characteristics (Fig. 29).

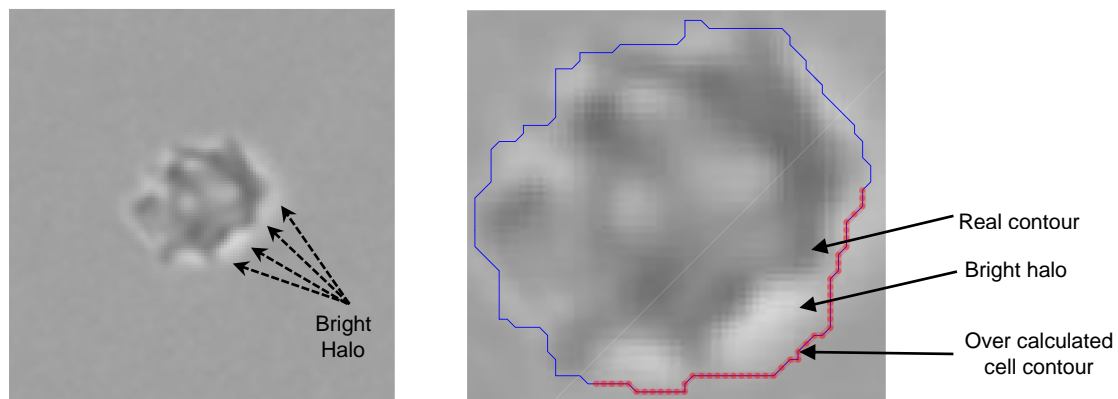


Fig. 29. Bright halo around the border of a well-focused RBC (left). Over calculated cell contour in the halo region (right).

The halo contrasts with the micrograph background around the periphery of the cell and it generates an image artefact which obscures the cell contour. This is a serious obstacle for the determination of structures such as the cell spikes of echinocytes. In order to deal with this effect, a specific module for a more accurate contour fitting was developed.

3.6.1.3.1 Contour Fitting

The previous image processing generates for each sharp cell a binary cell micrograph M_k containing a coherent area (blob) representing the cell body. The contour fitting process works by cyclically eroding (contracting) the cell area in the binary micrograph M_k at each periphery point if its corresponding gray-scale pixel on M remains below (or above) a pixel intensity threshold that represents the real cell boundary. This threshold is defined in accordance with the characteristic of the halo. Cells with bright halo exhibit dark cell borders (and internal mean brightness below 163) and vice versa. Accordingly, the boundary contraction is intended to override the region of the halo effect until the binary cell boundary fits with the real cell contour. The following flow diagram describes the contour fitting logic.

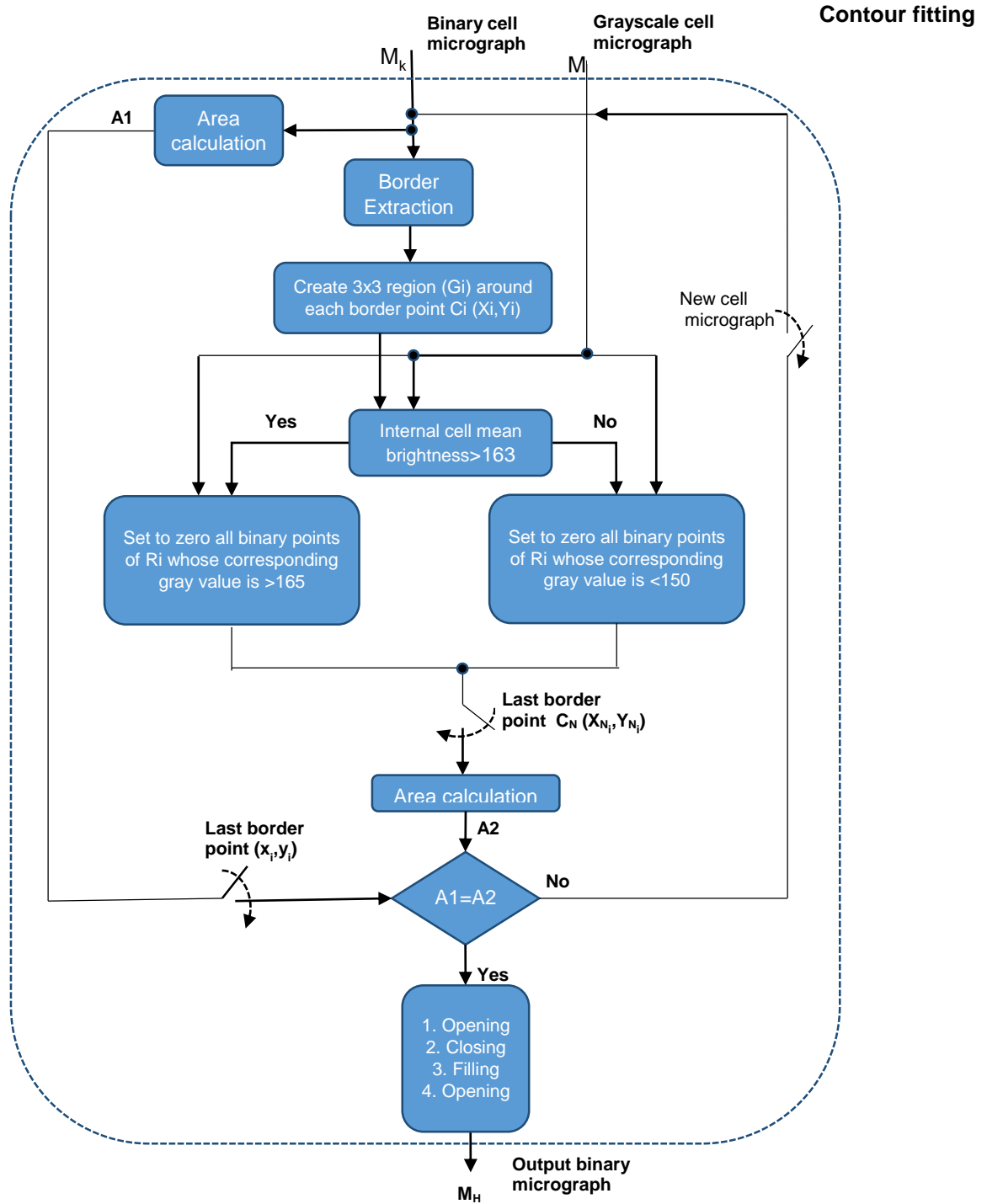


Fig. 30. Contour fitting algorithm. Binary M_k and the corresponding gray scale micrograph M as input of the module.

Firstly, border points C_i with coordinates X_i, Y_i are extracted from the blob. For each point C_i , a region G_i of size 3×3 centered at C_i is defined in both the gray-scale and binary micrograph. If the internal cell mean brightness in M is below 163, then this indicates that the halo is bright and the cell border is dark. In this case, the binary border boundary must be contracted until darker pixels of M are encountered. Dark pixels are defined to be pixel intensities (PI) below

165 and it constitutes the value of the erosion threshold for cells with bright halo. Consequently, each binary pixel in the region G_i is set to zero (blob contraction) if its corresponding brightness in M is higher than 165 until a particular C_i point reaches the true cell border ($PI < 165$). If no more changes take place in all regions of the contour, the blob contraction finishes. In order to assess this condition, the area A_2 of the resulting blob in each iteration (output blob) is compared with the area A_1 of the previous blob (input blob). If both areas are equal, the blob contraction finishes.

In some cases, the blob reduction can override the true cell contour if there is not sufficient contrast with the micrograph background. Sometimes, this is corrected through the subsequent morphological operations, but often the precision of the fitting is severely compromised. However, these cases are statistically not significant and therefore they do not merit a special analysis in the present study.

After the blob contraction, morphological operations are carried out over the resulting blob in order to remove isolated foreground pixels and refine the contour around the cell blob. As result, a blob M_H fitting the true cell contour is obtained (Fig. 31). This is the starting point for the feature extraction based on the cell outline, explained in the next chapter.

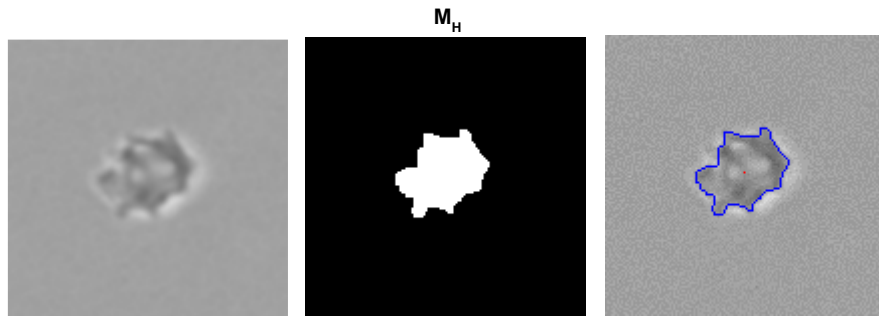


Fig. 31. Noise-filtered cell micrograph M_{LP} . Resulting blob M_H after contour fitting and resulting cell contour (right).

3.6.2 Feature Extraction

The feature extraction module computes morphological characteristics of erythrocytes based on both the cell contour and the pixel intensities of the cell micrograph calculated in the previous section (Fig. 32). As mentioned, a set of 4 features is defined in this study for the morphological characterization of erythrocytes. Three of them are based on the cell contour (non-circularity (NC), border roughness (BR) and equivalent diameter (ED)). The fourth feature

value is a measure of the texture inhomogeneity (T) in the inner cell region. The following diagram shows a flow diagram of the feature extraction process.

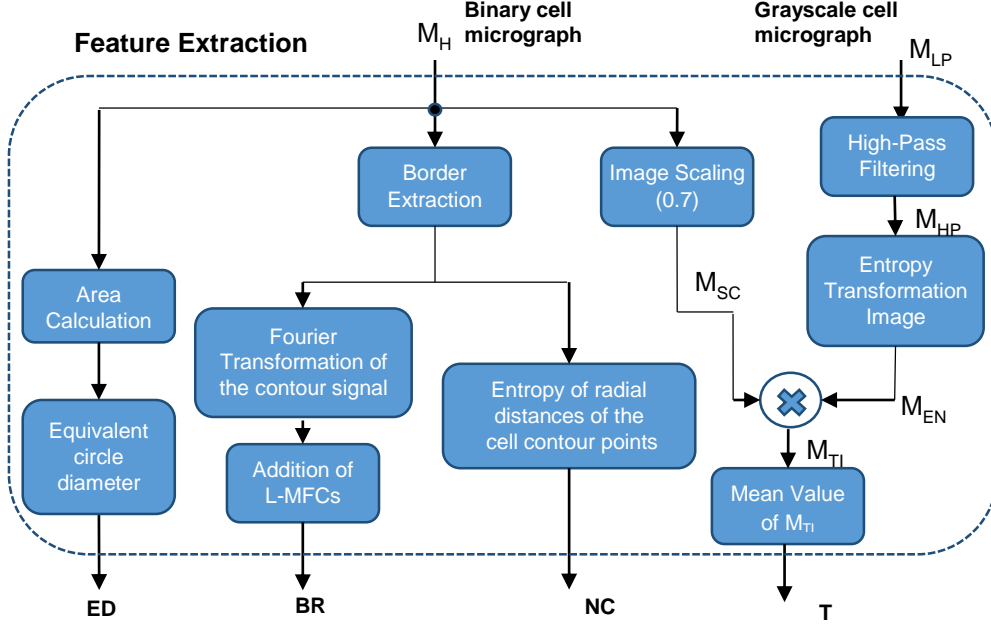


Fig. 32. Feature extraction process. Four features are calculated: Equivalent diameter (ED), Border Roughness (BR), Non-Circularity (NC) and Texture Inhomogeneity (T). Border Roughness (BR) is calculated as the addition of the last medium frequency components (L-MFCs) of the Fourier spectrum of the cell contour signal.

3.6.2.1 Border Roughness

At a digital representation level, the cell contour is a closed trajectory composed of connected pixels that outline the cell. These are the external pixels of the binary cell blob M_H generated in the cell segmentation process. Each pixel can be described as a point p_n with Cartesian coordinates (x_n, y_n) . Assuming a central point within the cell outline, p_n can also be expressed in polar coordinates.

The cell roughness is caused by small protrusions (bumps or spikes) in the cell surface. This is seen as an oscillating radius r_i in a short segment of consecutive border points in the cell outline (Fig. 33). In order to parametrize this fluctuating behavior of r_i , the function $r_i(\theta_i)$ is analyzed by means of Discrete Fourier Analysis (DFT).

In order to perform the DFT, the cell contour must be expressed as a contour function $z(n)$ (Fig. 33). The contour is a closed shape and for that reason, it is a periodic signal that can be expressed as a complex function:

$$z(n) = (x(n) - x_c) + j(y(n) - y_c), \quad n = 0, 1, \dots, N - 1$$

whereby N is the total amount of contour points and (x_c, y_c) are the coordinates of the shape centroid. DFT transforms a periodic signal $z(n)$ into spectral components F_k as follows:

$$F_k = \sum_{n=0}^{N-1} z(n) \cdot e^{-\frac{2\pi}{N} jkn} \quad k = 0, \dots, N-1$$

The spectral components F_k are known as Fourier descriptors (FDs) and represent the spatial outline signal $z(n)$ in the frequency domain. The first F_k coefficients (low frequency terms) of the DFT sum describe the global shape and are normally used for rough shape reconstruction or shape characterization (Fig. 36a). High frequency components capture finer details such as changes in direction in small segments of the outline (Fig. 36c). In the present study, such details correspond to cell bumps typical of the echinocytic shapes.

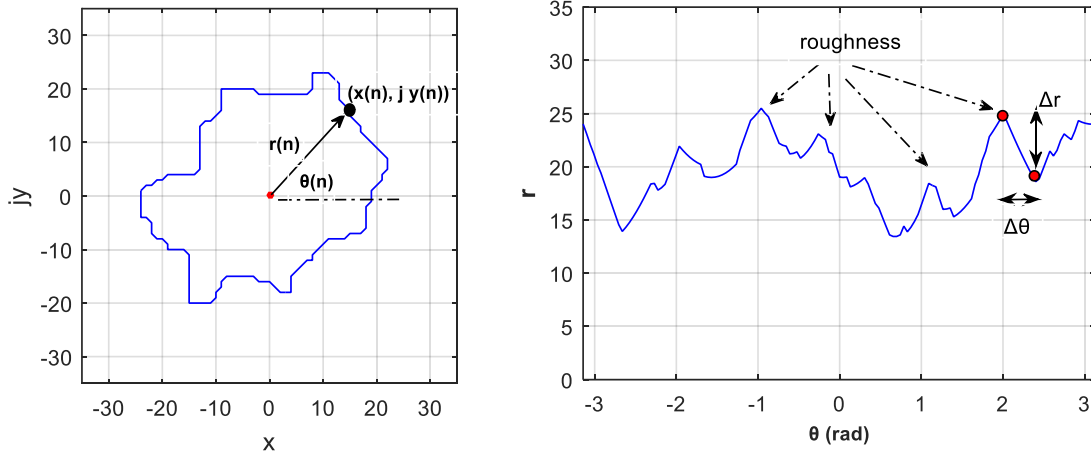


Fig. 33. Cell border as complex function $Z(n)$ in the coordinate system (x, y) (left). High cell roughness manifested through the oscillation of the function $r(\theta)$ (right).

FDs are complex numbers whose magnitudes are invariant under rotation and translation of the shape in the image plane. Naturally, F_0 corresponds to the DC (offset) component of the shape. This means that it depends on the location of the center point in the coordinate system. Only this coefficient is influenced by a translation of the object. For that reason, F_0 is not taken into account for the shape representation. The second FD-coefficient F_1 contains the fundamental frequency of closed shapes which corresponds to a circle (Fig. 34). The magnitude F_1 is proportional to the circle radius i.e., to the shape size. The next frequency components deform the circle to adapt to the shape. Their amplitudes are proportional to the shape size. FDs are normalized with respect to F_1 so that they remain invariant to the shape size. In general, the invariant Fourier series F of a shape can be expressed as:

$$FI = \left(\frac{|F_2|}{|F_1|}, \frac{|F_3|}{|F_1|}, \dots, \frac{|F_{N-1}|}{|F_1|} \right)$$

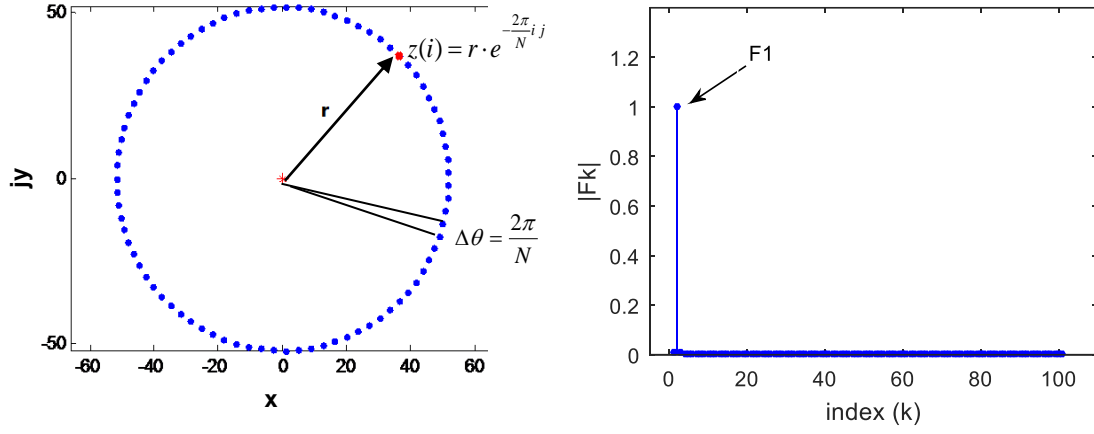


Fig. 34. Fourier transformation magnitude of a perfect circular form (left). Only the low frequency component F1 is required to describe the circle.

The high frequency components (HFCs) are located in the middle part of the Fourier series while the low frequency components (LFCs) are around the edges of the spectrum (Fig. 35b). Starting from the fundamental circle, LFCs stretch the circle and generate soft curves outlining the overall cell shape. Medium frequency components MFCs intensify the concavities or convexities of those curve outlining cell bumps. HFCs make the existing vertex more angular. In the case of cell contours, HFC-amplitudes are very low because of the lack of big prickly protrusions (large Δr with small $\Delta \theta$). Therefore, HFCs are not a relevant source of information for the spectral analysis.

In order to identify echinocytes, whose principal characteristic is the appearance of bumps, the roughness analysis is based on MFCs. In this study, the last MFCs of the spectrum (L-MFCs) were chosen to characterize the cell shape. In echinocytic contours, L-MFCs show the largest amplitude and variability generated by the contour bumps in comparison with their analogous MFCs of the beginning of the spectrum (F-MFCs). The border roughness feature value (BR) is defined as:

$$BR = \sum_{k=3}^8 \left\| \frac{F_{N-k}}{F_1} \right\|$$

Where N is the total number of FDs.

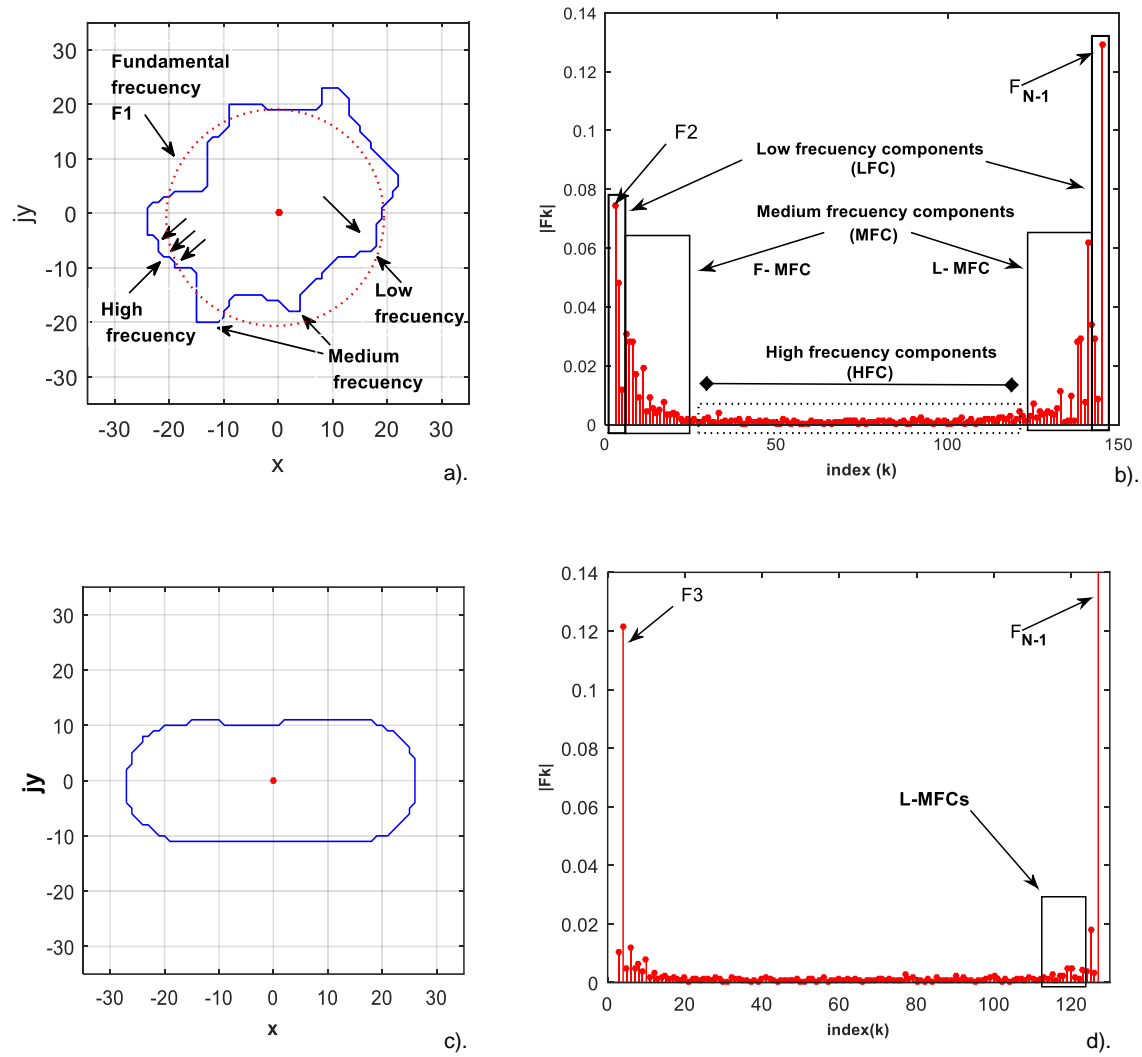


Fig. 35. Spectral analysis for echinocyte and discocyte contours. a) Identification of frequency components around the echinocyte border and b) corresponding Fourier transformation magnitude. c) Typical smooth border of the oval profile of an oriented discocyte and d) corresponding Fourier transformation.

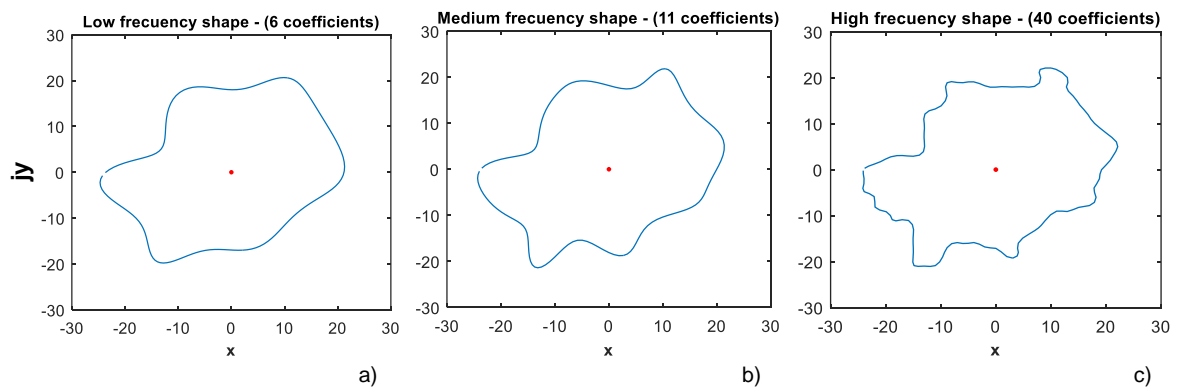


Fig. 36. From left to right, progressive echinocyte border reconstruction with LFC, MFC and HFC. Each reconstruction takes the first 6, 11 and 40 coefficients respectively.

3.6.2.2 Non-Circularity

This feature refers to the degree of deviation of the cell outline from a circle. It constitutes the most sensitive parameter to distinguish discocytes from the two other erythrocyte types defined in the present study. Settled discocytes are seen as circular shapes with smooth border. However, in a laminar flowing suspension and under specific shear stress, discocytes tend to orientate vertically with their rotation axis perpendicular to the flow direction. This means that an oval profile is seen by the inverted microscope. This oval outline is the strongest marker for discocyte recognition by using image processing. Mature echinocytes and spherocytes do not exhibit this characteristic due to their isotropic shape without regard to the flow conditions.

In this study, the non-circularity (NC) feature value is defined based on the variation of distances between each border point and the center of mass of the cell outline. Border points of a perfect circular form have a constant radius and therefore the radial variation is zero. Instead, an oval form exhibits a high variability of the radius and consequently the highest radial variation of the three defined morphological classes. As variability measure for the radial distances, the information entropy was used (Fig. 37).

Each cell contour generates a histogram of radial distances grouped in intervals R_k of size 5. The histogram is normalized to obtain the probabilities p_k of each R_k .

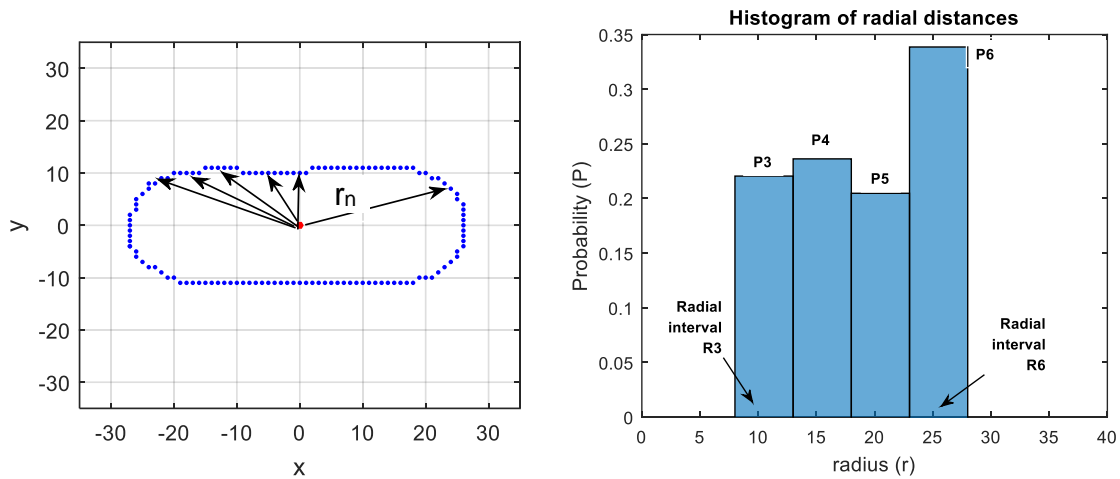


Fig. 37. Histogram of radial distances of an oriented discocyte. Bin range: 5 (radial interval)

Based on these probabilities, the entropy EN is defined by the following formula, assuming that all intervals with zero probability are excluded.

$$EN = - \sum_k^M p_k \log(p_k), \quad \text{whereby } p_k = \frac{h_k}{N}, \quad M: \text{Total number of radial intervals},$$

h_k : frequency of the radial interval R_k , N : total number of countour points

Radial distances r_n of a circular form (e.g. mature echinocytes and spherocytes) do not vary significantly and therefore almost all r_n fall into a single R_k . In terms of information entropy, that means redundancy of information and consequently, EN tends to be zero. A perfect circle has zero non-circularity i.e., zero entropy because there is no variance of radial distances. In contrast, EN is highest when all events (radial intervals) have the same probability (high variance of radial distances) which is the case of asymmetrical forms with respect to the shape centroid. Considering the morphological classes and their corresponding cell borders, the maximal asymmetry is found in oriented discocytes caused by their oval contour. The diversity of radial distances of this form is represented by a wide distribution of radial intervals with similar probabilities according to their histogram. The value of EN is thus directly assigned to the non-circularity feature:

$$NC = EN$$

3.6.2.3 Texture inhomogeneity

Cell bumps can only be observed as projections onto the 2 dimensional image plane; the third dimension escapes the contour analysis. Irregularities occurring within the internal region of the cell image manifest themselves only as fluctuations of pixel intensities, i.e. as texture inhomogeneity in the cell body. Echinocytes show high variability of pixel intensities, which is a clear signal of bump presence. The texture inhomogeneity measure characterizes the degree of brightness variation in the inner cell region. This variation is calculated through the entropy of pixel intensities of the internal cell region.

Firstly, the noise-reduced cell micrograph M_{LP} is passed through a high-pass filter to eliminate slight intensity variations and enhance significant changes in the inner cell region (Fig. 32). The high pass-filtered micrograph M_{HP} is then transformed into an entropy image M_{EN} where each pixel assumes the local entropy value $E_{i,j}$ of the 5-by-5 neighborhood around it (Fig. 38). Each local entropy $E_{i,j}$ is based on the histogram of 25 gray-scale values arranged around the pixel $M_{HP}(i,j)$:

$$EN_{i,j} = - \sum_k p_k \log(p_k), \quad \text{whereby } p_k = \frac{h_k}{25}, \quad h_k: \text{frequency of the pixel intensity } k$$

The resulting entropy image M_{EN} is then multiplied by the corresponding binary cell micrograph M_{SC} which acts as a binary mask to set as zero all entropy values outside the inner cell region. The binary blob in M_{SC} is downsized prior to this by a factor of 0.7 with respect to the resulting blob in M_H in order to exclude the cell boundary which contains highly contrasted regions that alter the consistency of the texture inhomogeneity values.

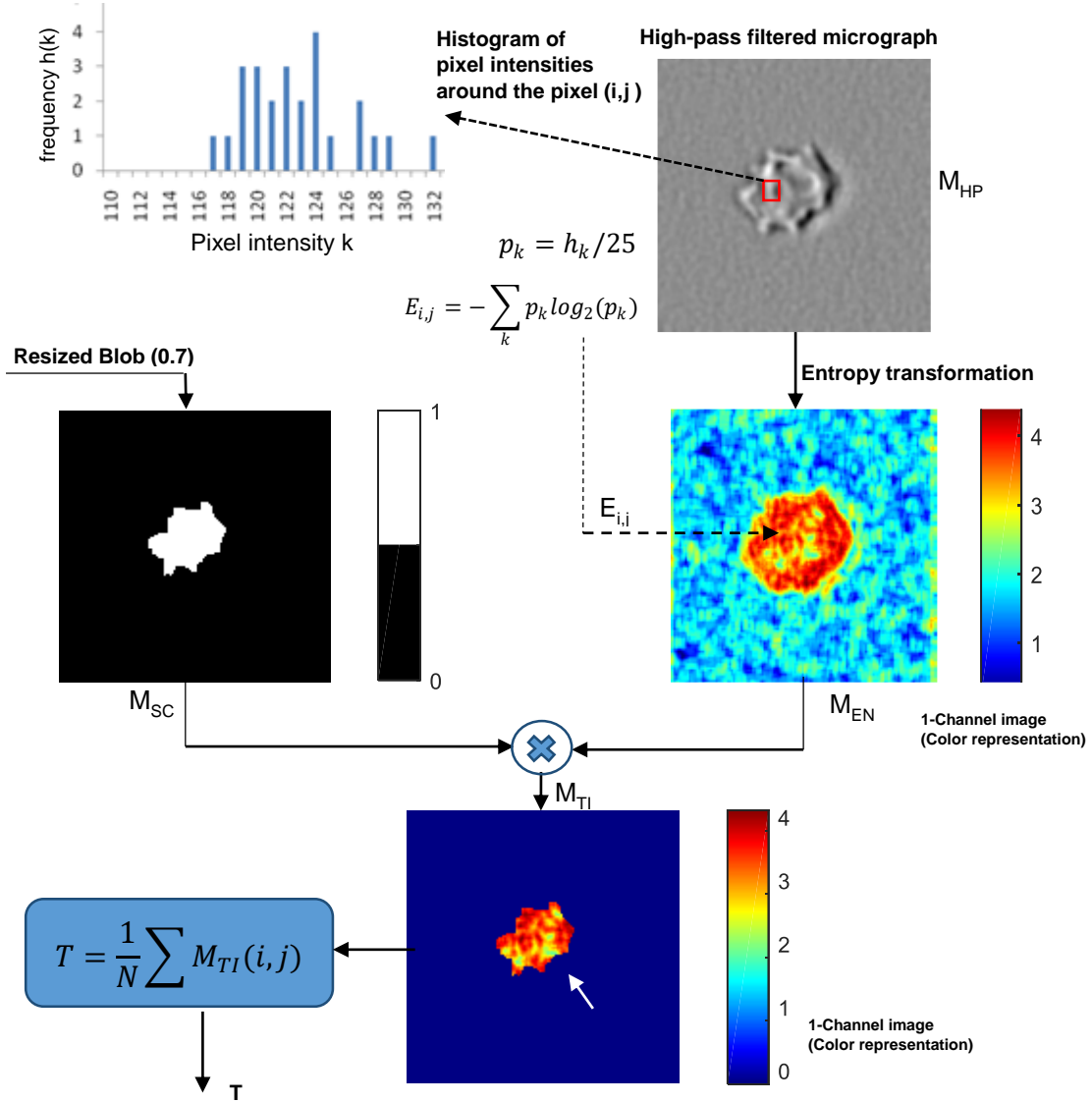


Fig. 38. Texture inhomogeneity calculation. Entropy transformation M_{EN} over the high-pass filtered cell micrograph M_{HP} based on the histogram of pixel intensities in local regions of 5 by 5 pixels. M_{EN} is multiplied with the binary mask M_{SC} that sets entropy values of non-inner cell pixels to zero. Non-zero values of the resulting image are averaged to obtain the RBC texture inhomogeneity (T).

After multiplication, all pixel values of M_{TI} are added together and divided by the number of pixels N forming the blob. The result is the average entropy T of the inner cell region that characterizes the inner texture of the cell. Entropy values of the outer cell region (background

and cell boundary) do not affect the addition because they have been previously set to zero by the binary multiplication. In comparison to smooth cells, bumpy cells have more brightness variation and therefore a higher value of entropy. In some cases, non-oriented discocytes can also present raised values of internal entropy due to the membrane folding. However, their values of border roughness and non-circularity allow their differentiation with respect to echinocytes.

In conclusion, the texture feature T measuring inhomogeneity is given by:

$$T = \frac{1}{N} \sum M_{TI}(i, j)$$

where M_{TI} is the matrix of entropy values of the inner cell region and N the number of points contained in this region.

3.6.2.4 Equivalent diameter

Erythrocytes undergo a slight diameter reduction during the morphological changes of the echinocytic pathway. This constitutes a good marker for the differentiation between spherocytes and non-oriented discocytes since both exhibit low roughness, low non-circularity and low texture values. The equivalent diameter ED corresponds to the diameter of an equivalent circle that contains the same area as that contained in the blob M_H , which represents the cell on the micrograph (Fig. 39). The area of the binary blob is expressed as number of pixels. The corresponding conversion in metric units must consider the pixel size of the camera sensor ($6.45\mu\text{m}$) and the magnification factor of the objective ($\times 40$) in order to calculate the real cell size. From this, the ED -feature derives as follows:

$$ED = 2 \sqrt{\frac{A}{\pi}} \left(\frac{6.45\mu\text{m}}{40} \right), \quad \text{where } A = \text{number of blob pixels}$$

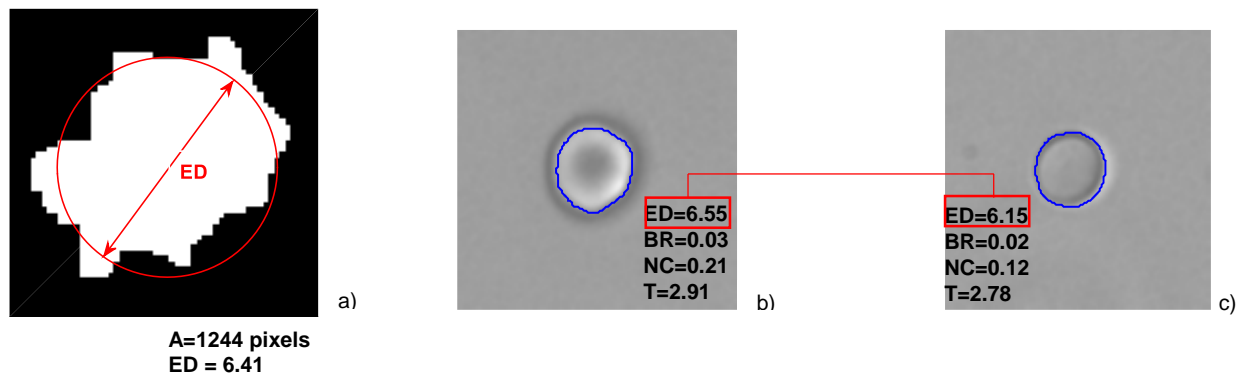


Fig. 39. a) Graphical representation of the equivalent diameter ED of an irregular form consisting of 1244 pixels. Real ED measure for b) a non-oriented discocyte and c) a spherocyte.

3.6.3 Classification

After the feature extraction, each RBC is parameterized by a vector of four coefficients that describes the morphology of the cell in terms of border roughness, non-circularity, texture inhomogeneity and size. RBC morphologies (D, E, and S) adopt specific values of these features and the classification process is based on the interval definition of these values. In order to establish the intervals, RBC micrographs were first manually classified into the three morphological categories and then analyzed by image processing. This calibration procedure was done by analyzing aliquots of RBCs during 12 weeks prior to the main monitoring of the storage lesion for this study. The images were used as reference of normal and aged RBCs for the algorithm calibration. One thousand micrographs for each RBC category were selected for the analysis. Through this process, three sets of feature vectors were obtained, each of them representing feature values of D, E and S.

The graphic representation of the feature vector allowed to observe the dispersion of values of each morphology. For this purpose, the features NC, BR and T are plotted in a three-dimensional feature space where each axis corresponds to a feature since stored RBCs are almost entirely characterized by these three features. The following figure shows the distribution of these values.

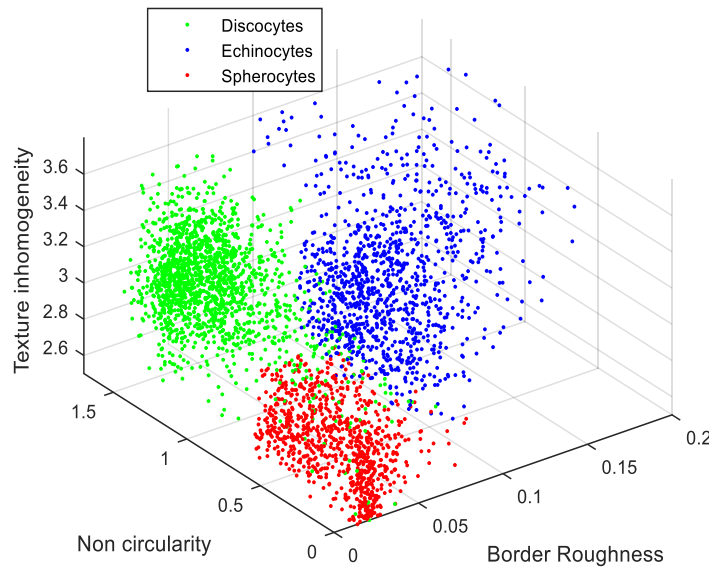


Fig. 40. Three-dimensional feature scatter of the three RBC morphological classes; discocytes (red), echinocytes (blue) and spherocytes (red). Each point corresponds to one cell analyzed by image processing. Axes represent the feature values; texture inhomogeneity, non- circularity and border roughness. (Size feature not shown)

Proximities in the feature space indicate RBC morphological similarities. In this sense, morphological differences between erythrocyte classes (D, E and S) must be reflected as spatial separations in the feature space. This is evident in the case of echinocytes and spherocytes (blue and red points respectively) which are located separately although there is no definite gap between them (Fig. 40). The adjacency of both clusters in the feature space is consistent with the gradual transition between both cell types manifested through the progressive contraction of spikes (decreasing texture inhomogeneity and border roughness) while preserving the spherical form (low non-circularity). However, discocytes are clearly separated from the other two classes because the oval profile captured during the orientation while in motion differs significantly from low values of non-circularity. This feature is therefore a preferred marker for discocyte identification. Non-oriented discocytes can be nevertheless seen as isolated points connecting the zones D-S. However the occurrence of these cases is significantly less frequent in comparison with orientated discocytes. Discocytes are predominantly located in the region of high non-circularity (vertical orientation), middle-high texture inhomogeneity and low border roughness (smooth texture). Echinocyte feature values of EI, EII and EIII are concentrated in the zone of middle-high texture inhomogeneity (bumps formation and loss), low-middle non-circularity (disc-spherical transition) and middle-high border roughness. As expected, spherocytes are distributed in low values of texture inhomogeneity, low border roughness and low non-circularity.

Two-dimensional projections of the data points show the intervals where the feature values are distributed. This allows the definition of threshold values for the classification of RBC types (Fig. 41). BR- values greater than 0.06 correspond uniquely to echinocytes and thereby the

first feature threshold T_{BR} can be set to this value to obtain the first set of echinocytes. Echinocytes with BR under 0.06 are mainly sphero-echinocytes with tiny spikes and are not distinguishable from spherocytes through this feature. At this point, BR seems to be enough to characterize directly almost all echinocytic forms corresponding to the subtypes EI, EII and E III. Excluding these points, a new two-dimensional perspective of the features, in this case observing BR versus NC, reveals a region where discocytes prevail and are separated from the other two types (Fig. 41). Non-circularity values greater than 0.69 are characteristic of oriented discocytes whose oval profile deviates significantly from the circular form. This makes it possible to set a second feature threshold T_{ED} in order to recognize discocytes after the previous recognition of echinocytes. Remaining discocytes (under this threshold value) are not oriented and therefore they show the known disc form (low non-circularity). However, the occurrence of these cases is statistically not significant. Discarding the above recognized oriented discocytes ($T_{ED} > 0.69$) a third two-dimensional feature view, representing T versus NC, shows the separation between spherocytes and sphero-echinocytes along the T-axis (Fig. 41). A plausible threshold value T_{IH} of the for texture inhomogeneity feature can be set to 3 in order to separate both spherocytic types. A few echinocyte points remain in the region of spherocytes due to tiny spikes on the cell membrane that are not more identifiable with respect to the sensitivity level of the feature extraction algorithm. Furthermore, some circular discocytes exhibiting high T-levels are located in the sphero-echinocytes region as result of high luminosity contrast through the inner biconcavity that increases the texture inhomogeneity. These cases can be disregarded due to their negligible occurrence level and taking into account that the main purpose of this study consists of a primary approach to the automatic quality evaluation of the stored RBCs.

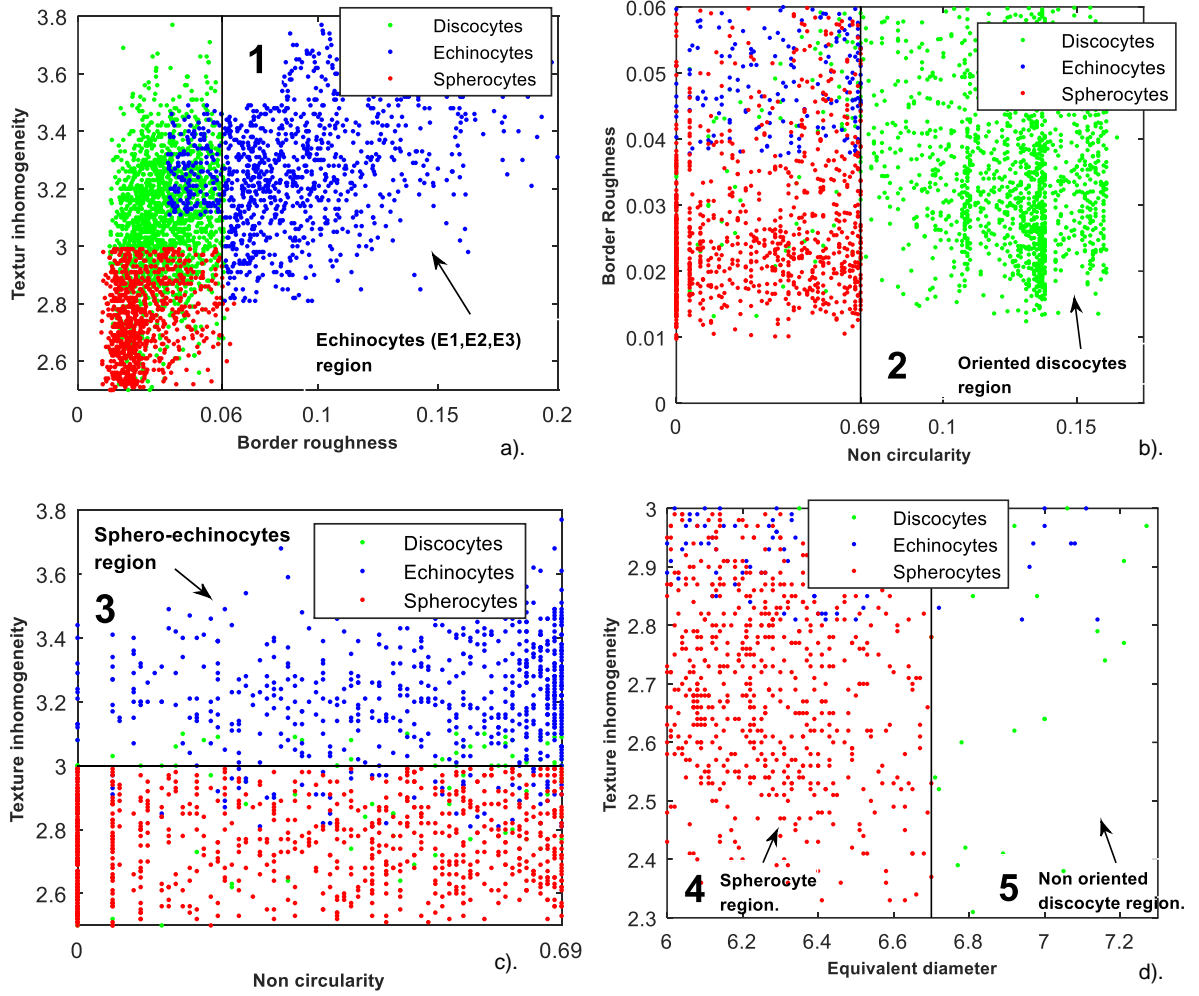


Fig. 41. Two-dimensional views of the four dimensional feature space. Points represent RBCs . a) Feature distribution BR vs. T. $BR > 0.06$ defines the region of echinocytes (E1,E2,E3). b) Feature distribution NC vs. BR. $NC > 0.69$ defines the region of oriented discocytes (D). c) Feature distribution NC vs. T. $T < 3$ (excluding D,E1,E2, and E3) defines the region of spherocytes and non-oriented discocytes . d) Feature distribution ED vs. T. $ED < 6.7$ separates spherocytes from discocytes.

Taking into account the flow and optical conditions for the cell imaging in this study, the area bounded by the oval profile of oriented discocytes is similar in value to the circular area of echinocytes and spherocytes and only the area of occasionally imaged circular (non-oriented) discocytes is larger. Considering this aspect, the size feature does not represent a crucial parameter for the differentiation of RBC morphological types in flow. However, it is a very meaningful parameter for the detection of cell overlapping, which is considered a noise factor in the image processing. Cell overlapping cases were previously excluded by means of the equivalent diameter and border roughness vales. Excluding the above identified sphero-echinocytes, a two-dimensional feature view of T versus ED over the remaining feature points allows the observation of the size separation between non-oriented discocytes and spherocytes (Fig. 42). According to this, the size threshold $T_{ED}=6.5$ separates both RBC types and contributes to the fine tuning of the spherocytes region. Only a small proportion of sphero-

echinocytes remain in the region of spherocytes in the range $2.8 < T < 3$. This sub-region constitutes a tolerance zone for the distinction between both RBC types caused by the gradual transition $E \rightarrow S$. Based on this analysis, four threshold values were defined: $T_{BR}=0.06$, $T_{NC}=0.69$, $T_{IH}=3$ and $T_{ED}=6.5$. The automatic classification consist in a decision tree which applies these threshold values for the sorting of the cells in the specific classes D, E and S.

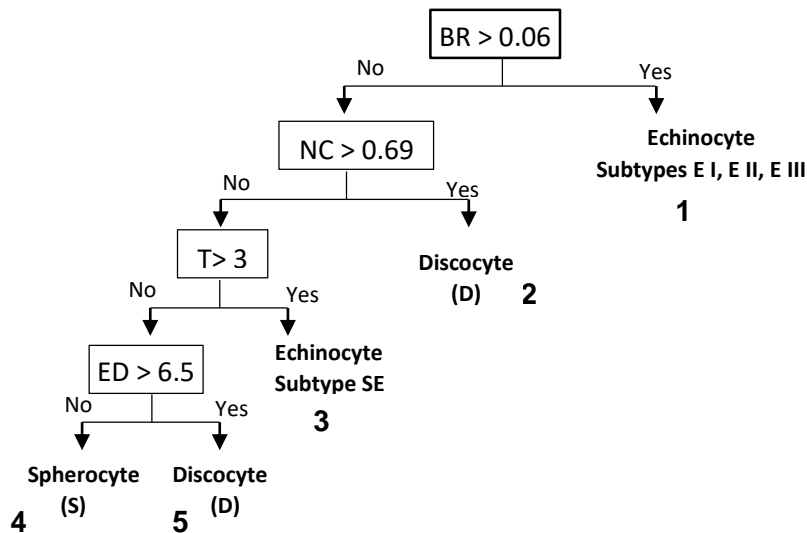


Fig. 42. Binary decision tree for classification of red blood cells. The first ramification detects erythrocytes with superficial bumps and spikes (echinocytes) through the border roughness (BR). Smooth oval contours (discocytes) and round erythrocytes with small spikes (sphero-echinocytes) are recognized by the non-circularity (NC) and texture inhomogeneity (T), respectively. In the last ramification, smooth spherical erythrocytes (spherocytes) are distinguished from non-oriented discocytes by the equivalent diameter (ED). Bold numbers refer to numbering in figure.41.

In a first classification step, the threshold level of the border roughness BR (measured by Fourier-descriptors) is applied. This identifies the echinocytes, which show appreciable spectral components corresponding to contour bumps.

In a second step, the cells without border bumps are separated into circular and non-circular (oval) cells by thresholding the measured non-circularity. The oval cells obtained from this algorithm step are classified as discocytes.

In the third step, the circular cell images are analyzed with respect to their texture-inhomogeneity. This way, some echinocytes are detected which were not found in step one due to the smallness of their contour bumps and spicules. If a cell exhibits texture inhomogeneity above a suitable threshold, then it is classified as an echinocyte. According to the classification scheme in (7), such cells would probably be described as sphero-echinocytes (SE).

In the last decision step, the left over circular cell images with homogeneous texture have to be discriminated with respect to the classes S and D. The D cells found in this set are not

identified in the second step because of their orientation: unlike the majority of the rolling discocytes, these cells have been oriented within the focal plane during the image capture. Cells with a size above the ED-threshold of 6.5µm are classified as discocytes, while the smaller ones are classified as spherocytes.

According to this decision tree, the feature vector of every RBC falls into one of the three categories D, E and S. The resulting relative proportions between them were used for the monitoring of morphological changes in the RBC units.

After the classification, the resulting frequency of each morphological stage is used to calculate the morphological index (MI) of the corresponding sample. The MI and the percentages of echinocytes and spherocytes in relation to the total number of analyzed cells are used as measures of the storage lesion in RBC units.

3.7 Monitoring of RBC Units

3.7.1 Percentage of Echinocytes, Spherocytes and morphological Index over Time.

For the determination of the storage lesion in each RBC unit, the proportions of discocytes (D), echinocytes (E) and spherocytes (S) are measured as functions of storage time. Based on these measurements, the morphological index MI is defined as the average score of the weighted morphological classes:

$$MI = \frac{1}{N} \sum_{i=1}^3 w_i \cdot n_i$$

where n_i is the number of occurrences of each morphological class and N is the total number of analyzed cells. For the three defined morphological RBC stages, weights (w_i) are assigned to each class: $D \rightarrow w_1 = 0$, $E \rightarrow w_2 = 2.5$ and $S \rightarrow w_3 = 5$. These values are chosen in accordance with [72]. According to this, each classified RBC contributes to the index in a manner proportional to its degree of damage (D, E or S) and occurrence.

Figure 43 shows typical damage curves measured in one individual RBC unit. At the beginning of storage, RBCs do not show significant changes in their morphology and therefore exhibit low percentages of E and S (<5%), with approximately 95% cells showing a normal smooth discoid shape. This corresponds to a low morphological index (< 0.4). After two weeks, the first bumps and spicules are detected on the membrane of some erythrocytes. At week 5, the proportion of echinocytes (type E) varies between 5% and 30% depending on the RBC unit, while the quantity of spherocytes remains below 10% because the transition $E \rightarrow S$ does not

occur frequently within the official shelf-life of RBC-units (35 days, [26]). Up to this time, the morphological index increases mainly due to the increasing concentration of E-type cells. However, the last morphological stage (S) of RBCs becomes more frequent at week 8, reaching levels between 5% and 20% depending on the unit. After approximately 8 weeks of storage, the maximum point of echinocyte frequency is reached and the proportion of echinocytes (E) stops increasing and usually starts to decay until the end of the observation time of 13 weeks, indicating that the morphological transition $E \rightarrow S$ becomes more frequent than the transition $D \rightarrow E$. After week 10, the rising proportion of spherocytes usually exceeds the percentages of echinocytes. From here, a coherent compensation effect is observed in the sense that any depletion in the percentage of echinocytes is always compensated through an equivalent increment in the proportion of spherocytes, being consistent with the direct transition $E \rightarrow S$. This fact is manifested in the slope symmetry between E and S-curves relative to the horizontal.

As is discussed in the following section, at the end of the monitoring period (week 13), a high donor-variability in the final S-percentages (25% - 65%) and morphological index (1.7 - 3.7) is observed (see figure 53). This indicates large differences between individual RBC-units with respect to their rate of deterioration.

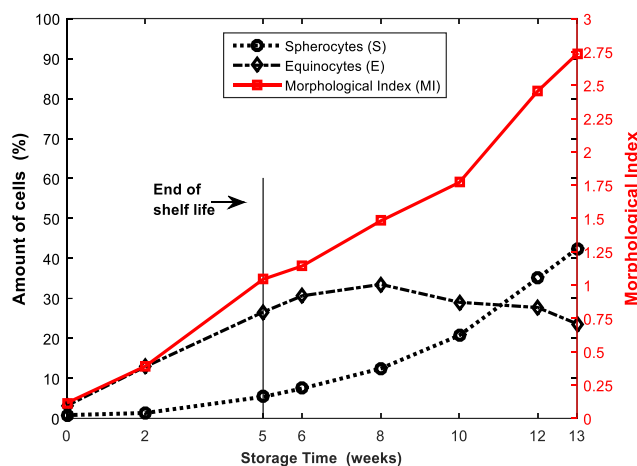


Fig. 43. Typical data of E-percentages (\diamond), S-percentages (\circ) and morphological index (MI) in an individual RBC unit as function of time. End of shelf life (35 days) as defined by [44]

Having established the system and an algorithm able to discriminate the different shapes erythrocytes undergo, monitoring of RBC units over time was performed in order to assess morphological changes and find correlations with biochemical parameters known to change during erythrocyte storage. The following sections describe the detailed analysis of RBC units from the three sets of donors (see also section 2.4/2.4.1).

3.7.2 Donor Group 1.

As indicated in section 2.4, 5 RBC units, corresponding to the first donor group, were followed over a storage period of 13 weeks. At time intervals of 1 to 3 weeks, samples were taken and assessed using microscopy and biochemical testing. As expected, the morphological assessment of this group shows an increase of echinocyte percentages (E-percentages) until week 10 for all RBC units (Fig. 44a). The fluctuations observed at earlier time points are attributed to inconsistencies in the setup which were optimized throughout the series of experiments. The focal plane height was not sufficiently well reproduced and the degree of orientation of discocytes in the rolling mode was not maximized. This could have an impact on the E-percentages due to flipping discocytes being misinterpreted as echinocytes by the classifier. A strict procedure for the reproduction of 12 μ m height for the focal plane was only established at week 10. Despite this additional source of statistical deviations in the E-percentage at the first measurement points up to week 10, there is evidence for the consistency of the results. Firstly, the least damaged RBC unit of this group (donor 1-1) continually shows a slower deterioration in comparison with the other RBC units of the group. This is reflected in the constantly low E-percentages of this unit over the time. The regularity of this fact for the whole monitoring period implies that the measurement errors are not significant, because of the low probability of a systematic error occurring for the same RBC unit for 13 weeks. After the tenth week, the E-percentage is still increasing for this unit without having reached the maximum point of E-percentages, confirming its delayed deterioration progress. In addition, lower S-percentages and low hemolysis values (Fig. 44b and 45b) confirms the tendency of this RBC unit to deteriorate more slowly. All five E and S-curves of this group show a certain intra-group order in the sense that they tend to exhibit always the same order in the deterioration degree of RBCs. E-curves rarely cross each other. The RBC samples were evaluated without keeping a specific sequence among them, thus excluding the possibility of time-dependent factors influencing the results during the routine of the sample analysis.

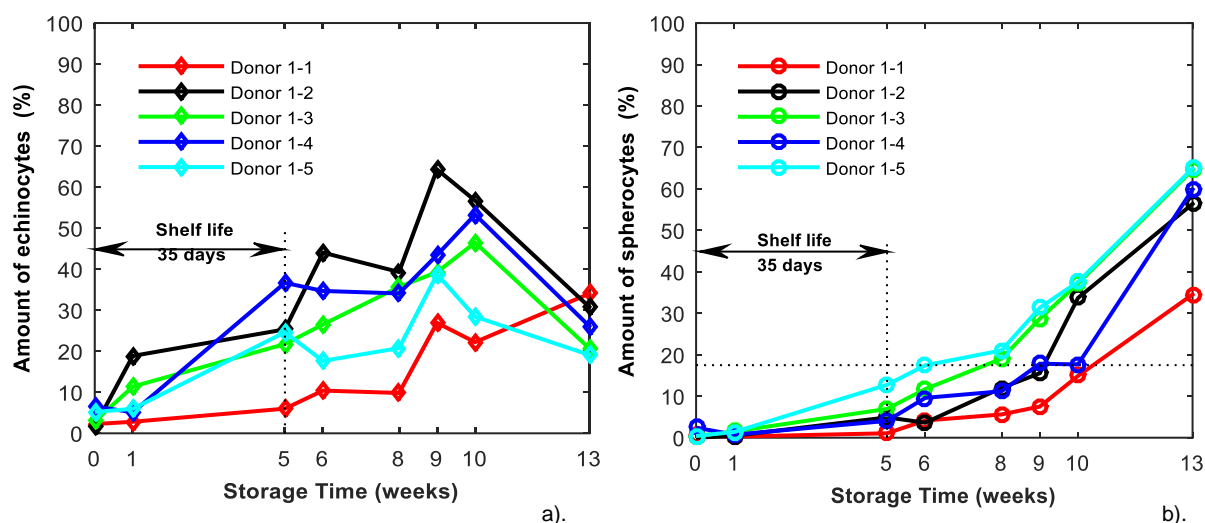


Fig. 44. Morphological changes on RBC units of the first set of donors. Curves represent **a)** E-percentages and **b)** S-percentages in individual RBC units as function of time.

E-percentages represent almost entirely echinocytic forms without being critically altered by deformed discocytes recognized as echinocytes. This is particularly demonstrated by the low E-percentages at the beginning of the monitoring (week 0), being consistent with the expected good quality of RBCs at the start of the storage. Beyond moderate statistical fluctuations, E-curves describe the deterioration progress in the RBC units of group 1 consistently.

As opposed to the E-percentage, S-percentages are not affected by false recognition of non-oriented discocytes. The symmetrical form of spherocytes and their non-deformability under different flow conditions enables the classification of this morphology type without ambiguities. S-percentages rise continuously until the end of the monitoring period. This is consistent with the fact that no decrease in S-percentages should occur because spherocytes do not undergo further morphological transformation before the tenth week and therefore their quantity is cumulative over the whole time. After week 10, a further morphological stage was sporadically observed ("ghost"), indicative of the membrane remnants after the cell contents have been released during lysis. However, it does not represent a relevant aspect to be studied because it takes place towards the end of the monitoring period and does not have any impact over the statistical analysis. The formation of spherocytes becomes evident from the fifth week on, just when the shelf life of RBC units expires. The S-percentage still remains under 15% at this week. Before this time, spherocytes are rarely detected. Between the weeks 9 and 10, the rate of spherocyte formation increases significantly. This is congruent with the maximum point of E-curves confirming the transition $E \rightarrow S$.

The morphological index curves (MI-curves) show very similar deterioration rates amongst four donors with a distinctive separation of the MI-curve corresponding to the above mentioned donor 1-1 (Fig. 45a). This evidences the better preservation of this RBC unit once again. This MI-curve indicates a deterioration which is delayed by approximately four weeks in comparison to the other units. MI-curves rise continuously and do not exhibit oscillations as in the case of E-curves. The morphological index, as weighted average between echinocytes (weight 2.5) and spherocytes (weight 5) relative to the total amount of analyzed RBCs in the sample, preponderates the measured amount of spherocytes through the higher assigned weight. It thus attenuates the oscillation of E-percentages in the MI calculation. This fact also explains the predominance of S-percentages reflected in the MI after the tenth week, when E-percentages decrease. As in the case of S-percentages, the morphological index of this group becomes more evident from the fifth week on, when values of up to 1.25 are reached.

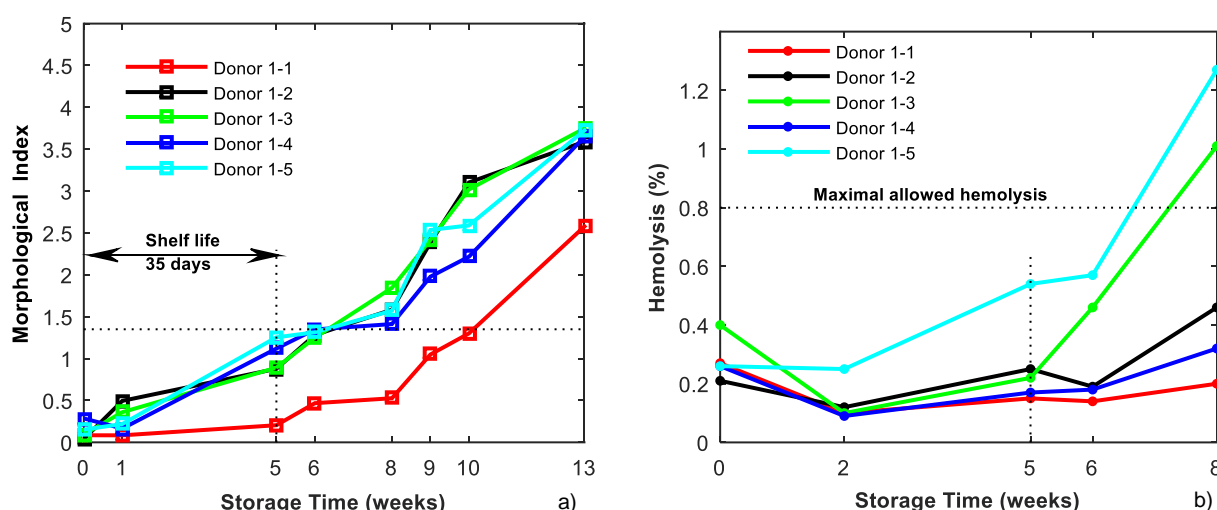


Fig. 45. a) Morphological changes on RBC units of the first set of donors measured as morphological index (0: Discocytes, 2.5: Echinocytes and 5: Spherocytes). **b)** Respective hemolysis percentages for the same units. Each curve represents an individual RBC unit as function of time.

In group 1, the morphological assessment was done during thirteen weeks. However, the reference values of hemolysis were measured only until the eighth week (Fig. 45b). Except for the donor 1-5, hemolysis values decrease between the beginning of the storage and the second week, which is irregular for stored RBCs: hemolysis values are expected to increase monotonously with time. Supported by the fact that the hemolysis decrease occurred in four out of five units, a systematic error at the day of the initial measurement can be hypothesized. Subsequent hemolysis measurements follow the expected pattern, and do not appear to be compromised.

Many facts are notable in the hemolysis curves of this group. First, hemolysis of the donor 1-5 is distinguished by the highest hemolysis percentage (h) from the second week ($h=0.25\%$) until the eighth week ($H=1.27\%$). This coincides with the RBC unit with the highest S-percentages over the time. Hemolysis percentages of the other donors do not show significant differentiation until the fifth week. They range between 0.15% and 0.25% at this point of time which indicates little variation between units, if the tolerance in the hemolysis measure is taken into account. However, the sixth week reveals a clear tendency of deterioration. Two RBC units (donors 1-3 and 1-5) have deteriorated faster than the remaining three units. Out of these three units, the unit with consistently lower hemolysis percentages corresponds to the unit with lower E and S-percentages (donor 1-1). Interestingly, the order of hemolysis curves (H-curves) agrees with the order of S-curves (after the end of the shelf life). This is the first indication of a certain degree of intra-group correlation between hemolysis percentages and S-percentages. Apart from the donor 1-1, the order of E-curves does not coincide with the order of S-curves and consequently with the order of H-curves. The absence of intra-group order correlation with E-curves does not make possible to use the proportion of echinocytes in order to estimate the deterioration degree of RBC units as measured by hemolysis. In addition, the non-monotonic behavior of E-curves compared with the monotonically increasing S and H-curves indicates a lack of correlation between E and S or H measurements.

At the end of the shelf life, no RBC unit exceeded the maximal allowed hemolysis value of 0.8% (H-threshold). Only in the eighth week is the H-threshold exceeded by two deteriorated RBC units (1-3 and 1-5). S-curves corresponding to these two units also show the highest S-percentage level at this week. Considering this co-occurrence, the definition of an equivalent threshold of spherocyte percentages (S-threshold) can be envisaged in order to estimate the quality of RBC-units with respect to the hemolysis threshold (H-threshold). The validity of a possible S-threshold is further investigated through the assessment of the other two donor groups.

Except for the curve representing the donor 1-1, MI-curves crossed each other and do not show an evident order correlating with the order of H-curves. Only the best preserved RBC unit seems to show a consistent pattern in all measurements. The MI-curves constitute a less useful indicator of hemolysis percentages than the S-curves because the MI-curves are an average of the E and S percentages, and the E curves do not directly reflect the deterioration progress of RBC units. Despite this, the morphological index is sensitive to morphological changes during the shelf life. All in all, MI-data provide an acceptable description of the deterioration progress in that they increase monotonously over time. The setting of a maximal morphological index (MI-threshold) as an acceptable measure for the quality estimation of RBC units will be discussed further down.

Finally, the measured ATP values also support the validity of the morphological data to a large extent (Fig. 46.). Once again, the two units with lowest ATP levels also exhibit the highest hemolysis and S-percentages (donors 1-3 and 1-5). The best preserved RBC unit (1-1) does not always show the highest ATP level over time but it does alternate the highest ATP level with one other RBC unit (donor 1-2).

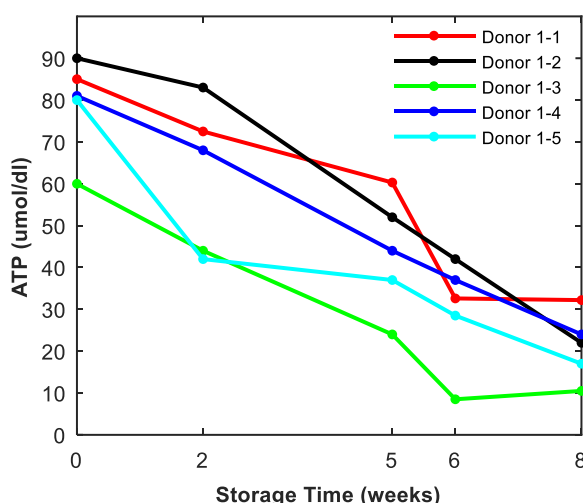


Fig. 46. ATP values of RBC units of the first donor group. Each curve represents individual RBC units as function of time. The two lower ATP-curves are in concordance with the two higher curves of S-percentages and hemolysis.

Additional biochemical measurements exhibited too much variability to enable meaningful correlations with morphological and hemolytic data (therefore methods not explained in detail; data shown in appendix Tab. A-1 to Tab. A-17).

3.7.3 Donor Group 2

The second set of RBC units consists of seven donors. The monitoring period for both morphological and biochemical assessments was thirteen weeks. Sample preparation, measurement protocol and system setup were the same as for the first set of donors. For this group, the focal plane height was precisely adjusted to a fixed level (12 μ m from channel bottom) as explained in chapter 3.4.

In comparison with the group 1, E-curves of this set of RBC units exhibit lower E-percentages and a flat response to the storage deterioration (Fig. 47a). At the beginning of the monitoring, E-percentages of the 7 samples ranged between 2.7% - 9.7%. In the second week, these values increase slightly (between 4.6% and 19%). This level remains almost constant until the tenth week, the data oscillating between 8.4% and 25 %. At the end of the shelf life (week 5),

E-percentages reach values between 8% and 21%, almost the same as to the values in the second week. By the twelfth week, four of the seven E-curves reach the maximum at which E-percentages start to decrease. At this point of time, the minimal and maximal E-percentage of the group are 17.5% and 29.5% respectively. In addition, E-percentages do not oscillate as much as in the case of group 1.

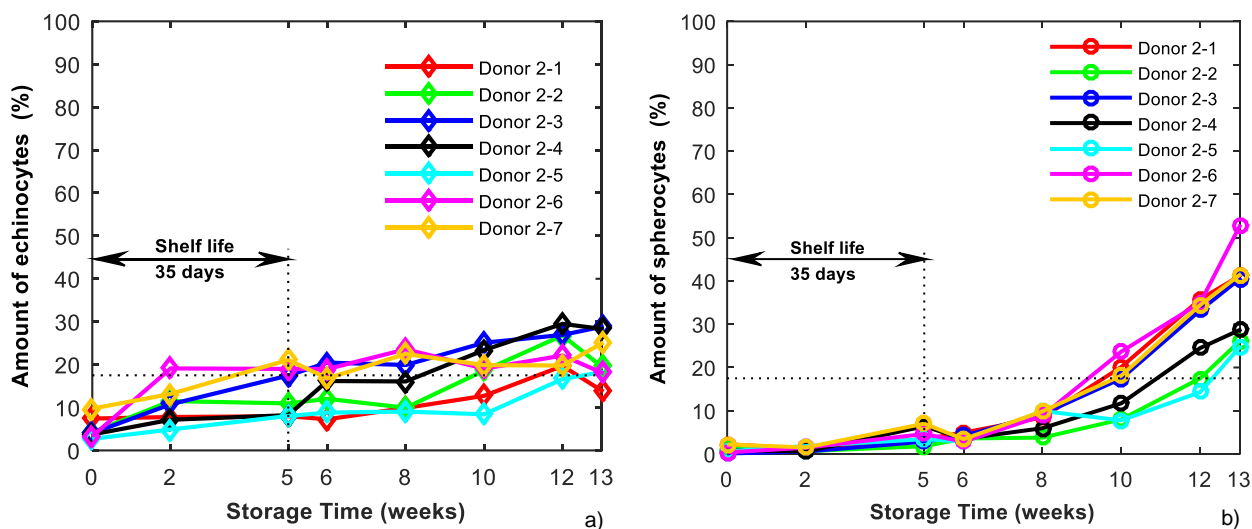


Fig. 47. Morphological changes on RBC units of the second set of donors. Curves represent **a)** E-percentages and **b)** S-percentages in individual RBC units as function of time.

Not unexpectedly, the S-percentages also indicate a slower deterioration rate in this group. Until the sixth week, they remain below 5%. Only after this point do the S-curves progress exponentially, reaching values between 24% and 52% in the week 13 (Fig. 47b). In comparison with S-percentages, the MI-values reflect the storage damage from the beginning of the storage in a more sensitive way because of the contribution of echinocytes (Fig. 48a). From the second week onwards, the order of the curves suggests the deterioration tendency of each unit. This tendency is maintained consistently until the end of the monitoring. MI-values of donor 2-2 and 2-5 are the lowest during the whole monitoring, indicating a better RBC preservation under storage conditions in this units. By contrast, donors 2-6 and 2-7 exhibit the fastest deterioration. RBC deterioration of donor 2-4 is always intermediate with respect to the rest of units of the group. The order of MI- curves is quite well reproduced by the order between S-percentages (after week 6), hemolysis percentages (Fig. 48b) and ATP levels (Fig. 49). However, this intra-group order is not reproduced by the E-percentages after the end of the shelf life.

During the shelf life, the state of deterioration of each unit cannot be inferred by the intra-group order of hemolysis percentages because the small percentages during this period ($H_{\min}=0.13\%$ and $H_{\max}=0.18\%$ at the end of the shelf life) suffer statistic deviation due to small variations in

the sample preparation. Analogously, S-percentages fluctuate in a small range between 1.7% and 7% at the end of the shelf life. At such low S-percentages, the accuracy of the measurement is reduced by the counting statistic of the image processing algorithm. For that reason, the intra-group correlation between S-percentages and hemolysis is only meaningful after the end of the shelf life of RBC units, when the measurement values are larger and more disperse. MI calculation is dependent on E and S-percentages with a heavier weighting on the contribution of the S-percentage, and therefore, after the end of the shelf life, the MI values exhibit largely the same pattern as the S-curves, when the S-percentages increase significantly. For that reason, the intra-group order correlates well with hemolysis data.

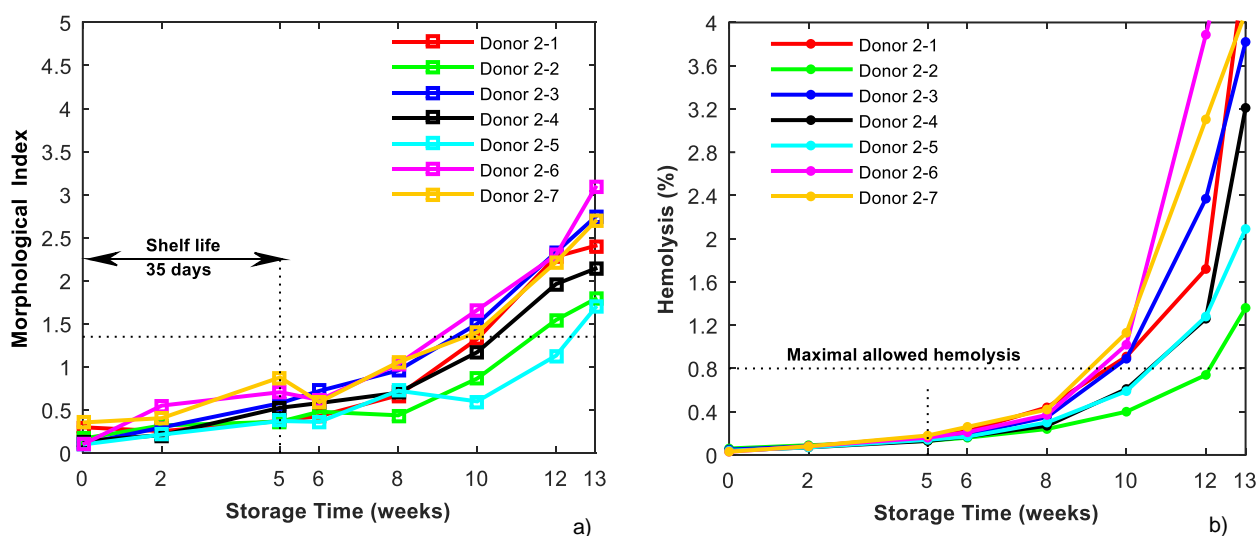


Fig. 48. Morphological changes measured in the RBC units of donor group 2. Curves represent **a)** Morphological index (MI) and **b)** Hemolysis percentages. Each curve represents an individual RBC unit as function of time. Shelf life corresponds to 5 weeks. Maximal allowed hemolysis during the shelf life is 0.8%.

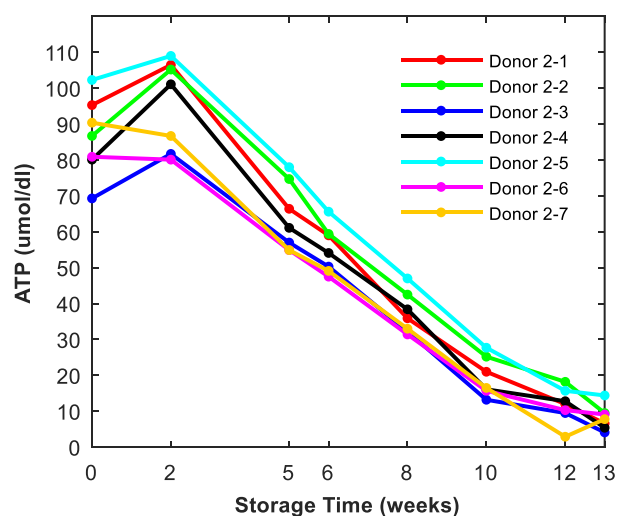


Fig. 49. ATP values of RBC units corresponding to the donor group 2. Each curve represents individual RBC units as function of time. ATP intra-group order correlates largely with the order of S-curves and hemolysis curves.

Interestingly, the intra-group order of ATP-curves is also in concordance with the MI-order. The RBC units with the lowest, intermediate and more advanced morphological deterioration correspond to the units with the upper, middle and lower ATP-curves respectively.

In general, group 2 exhibits a slower deterioration rate compared with the group 1. This is manifested through the biochemical data and through lower values of the morphological index.

3.7.4 Donor Group 3

Group 3 consists of five RBC units. One unit (from donor 3-1) was irradiated at the beginning of the storage in order to explore induced damage of RBCs. As usual, the E-curves rise during shelf life (Fig. 50a). However, they reach the maximum earlier than in the two previous groups (between week 5 and 8). E-percentages in the different samples range between 17.8% and 28.4% at the end of the shelf life and the maximal variation occurs in the following week, when they vary between 16% and 34%. After this point, E-percentages follow steady trends and finish with values between 14% and 24% at week 13. In almost all measurements, the irradiated unit shows an accelerated deterioration. In the case of E-percentages, its E-curve rises rapidly over the other curves until the second week and then it starts to decrease early, at the fifth week.

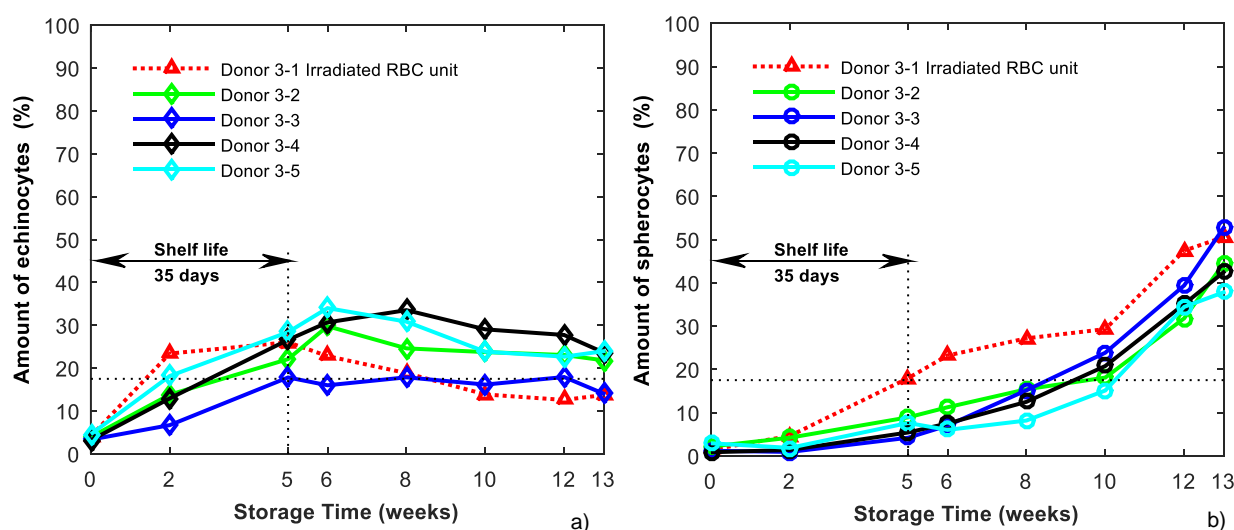


Fig. 50. Morphological changes in RBC units of the second set of donors. Curves represent a) E-percentages and b) S-percentages in individual RBC units as function of time.

In comparison to the other groups, the S-curves in group 3 reveal a faster deterioration of RBCs (Fig. 50b). The non-irradiated RBC units show a similar progress of S-curves. Donor 3-5 exhibits the lowest proportion of spherocytes after the sixth week, in agreement with the lowest hemolysis of this group showed by the same donor. At the other extreme, the irradiated

RBC unit shows the highest proportion of spherocytes over the whole time period. This correlates well with the highest intra-group hemolysis and partially with the lowest ATP level after the fifth week. Atypically, hemolysis of the irradiated unit exceeds the established limit under storage (0.8%) before the end of regular shelf life (Fig. 51b). This indicates that irradiated RBC units undergo early hemolytic alterations that are also expressed at a morphological level and can be detected through the rapid increase of the S-signal. In addition, the fact that E-percentages of the irradiated unit increase rapidly and then decrease early suggests that the transition of the E forms to the S form is more rapid than in the case of non-irradiated units.

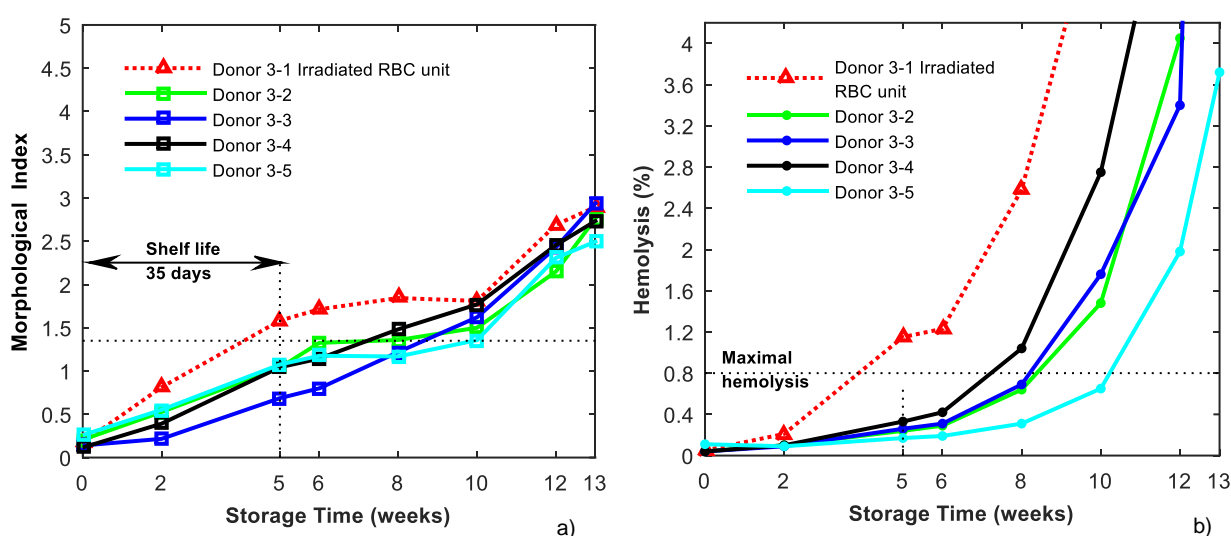


Fig. 51. Morphological changes in RBC units of the third set of donors. Curves represent **a)** Morphological index MI and **b)** Hemolysis in individual RBC units as function of time.

As to be expected, the top MI-curve corresponds to the irradiated RBC unit (Fig. 51a). Due to the similarity of the MI and S-curves, an interpretation about an intra-group order and hence the relative deterioration rates of the units is not possible.

However, hemolysis values show a clear and stable intragroup order and the best preserved RBC unit also exhibit the lowest S-values. In the case of non-irradiated RBC units, the hemolysis limit is only exceeded after the eighth week (Fig. 51b)

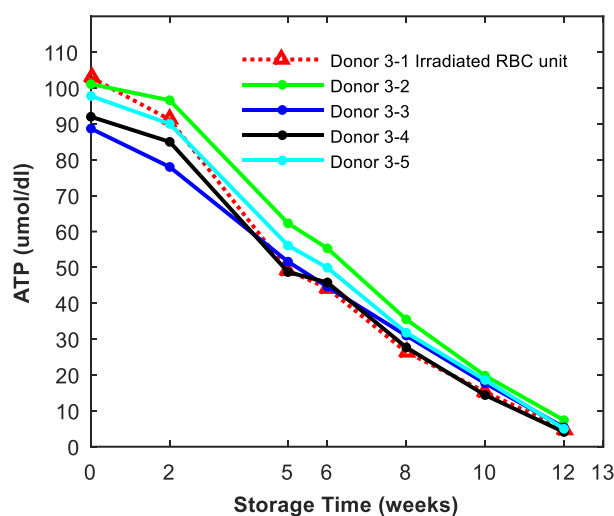


Fig. 52. ATP values of RBC units corresponding to the third donor group. Each curve represents individual RBC units as function of time. The irradiated unit does not show a significant differences from the other units in ATP levels.

Interestingly, the ATP data do not reflect the irradiation damage. This means the radiation process does not seem to influence the ATP levels (Fig. 52).

Considering E and S-curves of the three donor groups, the low S-percentages during the shelf life (until week 5) indicate that the morphological transition from echinocytes to spherocytes requires several weeks, although this time seems to be highly variable. Accordingly, the proportion of spherocytes cannot be predicted from E-percentages and depends on the variable residence time of RBCs in stage E. The high variability of residence time in this stage can be observed by comparing E and S-curves of the first two donor groups.

3.7.5 Inter-Group Correlation between Morphological and biochemical Assessments

Figure 53 displays the differences between the donor groups by superimposing their corresponding curves. The deterioration of the three groups of units over time is compared for the curves corresponding to MI, ATP, S, and hemolysis values (Fig. 53). Each group is represented with a different color and line trace as indicated in the upper legend of the figures. The curve of the irradiated RBC unit is represented with an additional color (green) in order to distinguish it from the non-irradiated units of the same group.

Figure 53a shows the morphological index MI obtained from the three sets of RBC units. Monotonously rising curves with increasing slopes after a storage time of approximately 8 weeks can be observed in all three groups. The characteristic decrease in ATP levels is shown

in Figure 53b. Figure 53c displays the S-percentages of all three sample groups over time. The overall trend is similar to the MI curves: monotonous functions with increasing slopes, in particular after the first 8 weeks of storage. This behaviour is in contrast to the E-percentage which peaks at different time points and decreases afterwards as mentioned in the section 3.7.1 (Fig. 43). Hemolysis curves of all units increase exponentially and show that the hemolysis values tend to be below the established limit of 0.8% before the eighth week of storage (Fig. 53d). Likewise, S-percentages and MI values are rarely higher than 18% and 1.4 respectively before this week. This analogy suggests an existing link between the hemolysis limit and a hypothetical morphological index limit which will be analyzed in the next section.

In general, group 1 deteriorates faster than group 2. It is important to note that these differences occur consistently in both morphological and biochemical data. Group 3 exhibits an intermediate deterioration in the sense that its measured values are consistently between the value range exhibited by the group 1 and 2 in all four measurements: MI, E, S and hemolysis. The agreement between morphological and biochemical assessments proves that the observed inter-group differences are not experimental artefacts.

No causes were found to explain such inter-group differences in the deterioration rate. Donor characteristics do not appear to be responsible for these differences since each group was comprised of donors with mixed gender, age and blood type. It is possible that seasonal influences are responsible for the quality differences observed.

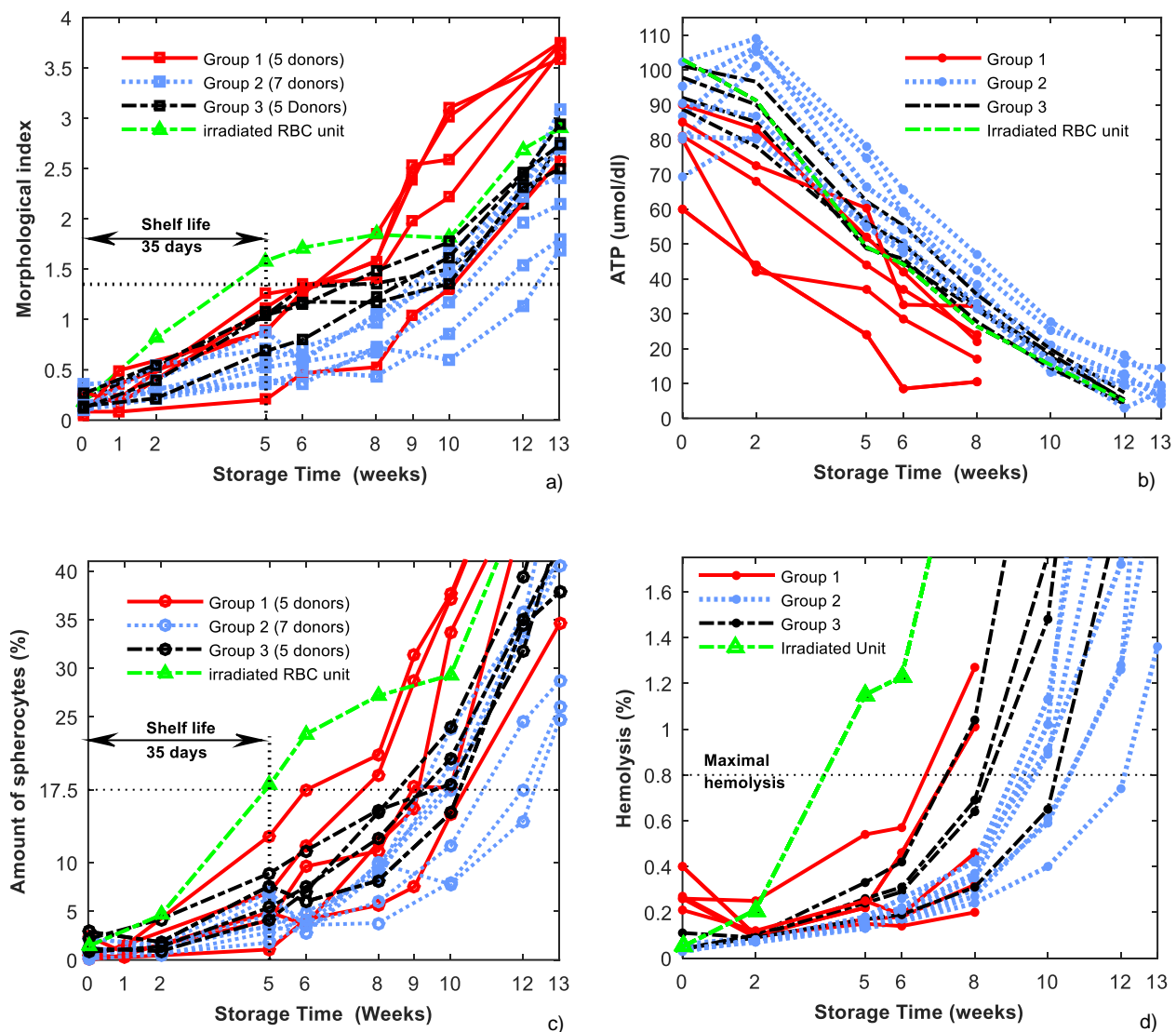


Fig. 53. Comparison of flow morphometry data and biochemical data in three sets of RBC-units during observation periods of 13 weeks. **a)** Morphological index. **b)** ATP-levels. **c)** Percentages of spherocytes. **d)** Hemolysis percentages. Graphs c) and d) are expanded for clarity in figures A-5 and A-6 in appendix.

3.7.6 Estimation of Hemolysis through morphometric Assessment

The monotonic increase of both S percentages and hemolysis as functions of the storage time indicates a correlation between both data sets. Figure 54 shows a scatter plot representing as points the S percentages and hemolysis values of each analyzed sample. This set of points contains the data of all three donor groups (differentiated by colors) during the whole monitoring period. Data points of the irradiated RBC unit are distinguished by the marker Δ .

The point distribution indicates a good correlation between both parameters. Temporal information about the elapsed storage time is not explicit in the graph but it can be inferred from the point's distance to the origin. Points near the origin correspond to samples of RBC units analyzed at the beginning of the storage. In general, samples assessed before the eighth week are represented by points below the hemolysis threshold ($<0.8\%$), where the distribution of points indicates a linear correlation (Fig. 54a). After this time, the relation between S percentages and hemolysis becomes nonlinear and the point distribution becomes more dispersed.

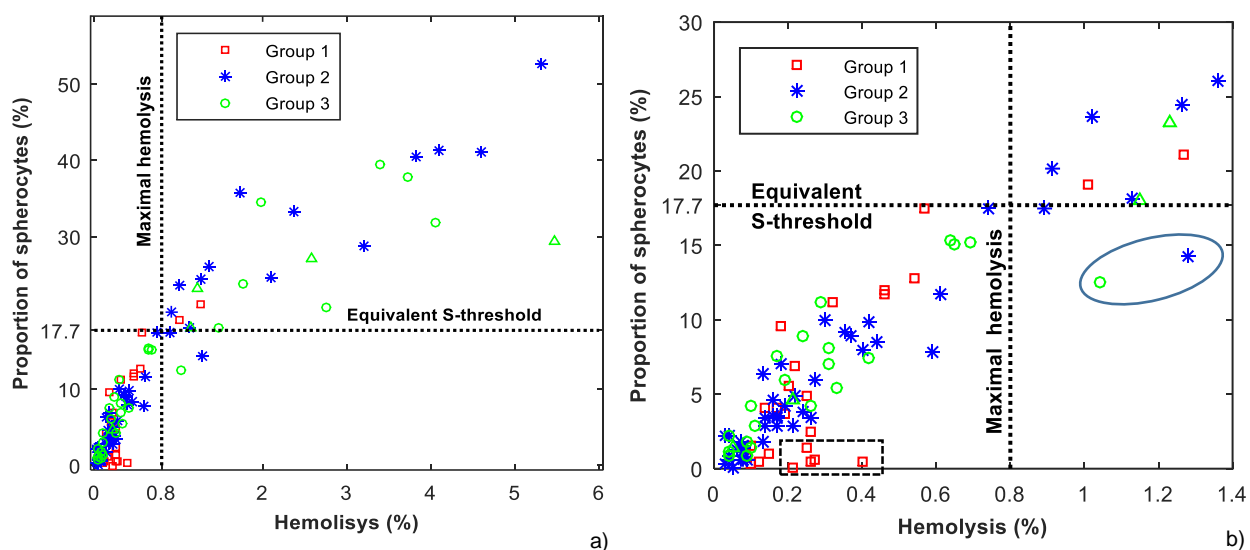


Fig. 54. Correlation between hemolysis and S-percentages for RBC units of all three donor groups. a) Overall view of all measurement points of hemolysis and S-percentages up to week 13. The S-threshold (17.7%) is optimized to agree with positive and negative cases of exceeded hemolysis limit (0.8%). Hemolysis threshold and the equivalent S threshold are indicated as dashed lines. **b)** Expanded view in the range of linear correlation. Only two data points out of 116 ($P < 0.03$) do not agree with the thresholding correspondence (enclosed data points). Unreliable hemolysis measurement values of the group 1 at the beginning of the storage (as mentioned before) are shown (see bottom boxed area).

The dashed vertical line separates the data points into two sets: below and above the maximal allowed hemolysis limit (0.8%). In the same way, the setting of an equivalent threshold of S-percentages (S-threshold) provides a similar separation of the data points in two sets. An S-threshold of 17.7% (horizontal dashed line) optimizes the concordance of point separation with respect to the 0.8% hemolysis threshold. This means that data points exceeding the S-threshold also exceed the hemolysis limit. From a total of 116 data points, only two data points do not conform this correspondence. Accordingly, 98.3% of the samples agree with it.

A Pearson correlation coefficient was calculated for the first eight weeks of storage, since in this time there is an approximately linear relationship between hemolysis and S percentages (Fig. 55). In addition, RBC units rarely exceed the hemolysis threshold of 0.8% during this period of time. For the relationship between S-percentage and hemolysis, a Pearson coefficient of $R = 0.85$ was obtained. This supports the presumption that the S-percentage is indeed a meaningful measure of the storage lesion.

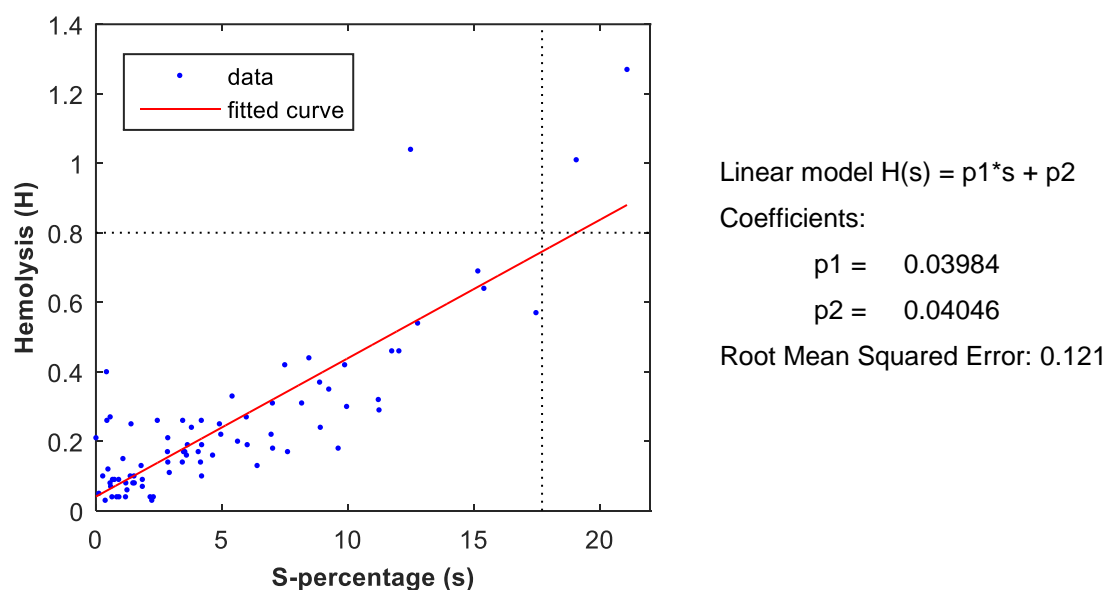


Fig. 55. Linear regression of hemolysis values and S-percentages based on 80 data points. Points represent measurements of all RBC units until the week 8. The center line (red) represents the theoretical linear model for hemolysis estimation as a function of S-percentages. Coefficients of the linear equations of the curves are shown (right side).

Additionally, the linear regression of hemolysis and S-percentage data points provides a theoretical linear model for the estimation of hemolysis values as function of the measured S-percentages (Fig. 55). The red curve represents the model that minimizes the standard deviation between measured and estimated hemolysis values. This deviation, called root mean square error, is 0.121 for this point distribution. This means that if a hemolysis value is estimated by using the S-value and the linear model, then the standard deviation of the hemolysis estimation is approximately 0.12%.

Considering the fact that hemolysis values are far below the hemolysis limit of 0.8% during the shelf life, S-percentages seem to provide a reasonable hemolysis estimation for diagnosing RBC quality.

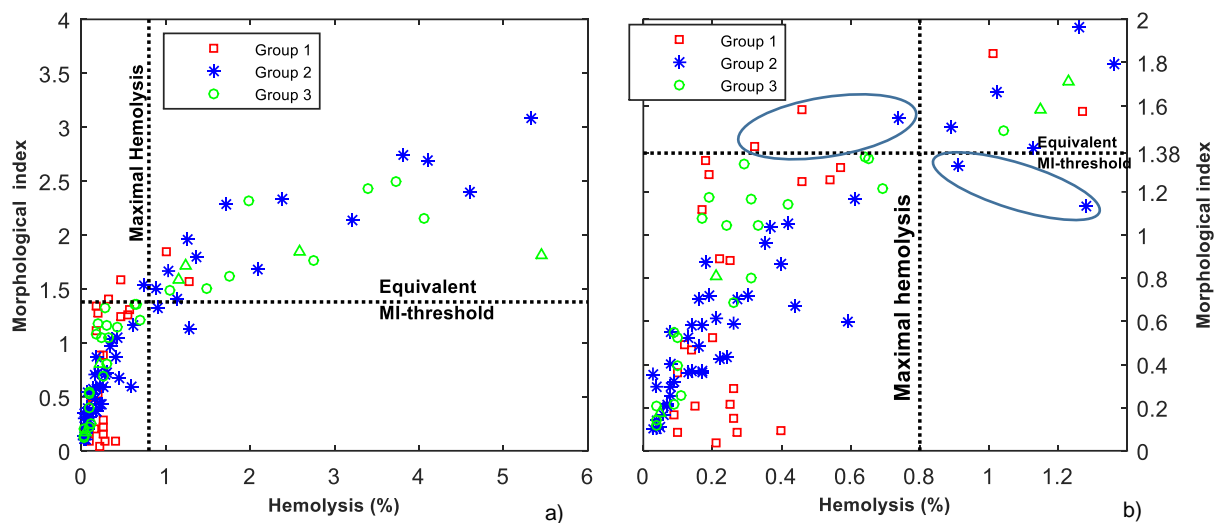


Fig. 56. Correlation between hemolysis and MI for RBC units of all three donor groups. **a)** Overall view of all measurement points of hemolysis and MI up to the week 13. The MI is optimized to agree with positive and negative cases of exceeded hemolysis limit (0.8%). Hemolysis threshold and the equivalent MI are indicated as dashed lines. **b)** Detailed view in the range of linear correlation. Only five of 116 data points ($P=0.05$) do not show the thresholding correspondence (enclosed data points). Unreliable hemolysis measurement values of the group 1 at the beginning of the storage (as mentioned before) are shown (see bottom boxed area).

MI values are also correlated with hemolysis values (Fig. 56a). As in the case of S-percentages, the data points correspond to the measurements of all RBC units over the whole monitoring period. The correlation seems approximately linear in the region below the hemolysis limit ($<0.8\%$) (Fig. 56b). The Pearson correlation coefficient is $R=0.76$ for data points within the first 8 weeks of storage. This value is a measure of the noticeably higher dispersion of data points as compared to the data of S-percentages. Similarly, an equivalent optimized threshold for MI values (MI-threshold = 1.38) generates an analogous estimation of exceeded hemolysis ($>0.8\%$), albeit with a somewhat lesser agreement: there are 3 false positive cases and 2 false negative cases within a total of 116 data points. This slightly lesser estimation performance is consistent with the weaker correlation which is largely due to the E-percentage which does not correlate with the measured hemolysis as shown in figure 57.

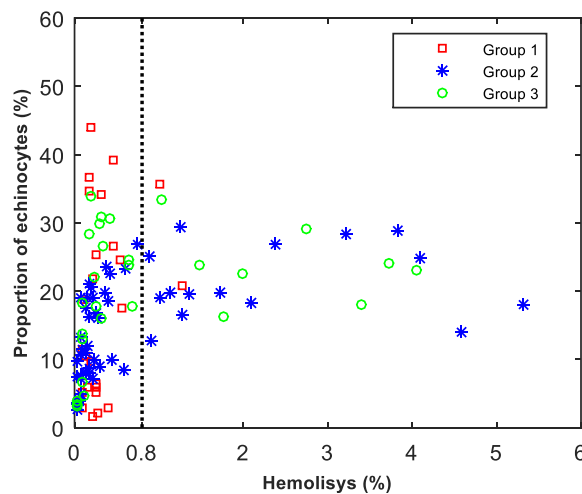


Fig. 57. Data Points of hemolysis and E-percentages of all RBC units during the monitoring. No correlation is observed between both measurements. Intermediate E-percentages at exceeded hemolysis values ($>0.8\%$) are consistent with the non-monotonous progress of the E-signal over the storage time. E-percentages over 30% exhibiting low hemolysis values ($<0.8\%$) also indicate the unrelated character of both parameters.

ATP levels decrease monotonously over the storage time. This correlates inversely with the increasing hemolysis values as shown in the scatter plot in the figure 58a. The data points represent the values of ATP and hemolysis measurements of all RBC units during the whole monitoring. The chronology of the measurements can be observed through the colors. Hemolysis limit (0.8%) is normally exceeded between the week 8 and 10 except for two points of the irradiated RBC unit at week 5 and 6 (see also green curve in figure 53d). As in the case of the S-threshold, an equivalent ATP-threshold at $20\mu\text{mol/dl}$ can be used to estimate whether the sample exceeds 0.8% hemolysis. However, the correlation is slightly lower than for the estimation by the S-percentages or the morphological index (see above) considering the larger amount of points that do not conform the threshold correspondence in this case.

As expected, ATP levels and S-percentages are also correlated since the spherocytosis turns out to be linked to the hemolysis according to the results. The data point distribution in figure 58b shows this correlation. Consequently, the defined ATP-threshold of $20\mu\text{mol/dl}$ is equivalent to the previously optimized S-threshold of 17.7% for hemolysis. (S-threshold of 18% is shown in the figure as better threshold optimization with respect to ATP levels).

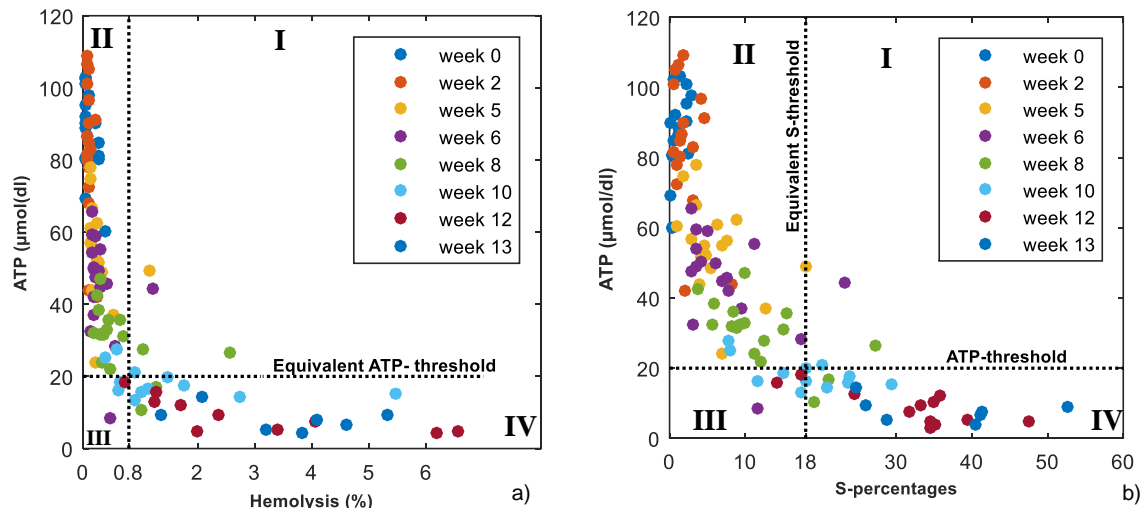


Fig. 58. Correlation of ATP levels with a) hemolysis and b) S-percentages during the whole monitoring. Each point corresponds to the measurement in one individual RBC unit at specific time points (see colors as time reference). Regions of threshold equivalence are located in the quadrant II and IV. Excluding the data points of the irradiated unit, only 7 of 108 data points do not exhibit the correspondence between the ATP and hemolysis thresholding (see quadrants I and III).

3.7.7 Morphological Response of RBCs to Heat Damage

Figure 59a shows the comparison between the heated RBC unit (dashed curve) and RBC units of the group 2 for S-percentages and hemolysis values over time. The heat damage was induced in the second week of storage and therefore two measurements (pre and post-heating) were carried out in this week. This double measurement corresponds to the step of the S and H-curve at this week. Post-heating values of this unit in the second week are comparable with deterioration levels of non-damaged RBC units after week 8 of storage. After the heat damage, the proportion of spherocytes and hemolysis significantly increase with respect to the non-damaged RBC units of the group 2 and remains significantly different until the end of the monitoring. Examples of cell micrographs of the induced spherocytosis by heating are shown in the appendix section (Fig. A-8)

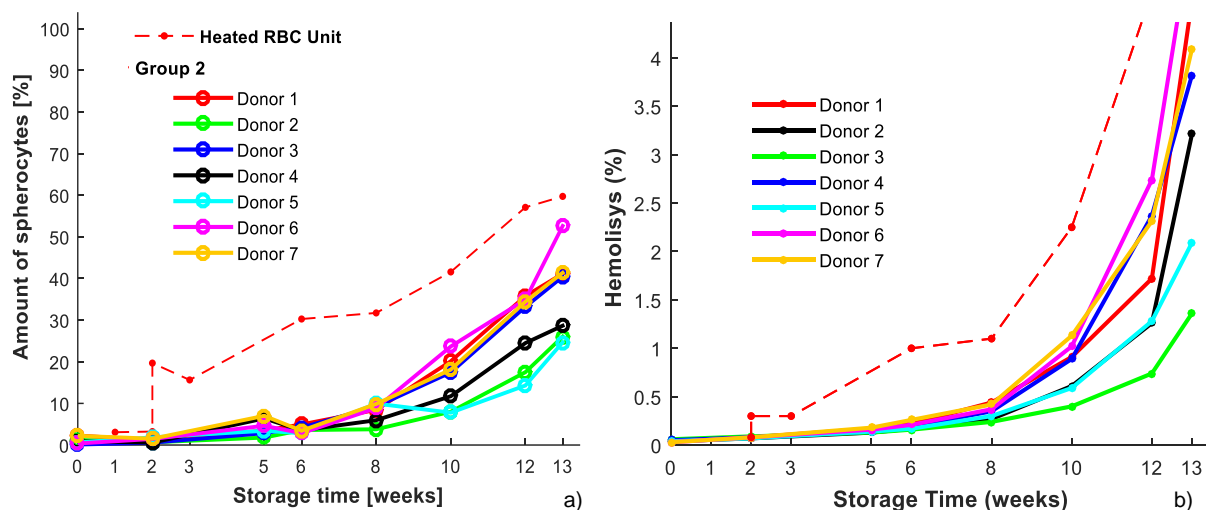


Fig. 59. Comparison between the heated RBC unit (dashed curve) and regular stored RBC units (continuous curves) for S-percentages and hemolysis values. Heat shock was carried out in the second week. Pre- and post-heating measurements were made in this week. Increased values of both assessments for the heated unit are consistent.

Interestingly, there was no increase of the echinocyte proportion after the heating and therefore the measured E-percentages remained constant at a very low level (<6%) until the end of the monitoring (Fig. 60). This suggests that the formation of echinocytes could be inhibited by collateral biochemical alterations in RBCs after the heating or that the residence time of echinocytes in this stage is shortened. The flat response of the E-signal seems to be distinctive for RBCs injured by heat shock. Additionally, both altered RBC units (by heat shock and irradiation) present higher proportions of spherocytes as compared with regular stored RBC units. This strongly supports the idea that the S-percentage is a suitable measure for the degree of damage of RBC units.

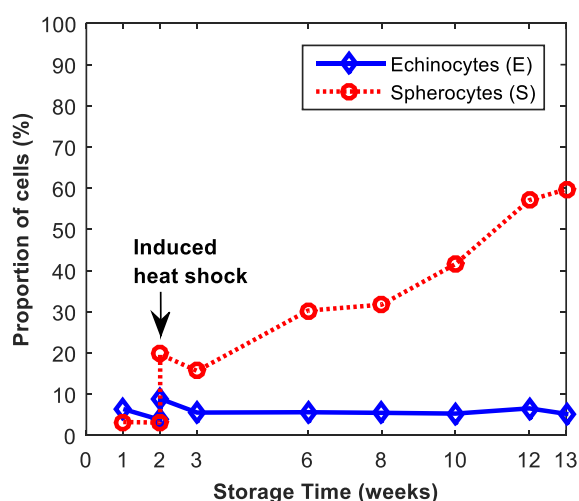


Fig. 60. Inhibition of echinocytes formation after heat damage of one RBC unit. Proportion of echinocytes remains under 6% after the damage (blue curve). Pre- and post-heating step is observed in the S-percentage at week 2.

3.8 Statistical Uncertainty

3.8.1 Measurement Variability

The statistical uncertainty of the morphological measurements was examined with respect to replicates prepared with new sample dilutions and optical readjustment. From a set of 30 RBC samples at different storage times, three replicates per sample were analyzed to calculate the MI, E- and S-percentages as mean values of the replicates. The samples were obtained from RBC units of five donors (group 3) at six different weeks (from week 2 to 12). Figure 61 displays the variability of S-percentages over time calculated as the standard deviation (SD) of the three-replicate sets (see vertical bars). During the shelf life, the maximal SD of S-percentages was 2%. The maximal SD during the whole monitoring occurs at week 12 reaching 5.0% while the average of all SDs for S-percentages was 1.6%. The average SD of S-percentages at each week shows an increase over time suggesting that the measurement variability is directly related to the proportion of spherocytes.

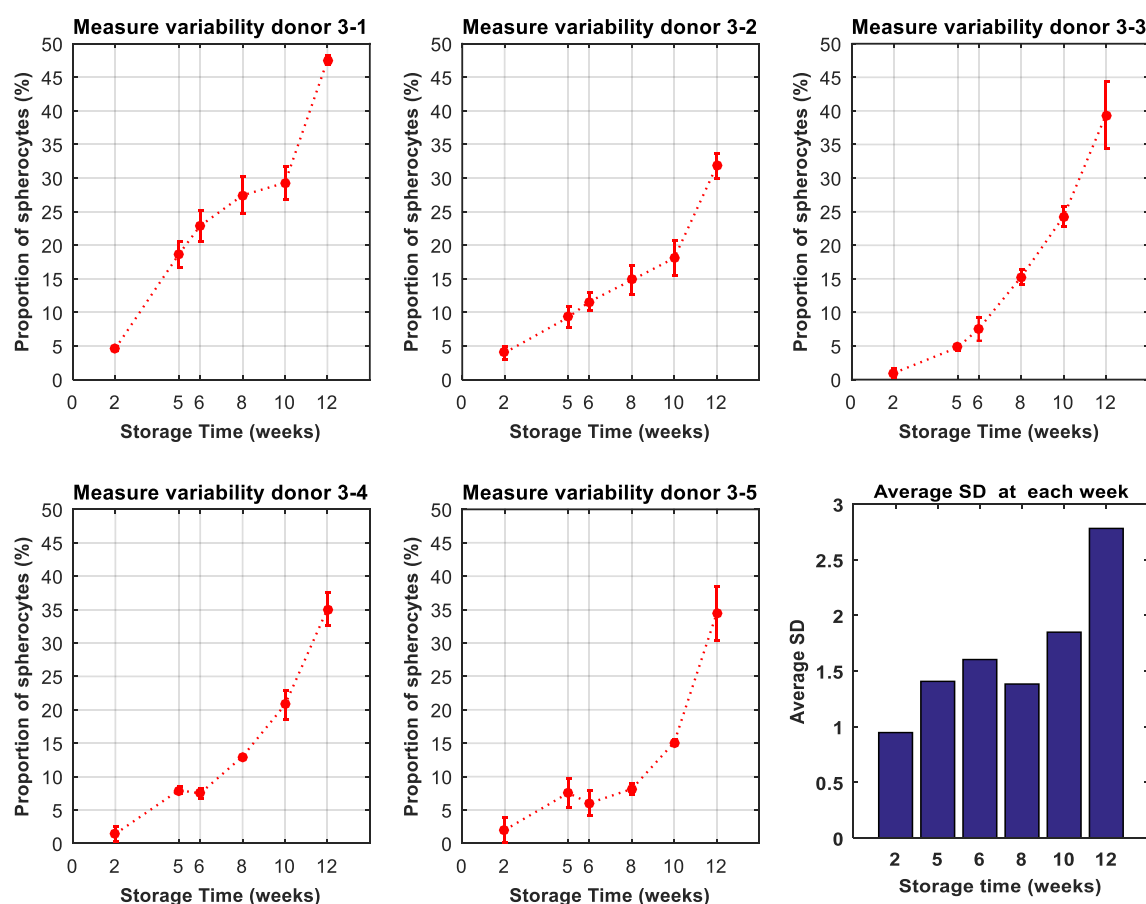


Fig. 61. Measurement variability of S-percentages during the monitoring of five RBC units. Curves connect the mean values of the three-replicate measurements. Vertical bars along the curves represent the corresponding standard deviation. Bar diagram shows the average SD at each week.

The maximal standard deviation of MI during the shelf life is 0.18 (see donor 3-4 at week 5 in figure 62) and the maximal SD during the whole monitoring is 0.23 with a mean value of 2.3 at week 12 (see donor 3-5). The average SD for MI measurements is 0.11. The SDs tend to decrease during the first 6 weeks which coincides with the peak of E-percentages in this set of RBC units (see the measurement variability of E-percentages in figure A-7 of the appendix section). This indicates a role of E-percentage fluctuations in the generation of statistical deviations.

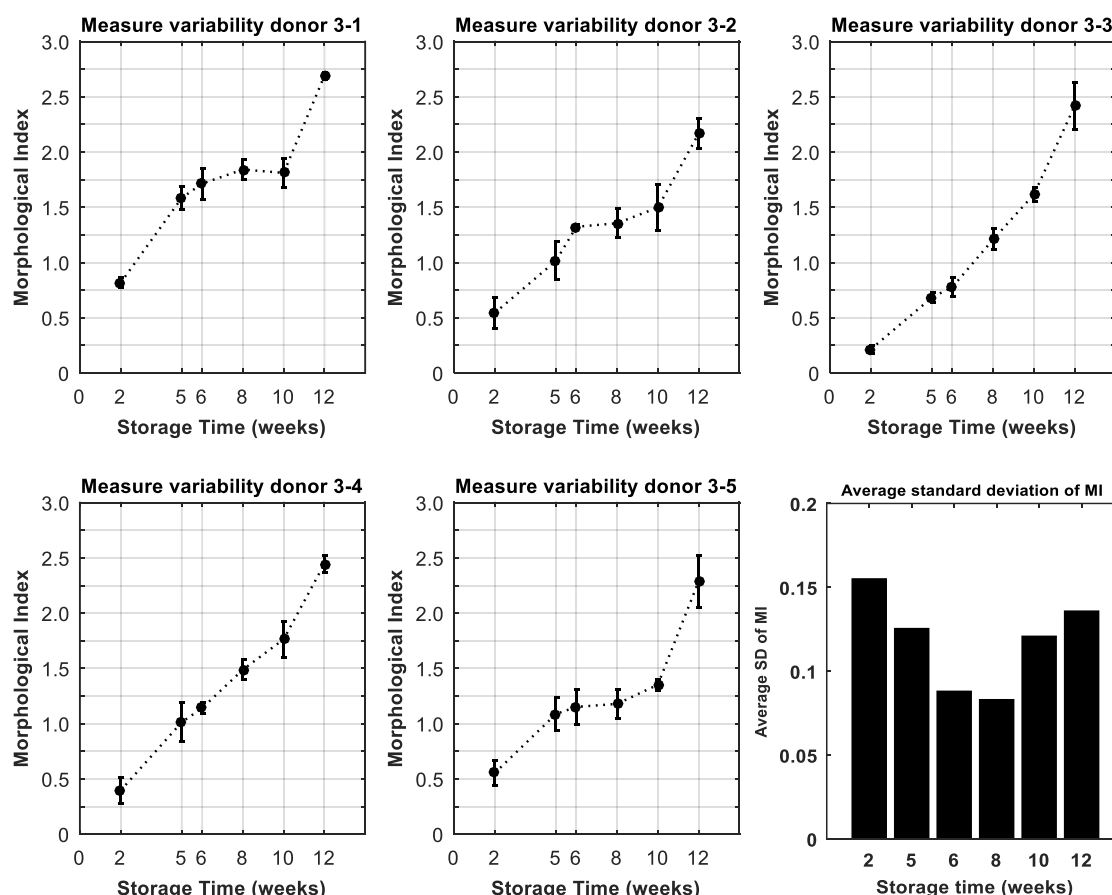


Fig. 62. Measure variability of MI during the monitoring of five RBC units. Curves connect the mean values of the three replicate measurements. Vertical bars along the curves represent the corresponding standard deviation. Bar diagram shows the average SD at each week.

The relative standard deviation is defined as the quotient of standard deviation and the mean value of the replicate measurements. These values tend to be large at the beginning of the storage because the E, S or MI values are comparable to the measurement deviations. A relative SD of 90% is reached in some cases (see donor 3-5 at week 2 for S-percentages). Such high relative deviations are acceptable for small measured values (near to zero) as they are well below the critical values in week 5. The averages of the relative SDs of all RBC units

over time are shown in figure 63. For MI and S-percentage measurements, the relative SD decreases over time. This is expected because of the rising mean values of MI and S-percentages. In the case of E-percentages, the average relative SD of the measurements has little decrease over time.

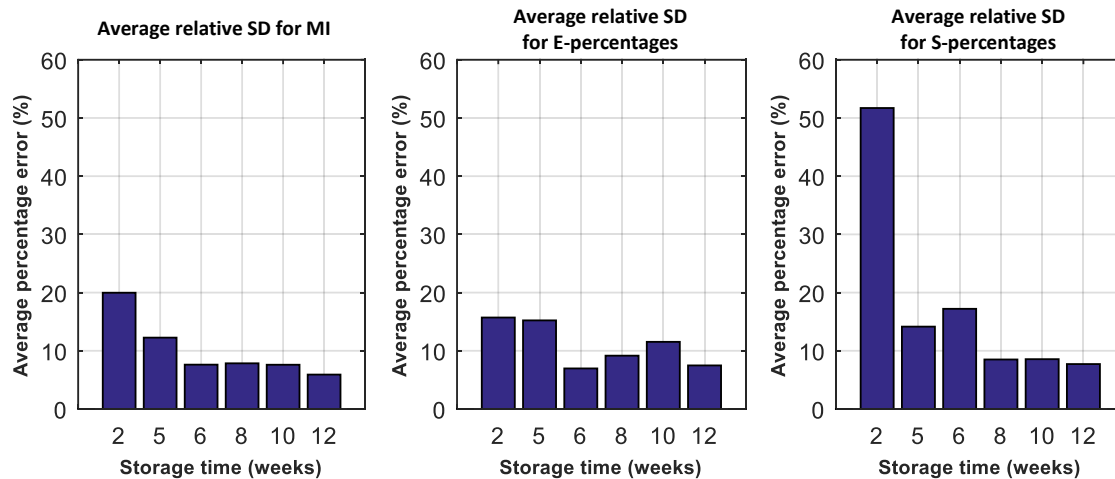


Fig. 63. Average of the five relative SD corresponding to the MI, E and S measurements at each week.

3.8.2 Number of analyzed RBCs for Data Point Generation

The morphometric analysis of each blood sample was carried out by analyzing 1000 RBCs. This number was defined after observing the necessary number of cells for the statistical convergence of the E, S and MI values. Figure 64 shows curves of D-, E-, S-percentages and MI as functions of the number of analyzed RBCs for one single RBC unit monitored at weeks 0, 5, 8 and 13. The transient phase of the curves occurs approximately during the first 400 analyzed RBCs. After this, curves enter into a stationary phase where only very small variations occur. At approximately 500 RBCs the mean values tend to stabilize so that 1000 RBCs were used as a safe basis for computing the results.

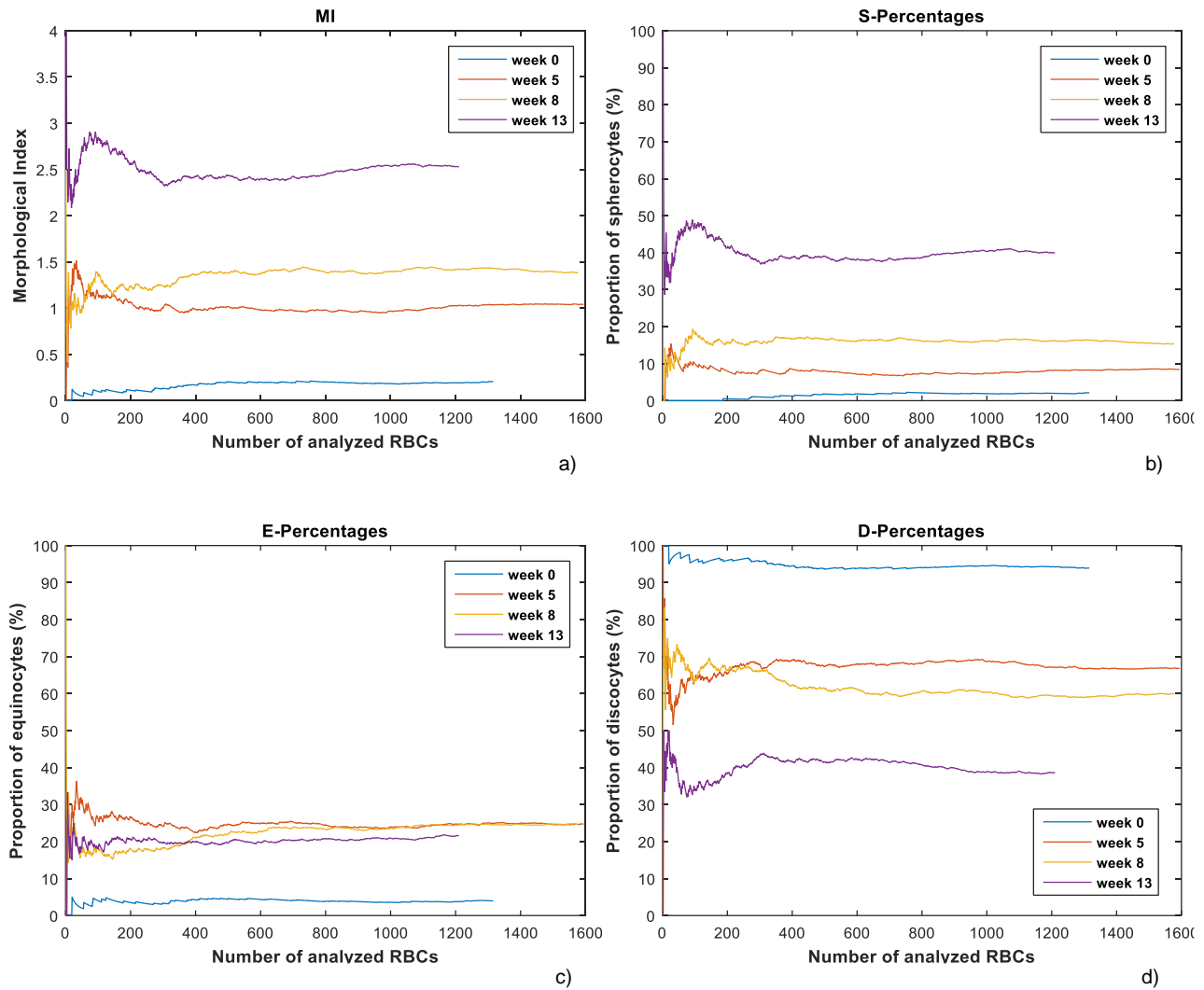


Fig. 64. Transient phase and stabilization point of D, E, S and MI-values as a function of the number of analyzed RBCs at different weeks of storage. Curves were generated for one single RBC unit.

Amongst the curves of different RBC units, the maximal fluctuations in the E- and S-values evaluated on the basis of 500 to 1000 RBCs are approximately 3%. In the case of MI-curves, the maximal variation is approximately 0.15. These small fluctuations of the curves occurring between 500 analyzed RBCs until the end of the analysis are due to statistical variation of the evaluated cell shapes.

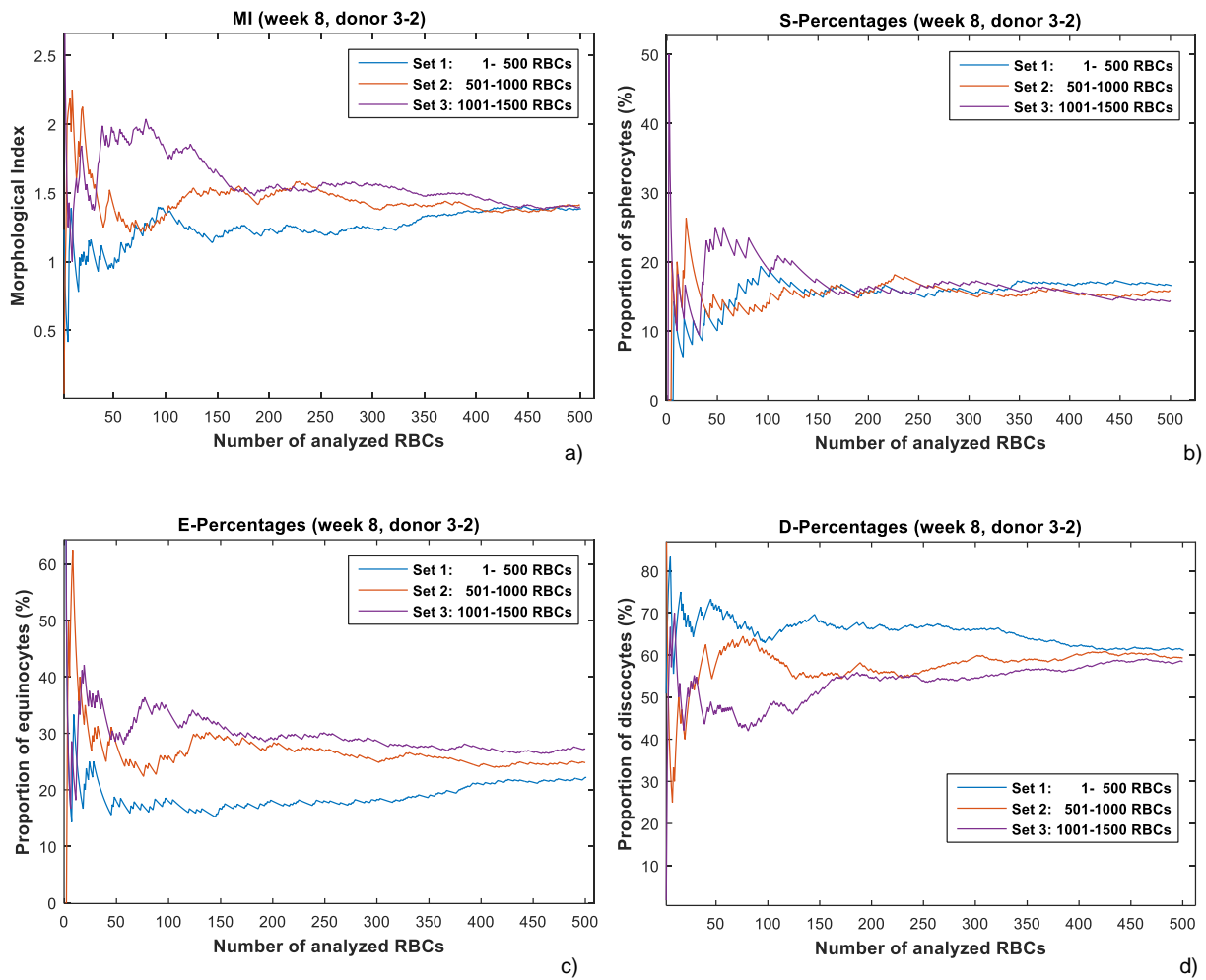


Fig. 65. Transient phase and stabilization point of D, E, S and MI-curves as function of the number of analyzed RBCs at different weeks of storage. Curves were generated for one single RBC unit.

The assumption that 1000 micrographs of individual RBCs are appropriate for statistically meaningful measurements was further tested by comparing the final values of MI, E and S-percentages obtained from 3 subsamples of 500 micrographs each which were obtained from a mother set of 1500 cell micrographs corresponding to one individual eight-week sample (see figure 65). The final values of the curves differ only slightly.

4 DISCUSSION

This study presents a flow cytomorphometry system developed for the quality assessment of stored RBC units. The following aspects of the obtained results will be discussed: 1) development of a system through the combination of the in situ microscope with a flow chamber (Fig. 66), 2) Flow conditions for the imaging of RBCs, 3) Image capture and processing time, 4) Image processing and RBC classification, 5) Sample preparation and 6) Analysis of the monitoring of RBC units.

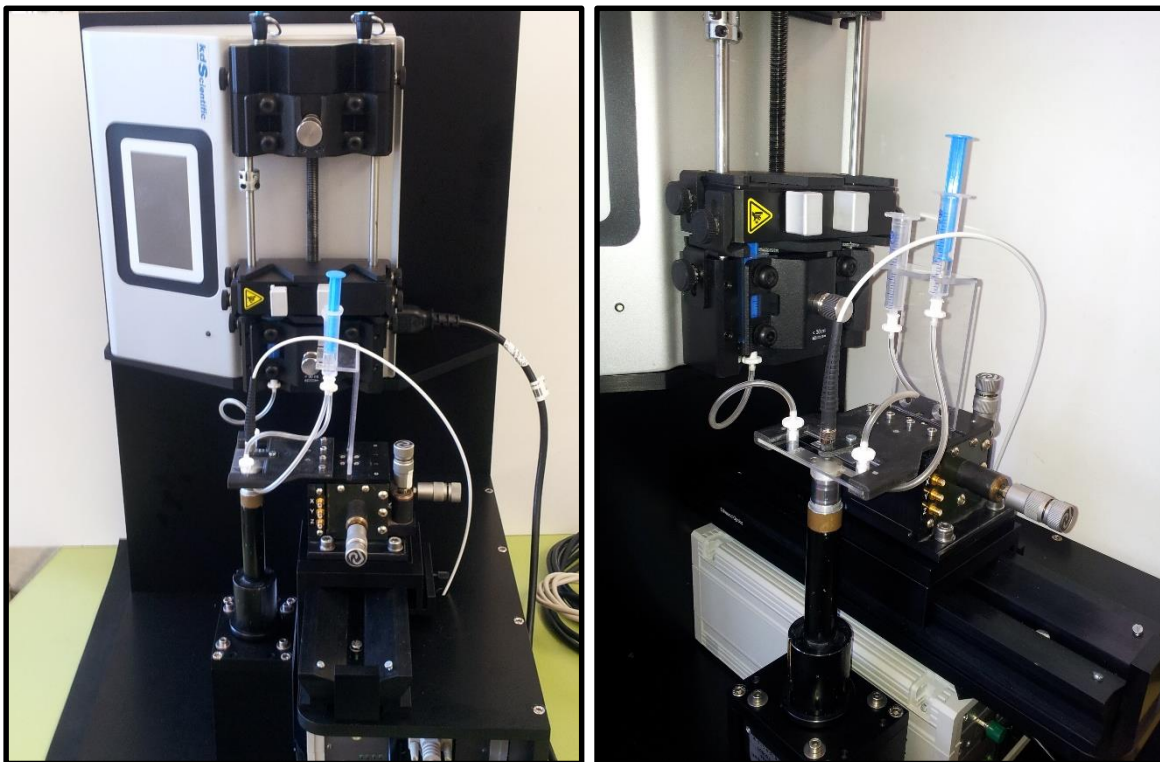


Fig 66. Flow cytomorphometry system.

4.1 Physical Operation of the System

The adaptation of an in situ microscope for morphometry in a flow chamber fully met the expectations of this project: The design of the instrument minimizes the operation complexity through the total automation of the cell analysis once the diluted sample has been introduced in the input reservoir. In addition, the design enables reproducible measurement conditions thanks to the controlled flow condition by means of a configurable and robust setup of the

syringe pump and focus plane in the flow chamber. The exchangeability of the fluidic kit (flow chamber, syringes, silicone tubes and connectors) and the contact free in situ microscope permit the analysis of samples in sterile conditions for reusability. Additionally, the dimensions of the system make it possible to work at a workbench (Fig. 66). In case where the samples must be kept sterile, for example if they are to be re-used for another purpose after the morphometry, the requirement for the change of the entire fluidic kit would impose some limitations. In this respect, the permanent mounting of the syringe on the syringe pump holder, the tubing-flow chamber connection and the optical setup readjustment constitutes a disadvantage of this method since it is not a fast procedure. Moreover, costs would increase considering the actual cost of the fluidic parts (around 10€). However, the system is very suitable for flow cytomorphometry of samples that can be disposed after the morphological analysis. In the particular case of RBC samples, they are disposable after the measurement. Obviously, re-using the fluidic kit requires a thorough rinsing to remove residual cells prior to the introduction of the next sample. The efficiency of this procedure can be checked through the imaging system.

The objective cover cap connected to the water syringe proves to be a practical and simple method to provide the immersion water for the objective lens without direct intervention in the image capture area. The water syringe coupled to the objective cap allows easy refilling in case of drying, which occurred approximately every two hours.

A sporadic effect is the formation of air bubbles due to the water pumping, which can interfere with the imaging if the bubbles are located in the field of view of the lens. This is normally solved by injecting additional water with more pressure. The recommended supervision of the immersion water during the image acquisition is the only aspect that limits the total autonomy of the system once the sample is introduced in the input reservoir.

The syringe pump performs adequately for the propulsion of the suspension into the flow chamber. The configuration of the target volume for pumping cycles according to the introduced sample volume and the precision in the configurable flow rate provide a great flexibility for evaluating RBCs at different flow conditions. Additionally, the USB-port interface of the syringe pump makes it totally controllable from the PC and thereby embeddable to be operated in the in situ microscope application ISM Viewer. In this project, the syringe pump was always manually operated through its touchscreen user interface because the total automation of the system operation was out of the scope of this study. In terms of the system design, an even smaller syringe pump could be used to minimize the dimension of the housing. The pump could even be horizontally positioned considering that the sedimentation effect of the cells in the pumping syringe is not significant in the time interval required for the image

acquisition (≈ 3 min). (The vertical position of the pump was initially chosen to prevent any sedimentation).

The three-axis positioning stage plays a crucial role for the adjustment of the focus plane within the flow channel. It permits the distance compensation of the focal plane due to micrometric tolerances in the mounting of the flow chamber in the 3D-printed chamber holder. Moreover, the micrometric positioning of the flow chamber provides a flexible setup of the focus plane along the channel height making it possible to probe hydrodynamic influences on the RBCs. Based on this positioning mechanism, it was possible to identify the RBC rolling mode at specific height positions and thereby exploit it for discocyte recognition.

As a future option, a Z-motion piezoelectric stage can be implemented in the system to automate the focus adjustment by developing an autofocus algorithm together with a custom-made electrical interface controlled from the PC.

All fluidic, optical and electrical methods and techniques employed in this project can be integrated in an embedded system so that the concept of flow cytomorphometry constitutes a real proposal in terms of implementing an automated system.

4.2 Flow Conditions and RBC Imaging

The most variable characteristic of RBCs under flow is the two-dimensional image projection of discocytes due to their flexible composition and the different orientations of the biconcave shape. This represents some difficulty for the two-dimensional image processing of this cell type. For that reason, the finding of a stable flowing mode of discocytes (rolling mode) simplified considerably their recognition. From the chamber bottom, they are seen as a unique oval profile in the microscopic object field. However, this leads to the requirement for a specific focus range with respect to the channel walls for a given flow rate and cross sectional area of the flow channel. The measurements are therefore prone to considerable variations if the setup reproducibility is not ensured. If the focal height is not kept constant, the effect on the measurement consists of an increased proportion of echinocytes (up to 15% above the real value) because the calculated feature values of deformed and non-rolling discocytes could fall in the detection range of echinocyte features. The robustness of the analysis and measurement consistency for different flow conditions and focal setups can be improved by introducing different or additional features that characterize unequivocally the discocytes without shape restrictions. However, this could lead to an increased computational time for the morphometric analysis.

In the present study, there were many technical points to take into account during the system development and therefore the algorithm optimization was not a decisive aspect once the discocytes could be subjected to a stable flowing mode for effective recognition. Nevertheless, principal results, specifically the S-percentages, are completely independent of the precision of the discocyte recognition since spherocytes are the most unequivocally characterizable state of erythrocytes under flow and thereby they are not prone to recognition errors. Therefore, the reliability of the S-percentage measurement regardless of the flow conditions is secure.

Variability in the rolling tendency of discocytes was observed between samples with the same storage time under the same setup. This means that discocytes of some samples had a greater degree of vertical orientation than discocytes in other samples. A direct connection between the orientability of discocytes of a determined sample and the subsequent deterioration rate of the corresponding RBC unit was not found. This variability could possibly be attributed to air bubbles in the suspension located in the vicinity of the image capture area, which slightly alters the laminar flow and consequently the hydrodynamic conditions to roll. After washing the fluidic parts for the infusion of the next sample, tiny water drops remain over the channel walls and when they come into contact with the new incoming suspension, they act as retaining walls, hindering the homogeneous distribution of the suspension in the channel, thereby generating tiny air bubbles. Normally, this effect is not relevant, provided that the air bubbles are not exactly located in the capture field of the camera and consequently obstruct the passing of the cells through this channel area. If this occurs, the flow channel must be re-emptied. However, donor dependent variations in the rolling quality cannot be discarded and requires further explorations to be confirmed.

Rolling effect of discocytes were reproduced in a flow chamber with reduced channel width ($w=1\text{mm}$, IBIDI VI^{0.1}) by decreasing proportionally the flow rate through the channel in the same factor ($F=0.1\text{ml/min}$). Significant differences in the cell orientation were not found in comparison with the regular flow chamber ($w=5\text{mm}$, ibidi I^{0.1}). A rolling effect with a smaller flow chamber can be useful in the case of a required slower flow rate for analysis, but to the detriment of increased sedimentation in the syringes (due to longer residence time of the suspension in the syringe). The rolling mode can also be reproduced for larger flow channels but it requires increased flow rates to obtain similar flow conditions with respect to the standard fluidic setup used for the monitoring of RBC units.

Rolling RBCs were not observed in the middle range of the channel height, from $\sim 25\mu\text{m}$ to $\sim 75\mu\text{m}$. This confirms the theoretical model [50], in that there is less shear stress around the middle height of the channel ($50\mu\text{m}$) because of the zero velocity gradient at this point. The approximate limits of the two zones with rolling RBCs are defined by a minimal shear rate/stress for rolling under the specific flow conditions ($h=100\mu\text{m}$, $F=0.5\text{ml/min}$ and $\eta=0.01\text{dyn}$

s/cm²). By increasing the flow rate, both limits must migrate closer to the middle height, making the non-rolling zone narrower. As test, the flow rate was increased to 2ml/min, however the rolling zone did not increase as would be expected. On the contrary, no rolling was observed at any point in the channel, not even near the channel walls. In this case, many discocytes were very deformed suggesting that the rolling effect has a requirement for not only a minimum but also a maximum shear stress which was exceeded at this flow rate. In view of the foregoing, the rolling effect seems to occur in a certain range of shear stress and therefore fluidic variables such as the channel geometry, the flow rate and the dynamic viscosity are critical in this respect.

4.3 Image Capture and Processing Time

Approximately 330 cells/min can be analyzed with the defined setup of the cytomorphometry system (mean cell velocity ≈ 1.67 cm/s, concentration $\approx 5 \times 10^6$ cells/ml, fps= 15Hz, computing time ≈ 60 ms/cell). This rate is a consequence of three factors: 1) the cell concentration, 2) the computing time of the image processing and 3) the maximal frame rate capture of the camera. Regarding the cell concentration, only one cell in two images is sharp enough to be analyzed (after discarding analyzed cells due to wrong segmentation). The concentration level was set to this level in order to increase the measurement reliability by avoiding cell overlapping, which can cause false erythrocyte classification. By doubling the cell concentration, the analysis rate can be improved to 500 cells/min without compromising the measurement reliability. At higher cell concentrations, algorithm modifications must be made because unfocused cell traces starts overlapping at the background of focused cells, disturbing the contour recognition of the cell and consequently the calculated feature values. In addition, higher cell concentrations do not provide a benefit if the computing time is not reduced. This means that if the mean computing time required to analyze all sharp cells in one individual image is larger than the period of the frame capture (60ms) there is no real advantage in terms of the real time computing performance. The computing time is 60ms per cell and the frame capture period also is 60ms, so that only one cell per image can be analyzed in real time regardless of the actualization rate of the images. This indicates that the cell concentration and the computing time per cell must both be considered to obtain the maximal time performance of the morphometric analysis of this system. It is technically possible to reduce drastically the computing time by implementing the algorithm code in C++ programming language (using computer visual libraries of OPENCV) and by integrating it in the ISM-Viewer software interface. In this respect, a parallel version of the algorithm was developed in C++ but it was not integrated into the system until the end of this study. Interestingly, the processing time

could be reduced by a factor of up to 7 provided the image entropy transform was avoided. The latter seems to be the more demanding computational calculation. Alternatively, for the further development of the algorithm, the entropy transform could be substituted by a faster texture metric such as the variance transform.

If the cell concentration is kept constant, the only way to improve the analysis performance is by reducing the computational time and simultaneously incrementing the frame acquisition rate. In this case, the computational time must be reduced at least by the same factor as the increase in the acquisition frame rate in order to optimize the time performance. However, the frame acquisition rate is limited by the mean flow velocity of the cells in the channel to avoid over sampling of the cells on the images. The erythrocytes move at approximately 1.67 cm/s (according to $F=0.5\text{ml/min}$ and the corresponding channel dimension for *ibid* $l^{0.1}$). Taking into account the travel distance of the cells along the image width ($225\mu\text{m}$), the frame rate can be increased up to five times (75Hz) without capturing repetitive cells between consecutive frames. Consequently, the computing time must be decreased to 12ms/cell. Under these conditions, the system would be able to analyze up to 2500 RBCs/min while maintaining the same flow conditions as in the present study. Higher cell concentrations and flow would enhance the analysis capacity of the system even more.

The above mentioned conditions determine the time performance of the system for the morphological analysis and show the interrelationship between fluidic, optical, electronic and computational variables. Improvements in this respect are left to further studies.

4.4 Image Processing and RBC Classification

Cell features are based on the contour recognition of the cells. This represents a challenge in the image processing since slight optical effects easily alter the contour fitting of the real cell outline and thereby the parameterization of the cell morphology. This effect mainly corresponds to the partial attenuation of the cell contour luminosity by interference with neighboring cells or other objects. It causes an increase of the measured border roughness feature, which leads to false cell classification as in the case of discocytes or spherocytes. The implemented algorithm detects anomalies in the cell segmentation by recognizing large feature values of equivalent diameter and border roughness that are out of the range of regular erythrocytic cell shapes. In this way, the algorithm automatically discards those cells from the statistical analysis. In some cases, the proportion of these invalidated cells could reach up to 20% in one individual RBC sample. For the purpose of the present study, the contour calculation method developed here showed a good performance for non-overlapped cells,

providing high precision description of the two-dimensional cell contour in 90% of the cases. Improvements in the segmentation method would enhance this percentage, allowing the maximum use of the set of recognized cells for each sample analysis.

Regarding the morphological features, the non-circularity, crucial for the detection of discocytes, can easily be replaced by other equivalent measures of shape features such as the aspect ratio or the eccentricity of the cell contour since the ratio between the maximal and minimal radial distances of the cell contour or the ratio between the area and contour perimeter also describe unequivocally the oval form of the rolling discocytes and the circular form of mature echinocytes and spherocytes. These shape metrics are computationally less expensive than the non-circularity measurement based on the entropy of the radial distances of the cell contour. The texture inhomogeneity based on the average local entropy of the pixel intensities in the inner cell region describes adequately inhomogeneities which normally correspond to superficial bumps or spikes on the echinocyte membrane. However, the membrane folding during the deformation of non-rolling discocytes or even their central concavity are also observed as inhomogeneities of pixel intensities. This interferes with the recognition of non-rolling discocytes by using the texture inhomogeneity of the cell membrane. To overcome this, an alternative texture analysis method based on the pattern recognition of the inhomogeneities on the cell membrane, as proposed in [73], could be tested for further improvements in this respect.

As first approach to the flow morphometry of RBCs by using the *in situ* microscope, the RBC classification was defined to be as simple as possible while remaining representative of the more characteristic morphological stages of stored RBCs. For that reason, the low resolution classification based on only three morphological classes discocytes D, echinocytes E and spherocytes S was implemented in this project.

Stomatocytes were not considered as a separate morphological stage. This variant of erythrocyte deterioration was rarely observed during the monitoring of RBC units and therefore their low statistical apparition does not lead to a relevant alteration in the obtained results. The few existing cases of this cell type were categorized as discocytes since they also exhibit a smooth round shape and their concavity is visually similar to that of discocytes. In this respect, the intermittent occurrence of non-oriented and half-moon shape erythrocytes during the cell imaging was assumed as a particular case of discocyte deformation under flow. However, it was not established whether this morphology represents the deformation of discocytes under flow, or whether it indicates the formation of stomatocytes. One possible option for future work would be to control the pH of the diluted RBC suspension that is analyzed, because the pH is known to affect the formation of stomatocytes [36]. The pH of the initial red cell concentrate

would have to be measured and then kept constant. However, increasing the pH would be a good way to test if the observed cell forms are stomatocytes.

Considering the morphological proximity between sphero-echinocyte (SEs) and spherocytes, the good correlation of hemolysis with S-percentages suggests that the proportion of sphero-echinocytes (SEs) also could have a direct connection with the hemolysis. However, this was not evaluated due to the class separation E-S which categorizes this erythrocyte type in the stage E. In this respect, the inclusion of this cell morphology in the S- category or the separated analysis of the same could refine the equivalency with the hemolysis values.

An increase in the classifier resolution would permit the more precise understanding of the deterioration dynamic of each RBC unit by monitoring the transitions and distributions of the cell subtypes along the storage period. Beyond this, there is no strong evidence that indicates a considerable improvement or paradigm change in the quality estimation of RBC units by enhancing the classifier resolution.

4.5 Sample Preparation

Sample preparation prior to the analysis is straightforward, with the sample being taken directly from the storage bag and diluted in saline solution. However, the small extracted aliquot (1.5µl) makes the dilution factor of 1000 prone to deviations. Alternatively, a larger aliquot (e.g. 15µl) can be extracted - keeping the same dilution factor - to increase the accuracy of the dilution but this requires more buffer solution (15ml) and the final dilution must be subsampled to obtain the required 1.5ml. Morphological measurements for two different dilutions (both by factor 1:1000) were done by extracting 1.5µl and 15µl aliquots of an 8 week stored RBC unit. The measurements did not reveal significant variations between them with respect to the proportion of the cell types, indicating that a 1.5µl sample is adequate.

Transferring the samples to a diluent without the additives of the SAG-M storage medium has the potential to deplete the ATP levels of the cells, but the rapid analysis makes it possible to carry out measurements within minutes, before significant changes occur in the cell morphology. In this respect, echinocytosis was not observed despite the inherent factors associated with the measurement such as temperature changes during the sample extraction and the measurement or the shear stress in the flow chamber.

The walls of the flow chamber were compatible with the analysis, causing no interference. The plastic surface of the flow chamber made it possible to avoid the morphological alterations of RBCs caused by the proximity to glass surfaces [74]. In addition, no adhesion of RBCs to the chamber walls was observed under flow conditions, making it possible to analyze samples

without the use of blocking agents such as bovine serum albumin (BSA), which are used for morphometric analyses with other chamber materials [57, 75]. The advantage of using plain saline is that the cells can be observed without the echinocytosis-reversing effect of the BSA [58].

4.6 Monitoring of RBC Units

The morphological measurements made with the flow morphometry system were validated by comparison to standard assays used by blood banks to monitor RBC storage quality. The measured MI values as well as the S-percentages correlate with the measured hemolysis and ATP levels. Interestingly, the S-percentage seems to be a better lesion monitoring parameter than MI. This might be because hemolysis is more likely to occur in the cells with the most advanced shape changes, so that hemolysis would be linked to the S-percentage. This leads to the suggestion that the percentage of spherocytes could be monitored rather than the commonly measured MI value. Damage to the RBCs induced by both heat shock and irradiation provided additional validation of the morphological measurements, with changes in both the S and MI-signals being consistent with the observed hemolysis.

The storage lesions of 3 sets of RBC units could be quantified through flow cytomorphometry, validating the suitability of this method, as demonstrated by the results of the present study. The inter-group variability is not significant in the first two weeks of storage according to the MI and S-percentages. Only after the end of the shelf life (week 5), the inter-group and inter-donor variability becomes manifest in terms of morphological changes. The low percentages of spherocytes at the beginning of the storage and the measurement tolerance are factors that affect the sensitivity of the morphometry system at low deterioration levels of RBCs. Typical S-percentages of regular stored RBC units were normally below 10 % at the end of the shelf life. Hemolysis turns out to be more sensitive in the range of low deterioration. Despite this, the tolerance of the morphological measurement does not compromise the estimation of critical hemolysis values (around the established limit of 0.8%) when using an equivalent S-threshold (17.7%), since S-percentages of regular stored RBC units during their shelf life are far below this level. In nearly all samples which exceeded the hemolysis limit (0.8%), the S-percentages were also above the S-threshold. For up to eight weeks of storage, the good correlation between hemolysis and S-percentages allows the use of a linear model to estimate hemolysis values in RBC units based on measured S-percentages. The average deviation of the estimated hemolysis values from the measured hemolysis is expected to be $\pm 0.12\%$ according to this model.

The prediction performances obtained here could possibly vary if new RBC-units are to be measured. For new data, the threshold values used here might not be quite as optimal as in the learning set of data for which the thresholds had been optimized. More work with independent sets of data has to be carried out in order to measure and confirm the true prediction probability of S- and MI-values with respect to the reference hemolysis.

The proportion of echinocytes, as the intermediate morphological stage between fresh (D) and hemolytic RBCs (S), depends on the balance between the transition rates $D \rightarrow E$ and $E \rightarrow S$. According to the results, E-percentages do not constitute a clear marker for the characterization of the progressive deterioration of RBCs units since the E-signal stops increasing after the shelf life because the transition rate $E \rightarrow S$ becomes faster than $D \rightarrow E$. For this reason, the non-monotonic E-percentages do not correlate with the monotonously increasing values of hemolysis over the whole monitoring time. Even during the shelf life, while the E-percentages continuously rise, they are not proportional to the measured hemolysis levels. These factors are reflected in the poor correlation of MI with hemolysis as compared to the S-percentage correlation.

Considering the sequential character of the morphological stages (D, E and S), it would be expected that E-percentages could predict the later proportion of spherocytes from the first weeks of storage. However, this does not necessarily occur, presumably due to an inter-donor variability in the transition time between the echinocyte stages (EI, EII, EIII, and SE). Additionally, the proportion of mature echinocytes (EIII and SE, prior to stage S) cannot be inferred from the total count of echinocytes (E-percentages). This unpredictability is reflected in the absence of inter-donor correlation between E-percentages and S-percentages. Nevertheless, E-percentages significantly contribute to the MI determination which provides an alternative description of the deterioration of RBCs. The hemolysis criteria are important, but may not be the only measure of cell aging, so that it could be potentially useful to have an additional description. Apart from hemolysis and ATP, no other biochemical parameter showed a relevant pattern and/or consistency with the morphological measurements (see Tab. A-1 to A-17 in appendix for data).

Based on three replicates for each measuring point, the measurement variability of E and S-percentages is in an acceptable range according to the low SDs (~3%) corresponding to 30 measuring points during the monitoring of 5 RBC units. This validates the proposed flow cytometry method and the suitability of MI and S-percentage for the monitoring of storage lesions. The verified measurement uncertainty is far lower than the percentage differences between the curves of different RBC units, which corroborates the measured inter-donor and inter-group quality differences. In addition, the observed inter-group differences were also confirmed by the standard biochemical reference measurements: hemolysis and

ATP. No specific causes such as age, gender or blood type were identified for these differences. It is possible that they indicate normal quality fluctuations between different donor groups due to seasonal variability. Indeed, samples collected in the warmest month (group 1, collected in September) had the poorest storage quality, consistent with results that have been reported elsewhere and have been associated with the residual white blood cell count after leucoreduction [76]. All RBC units in our study had a leukocyte count $<10E6/\text{unit}$.

The flow cytomorphometry system developed in this project provides suitable conditions for the assessment of the storage lesion in stored RBC units and thereby opens up a broad variety of specific studies in this area such as the preservation differences of erythrocytes with other additive solutions (e.g, AS3), regeneration and damage responses in RBCs or characterization and diagnosis of hemolytic diseases.

The goal of the work presented here was to establish an alternate measurement for the RBC storage quality. The primary measure of RBC storage quality is hemolysis, with RBC units non-eligible for transfusion if they exceed the threshold of 0.8% hemolysis. The defined S threshold detected 98 % of samples that exceeded the hemolysis limit, while the MI threshold detected 95%. More work with independent data sets would have to be carried out to maximize the detection of units above the 0.8% hemolysis limit while minimizing the falsely identified units. The results presented here do, however, demonstrate the potential of the system for use in quality control of stored RBCs.

5 SUMMARY

Red blood cells (erythrocytes) are commonly transfused in therapeutic procedures and surgeries to increase the hemoglobin level of patients. Currently, the only feasible way to supply the increasing demand of red blood cells is via blood donation and subsequent storage. During storage, metabolic alterations, called storage lesions, such as depletion of adenosine triphosphate levels occur in the cells. This is associated with changes in the cell membrane that alter cell morphology and lead to cell lysis. Therefore, adverse post transfusion effects are prevented by maintaining an optimal functionality of stored cells. Nowadays, hemolysis is the gold parameter to measure the deterioration degree of stored red blood cells. However, its measure is not standardized between laboratories and requires complex techniques that do not make it an easy measurement method.

In this study, the morphological analysis of erythrocytes was proposed as alternative method to assess the degree of damage in stored red blood cells. This method is called flow cytormorphometry and uses an existing in situ microscope able to capture images of moving cells directly in the cell suspension. For this purpose, the present project comprised: 1) the solid construction of a device based on the existing in situ microscope and with corresponding adaptation to new fluidic components, 2) algorithm development for morphological analysis of the cells and 3) data acquisition through the morphological and biochemical monitoring of three groups of red blood cell units during 13 weeks of storage. Morphological results were compared with biochemical measurements to validate the proposed method.

The developed apparatus employs a micro-fluidic flow chamber within which images of moving erythrocytes are captured and subsequently processed for morphometric cell analysis. The high frame rate allows to obtain a large data set for statistical analysis. The sample analysis is fully automated once the diluted sample is introduced in the input reservoir. The developed system allows a fast and easy operation and a high degree of reproducibility of the measurement conditions ensuring data consistency.

The image processing algorithm classifies each cell into one of three defined morphological classes (Discocytes, Echinocytes and Spherocytes) that represent the chronologic deterioration of the stored erythrocytes. The rolling mode of moving discocytes was an important characteristic that facilitated their recognition under flow conditions through their oval contour. The classification is performed according to four morphological features (Border Roughness, Non-circularity, Texture Inhomogeneity and Equivalent Diameter) which characterize the cell stages. Rising damage curves of each red blood cell unit based on the percentage of spherocytes and morphological index were consistent with the progressive cell

deterioration during storage. In accordance with literature, the morphological index was calculated by attributing scores to each morphological class and corresponds to the average score based on the occurrences of each class. For data collection, samples of several red blood cell units were assessed for a storage period of 13 weeks. The units were obtained from 3 groups of 5 to 7 blood donors each in different periods. High inter-group variability was found in the morphological assessment. This variability correlates well with the corresponding hemolysis and adenosine triphosphate reference values. Intra-group correlation between spherocytes percentages and hemolysis was also found in the sense that erythrocyte samples with a low proportion of spherocytes tended to exhibit low hemolysis values and high adenosine triphosphate levels. This correlation allowed to formulate a threshold of spherocyte percentages (17.7%) which is equivalent to the established hemolysis threshold (0.8%) used as quality criteria for stored red blood cell units. From 116 analyzed samples, corresponding to different storage times, 98.3% were consistent with the threshold correspondence. Analogously, the morphological index also showed a good correlation with hemolysis but with a slightly lesser agreement (95% of correspondence).

The results presented here show the viability of the proposed method for the assesment of red blood cell storage lesions, validated mainly through the correlation between both, biochemical and morphological measurements. From the point of view of the imaging technique, the flow cytormorphometry principle based on in situ microscopy proved to be a simple, fast and adequate method to evaluate erythrocyte storage lesions and opens the door to other cytormorphometric-based applications.

6 REFERENCES

1. Pittman RN. Regulation of Tissue Oxygenation. Morgan & Claypool Life Sciences; 2011.
2. Tinmouth A, Chin-Yee I. The clinical consequences of the red cell storage lesion. *Transfus Med Rev.* 2001;5(2):91-107.
3. Turgeon M. Clinical Hematology: Theory and Procedures. 5th ed. LWW; 2011.
4. Hoffbrand AV, Pettit JE, Moss PA, Hoelzer D. Grundkurs Hämatologie. 2nd ed. Thieme, Georg; 2002.
5. Mohandas N, Chasis JA. Red blood cell deformability, membrane material properties and shape: Regulation by transmembrane, skeletal and cytosolic proteins and lipids. *Semin Hemat.* 1993; 30:171-192.
6. Liumbruno G, Bennardello F, Lattanzio A, et al. Recommendations for the transfusion of red blood cells. *Blood Transfusion.* 2009;7(1):49-64.
7. Carson JL, Grossman BJ, Kleinman S, et al. Red Blood Cell Transfusion: A Clinical Practice Guideline from the AABB. *Ann. Intern. Med.* 2012; 157(1):49-58.
8. Al-Rubeai M, Naciri M. Stem Cells and Cell Therapy. Springer; 2014.
9. Deutsches Rotes Kreuz. Hämotherapie. 2014; 23:4-12.
10. Cohen B, Matot I. Aged erythrocytes: a fine wine or sour grapes?. *Br J Anaesth.* 2013; 111(1):62-70.
11. Marik PE, Corwin HL. Efficacy of red blood cell transfusion in the critically ill: A systematic review of the literature. *Crit Care Med.* 2008;36(9):2667-74.
12. Purdy FR, Tweeddale MG, Merrick PM. Association of mortality with age of blood transfused in septic ICU patients. *Can J Anaesth.* 1997;44(12):1256-1261.
13. Vamvakas EC, Carven JH. Transfusion and postoperative pneumonia in coronary artery bypass graft surgery: Effect of the length of storage of transfused red cells. *Transfusion.* 1999; 39(7):701-710.
14. Silliman CC, Ambruso DR, Boshkov LK. Transfusion-related acute lung injury. *Blood.* 2005; 105:2266-2273.
15. Malone DL, Dunne J, Tracy JK, et al. Blood transfusion, independent of shock severity, is associated with worse outcome in trauma. *J Trauma.* 2003; 54(5):898-905; discussion 905-907.
16. Högman CF, Meryman HT. Storage parameters affecting red blood cell survival and function after transfusion. *Transfus Med Rev.* 1999;13(4):275-96.
17. Hess JR, An update on solutions for red cell storage, *Vox Sang.* 2006;91(1):13-9.
18. Orlina AR, Josephson AM, McDonald B, et al. Comparative Viability of Blood Stored in ACD and CPD. *Transfusion.* 1969; 9: 62-69.
19. Nakao K, Wada T, Kamiyama T, et al. A direct relationship between adenosine triphosphate level and in vivo viability of erythrocytes. *Nature.* 1962;194:877-878.

20. Simon ER, Chapman RG, Finch CA: Adenine in red cell preservation. *J Clin Invest* 1962; 41 :351–359
21. Beutler E, Kuhl W. Volume control of erythrocytes during storage. The role of mannitol. *Transfusion*.1988; 28:353-357.
22. Hogman CF, Eriksson L, Ericson A, et al. Storage of saline-adenine-glucose-mannitol-suspended red cells in a new plastic container: Polyvinyl chloride plasticized with butyryl-nitrhexyl-citrate. *Transfusion*.1991;31:26-29.
23. Rock G, Tocchi M, Ganz PR, et al. Incorporation of plasticizer into red cells during storage. *Transfusion*. 1984; 24:493-498.
24. Brecher ME, Pineda AA, Torloni AS, et al. Prestorage leukocyte depletion: effect on leukocyte and platelet metabolites, erythrocyte lysis, metabolism, and in vivo survival. *Semin Hematol*. 1991;28:3-9 (suppl)
25. Heaton WAL, Holme S, Smith K, et al: Effects of 3–5 log₁₀ pre-storage leucocyte depletion on red cell storage and metabolism. *Br J Haematol*. 1994; 87:363–368.
26. Hogman CF, Akerblom O, Hedlund K, et al. Red cell suspensions in SAGM medium. Further experience of in vivo survival of red cells, clinical usefulness and plasmasaving effects. *Vox Sang*. 1983;45:217-223,
27. Card RT. Red cell membrane changes during storage. *Trans Med Rev*. 1988; 2:40-47.
- 28 Wolfe LC. The membrane and the lesions of storage in preserved red cells. *Transfusion* 1985; 25(3):185-202.
29. Henkelman S, Dijkstra-Tiekstra MJ, De Wildt-Eggen J, et al. Is red blood cell rheology preserved during routine blood bank storage?. *Transfusion*. 2010; 50:941-948.
30. Chin-Yee I, Arya N, d'Almeida MS. The Red Cell Storage Lesion and its Implication for Transfusion. *Transfusion Science*. *Transfus Sci*.1997;18(3):447-58.
31. Mohandas N, Evans E. Mechanical properties of the red cell membrane in relation to molecular structure and genetic defects. *Annu Rev Biophys Biomol Struct*. 1994;23:787.
32. Pinder JC, Bray D, Gratzer WB. Control of interaction of spectrin and actin by phosphorylation. *Nature*. 1977; 270:752-754
33. Mohandas N, Chasis JA. Red blood cell deformability, membrane material properties and shape: Regulation by transmembrane, skeletal and cytosolic proteins and lipids. *Semin Hemat* 1993;30:171-192.
34. Rmnsby MG, Trotter J, Allan D, et al. Recovery of membrane microvesicles from human erythrocytes stored for transfusion: A mechanism for the erythrocyte discocyte-to spherocyte shape transformation. *Biochem Soc Trans*. 1977;5:126- 128,
35. Bessis M. Red cell shapes. An illustrated classification and its rationale. *Nouv Rev Fr Hematol*. 1972;12:721–741.
36. Lim H. W. G, Wortis M, Mukhopadhyay R. Stomatocyte–discocyte–echinocyte sequence of the human red blood cell. Evidence for the bilayer– couple hypothesis from membrane mechanics. *Proceedings of the National Academy of Sciences of the United States of America*. 2002;99(26):16766-16769.

37. Nakao M, Nakao T, Yamazoe S. Adenosine triphosphate and maintenance of shape of human red cells. *Nature*. 1960;187:945-946.
38. Barshtein G, Gural A, Manny N, et al. Storage-Induced Damage to Red Blood Cell Mechanical Properties Can Be Only Partially Reversed by Rejuvenation. *Transfus Med Hemother*. 2014;41(3):197-204.
39. Haradin AR, Weed RI, Reed CF. Changes in physical properties of stored erythrocytes. *Transfusion*. 1969;9:229-237.
40. Beutler E, Kuhl W, West C. The osmotic fragility of erythrocytes after prolonged liquid storage and after reinfusion. *Blood*. 1982;59:1141-1147,
41. Hess JR: Red cell changes during storage. *Transfus Apher Sci*. 2010;43: 51–59
42. Rother RP, Bell L, Hillmen P, Gladwin MT. The clinical sequelae of intravascular hemolysis and extracellular plasma hemoglobin: a novel mechanism of human disease. *JAMA*. 2005; 293:1653-62.
43. Sowemimo-Coker SO. Red blood cell hemolysis during processing. *Transfus Med Rev*. 2002;16:46-60.
44. European Directorate for the Quality of Medicines & HealthCare. Guide to the preparation, use and quality assurance of blood components, 18th ed. Strasbourg. EDQM;2015:246-246
45. Bundesinstitut für Impfstoffe und biomedizinische Arzneimittel. Bekanntmachung der Richtlinie zur Gewinnung von Blut und Blutbestandteilen und zur Anwendung von Blutprodukten (Hämotherapie) gemäß §§ 12 und 18 des Transfusionsgesetzes (TFG). Bundesanzeiger. 2010; Nr.101:2389
46. FDA summary basis of approval for red blood cells frozen and red blood cells deglycerolized (Reference number 86-0335). US License Number 635-10. Applicant-Department of the Navy, Navy Hospital, Bethesda, MD, 1986
47. Han V, Serrano K, Devine D. A comparative study of common techniques used to measure hemolysis in stored red cell concentrates. *Vox Sang*. 2009; 98(2):116-23
48. Hess JR, Kagen LR, van der Meer PF, et al. Interlaboratory comparison of red-cell ATP, 2,3-diphosphoglycerate and haemolysis measurements. *Vox Sang*. 2005; 89:44-48
49. Janatpour KA, Paglieroni TG, Crocker VL, et al. Visual assessment of hemolysis in red blood cell units and segments can be deceptive. *Transfusion*. 2004;44:984-989
50. Hawkins R. Discrepancy between visual and spectrophotometric assessment of sample haemolysis. *Ann Clin Bioc-hem*. 2002;39:521-2.
51. Turchetti V, De Matteis C, Leoncini F, et al. Variations of erythrocyte morphology in different pathologies. *Clin Hemorheol Microcirc*. 1997;17:209-215.
52. Bossi D, Russo M. Hemolytic anemias due to disorders of red cell membrane skeleton. *Mol Aspects Med*. 1996; 17:171-188
53. Bacus JW, Weens JH, An automated method of differential red blood cell classification with application to the diagnosis of anemia. *J. Histochem. Cytochem*. 1977;25(7), 614–632.
54. Lee H, Chen Y, Cell morphology based classification for red cells in blood smear images. *Pattern Recognit. Lett*. 2014; 49:155-161.

55. Albertini MC, Teodori L, Piatti E, et al. Automated analysis of morphometric parameters for accurate definition of erythrocyte cell shape. *Cytometry*. 2013; 52A: 12-18.
56. Bessis M. Cellules du sang normal et pathologiques. Paris: Masson et Cie; 1972.
57. Piety NZ, Gifford SC, Yang X, et al: Quantifying morphological heterogeneity: a study of more than 1 000 000 individual stored red blood cells. *Vox Sang*. 2015; 109(3):221-30
58. Reinhart SA, Schulzki T, Reinhart WH. Albumin reverses the echinocytic shape transformation of stored erythrocytes. *Clin Hemorheol Microcirc*. 2015; 60(4):437-49
59. Moon I, Daneshpanah M, Anand A, Javidi B. Cell identification computational 3-D holographic microscopy. *Opt. Photonics News*. 2011; 22(6): 18–23.
60. Anand A, Javidi B. Digital holographic microscopy for automated 3D cell identification: an overview. *Chin. Opt. Lett*. 2014;12(6): 060012.
61. Memmolo P, Miccio L, Merola F, et al. 3D morphometry of red blood cells by digital holography. *Cytometry A*. 2014; 85(12):1030-6.
62. Suhr H, Wehnert G, Schneider K, et al. In situ microscopy for on-line characterization of cell-populations in bioreactors, including cell-concentration measurements by depth from focus. *Biotechnol Bioeng*. 1995;47:106-116.
63. Camisard V, Brienne J-, Baussart H, et al. Inline characterization of cell concentration and cell volume in agitated bioreactors using in situ microscopy: application to volume variation induced by osmotic stress. *Biotechnol Bioeng*. 2002;78(1):73-80.
64. Wiedemann P, Guez JS, Wiegemann HB. In situ microscopic cytometry enables noninvasive viability assessment of animal cells by measuring entropy states. *Biotechnol Bioeng*. 2011;108(12): 2884-93.
65. Dunkel T, Dias PA, de León Gallegos EL, et al. In situ microscopy as a tool for the monitoring of filamentous bacteria: a case study in an industrial activated sludge system dominated by *M. parvicella*. *Water Sci Technol*. 2016;73(6):1333-40
66. Ibidi. Instructions μ -Slide I Luer. Version 6.0. 2015.
http://ibidi.com/fileadmin/products/labware/channel_slides/S_801XX_Slide_ILuer/IN_801XX_I_Luer.pdf
67. Batchelor GK. An Introduction to Fluid Dynamics. *Cambridge University Press*. 1967: 211–215.
68. Eibl R, Eibl D, Pörtner R, et al. Cell and Tissue Reaction Engineering. Berlin Heidelberg. Springer; 2009.
69. Dupire J, Socol M, Viallat A. Full dynamics of a red blood cell in shear flow. *Proceedings of the National Academy of Sciences of the United States of America*. 2012;109(51):20808-20813.
70. Asanza DF. Entwicklung eines Frameworks für On-Line Bildanalyse für das In-Situ Mikroskop. *Hochschule Mannheim*. 2009
71. Gonzalez R, Woods RE, Eddins SL. Digital Image Procesing using Matlab. Prentice Hall; 2004:464-470

72. Ferrell JE, Lee KJ, Huestis WH. Membrane bilayer balance and erythrocyte shape: a quantitative assessment. *Biochemistry*. 1985; 24(12): 2849-2857.
73. Ojala T, Pietikainen M, Maenpaa T. Multiresolution gray-scale and rotation invariant texture classification with local binary patterns. *IEEE Trans. Pattern Anal. Mach. Intell.* 2002; 24(7): 971-987. doi: 10.1109/TPAMI.2002.1017623
74. Erikson LE. On the shape of human red blood cells interacting with flat artificial surfaces-the "glass effect." *Biochim Biophys Acta*. 1990;1036(3):193-201
75. Huang S, Hou HW, Kanas T. Towards microfluidic-based depletion of stiff and fragile human red cells that accumulate during blood storage. *Lab Chip*. 2015;15:448–458
76. Chabanel A, Carrat F, Begue S. Quality of leucoreduced red blood cell concentrates: 5 years of follow-up in France. *Vox Sang*. 2008;94:41-47

Own publications:

- Diego Sierra, Kathryn Melzak, Karin Janetzko, et al. Flow morphometry to assess the red blood cell storage lesion. *Cytometry Part A*. 2016. In revision.
- Philippe A. Dias, Thiemo Dunkel, Diego A. S. Fajardo, et al. Image processing for identification and quantification of filamentous bacteria in in situ acquired images. *BioMed Eng OnLine*. 2016;15:64, DOI: 10.1186/s12938-016-0197-7
- Dunkel T, Dias PA, de León Gallegos EL, et al. In situ microscopy as a tool for the monitoring of filamentous bacteria: a case study in an industrial activated sludge system dominated by *M. parvicella*. *Water Sci Technol*. 2016;73(6):1333-40

Oral presentations

- Sierra DA. Automated microscopic evaluation of Red Blood Cell storage lesion, *48th Annual Meeting of the German Society for Transfusion Medicine and Immune Hematology (DGTI 2015)*, Basel, Switzerland.

7 APPENDIX

Biochemical Values					
Donor 1-1. Blood Group O+. Age: 24. Gender: M					
	Week 0	Week 2	Week 5	Week 6	Week 8
	23.09.2014	07.10.2014	28.10.2014	04.11.2014	18.11.2014
Weight (g)	368		305	280	252
Hct (%)	60.1	61.1	62.7	62.2	63.5
Hb (g/dl)	20	18.4	19.5	19.2	20.3
pH 22°C	7.05	6.7	6.49	6.42	6.38
pCO ₂ (mmHg)	38.1	68.6	70.7		51.8
pO ₂ (mmHg)	14	17	24	28	39
Potassium	1.9	28.8	44.5	48.4	55.8
Glucose	517	381	286	276	223
LDH	172	62	104	102	142
Lactate	5.82	18.98	29.64	31.73	35.05
Free Hb (g/l)	1.359	0.483	0.78	0.686	1.121
Hemolysis (%)	0.27	0.10	0.15	0.14	0.20
ATP (μmol/dl)	83.8/88.7	71.0/74.3	59.4/61.5	31.0/32.2	32.2

Tab. A-1. Measured biochemical values of the RBC units corresponding to the donor 1-1 during the monitoring.

Biochemical Values					
Donor 1-2. Blood Group A+. Age: 19. Gender: M					
	Week 0	Week 2	Week 5	Week 6	Week 8
	23.09.2014	07.10.2014	28.10.2014	04.11.2014	18.11.2014
Weight (g)	387		318	293	266
Hct (%)	61.4	62.9	65.1	69.5	64.6
Hb (g/dl)	21.1	20.3	20.4	22.2	21.4
pH 22°C	7.09	6.7	6.43	6.31	6.3
pCO ₂ (mmHg)	37.3	71.1	70.9		63.9
pO ₂ (mmHg)	14	21	27	28	29
Potassium	1.7	31.7	47.5	52.8	58.9
Glucose	487	336	193	174	135
LDH	136	73	164	156	268
Lactate	6.35	22.61	36.45	39.33	40.02
Free Hb (g/l)	1.131	0.659	1.48	1.394	2.77
Hemolysis (%)	0.21	0.12	0.25	0.19	0.46
ATP (μmol/dl)	96.3/85.4	81.3/85.0	51.6/54.5	43.3/40.0	21.9/22.7

Tab. A-2. Measured biochemical values of the RBC units corresponding to the donor 1-2 during the monitoring.

Biochemical Values Donor 1-3. Blood Group B+. Age: 20. Gender: M					
	Week 0	Week 2	Week 5	Week 6	Week 8
	23.09.2014	07.10.2014	28.10.2014	04.11.2014	18.11.2014
Weight (g)	382		319	292	267
Hct (%)	61.9	63.3	21.1	62.7	63.9
Hb (g/dl)	21.1	21	63.1	20.8	21.6
pH 22°C	6.96	6.78	6.68	6.63	6.63
pCO ₂ (mmHg)	50	62.7	59.1	64.1	47.5
pO ₂ (mmHg)	8	12	16	17	21
Potassium	2.2	26.4	41.9	45.6	52.8
Glucose	518	461	388	397	371
LDH	232	70	184	295	646
Lactate	7.01	14.2	22.29	22.13	24.47
Free Hb (g/l)	2.2	0.578	1.74	2.59	6.07
Hemolysis (%)	382		319	292	267
ATP (μmol/dl)	61.9	63.3	21.1	62.7	63.9

Tab. A-3. Measured biochemical values of the stored RBC units corresponding to the donor 1-3 during the monitoring.

Biochemical Values Donor 1-4. Blood Group O+. Age: 44. Gender: F					
	Week 0	Week 2	Week 5	Week 6	Week 8
	23.09.2014	07.10.2014	28.10.2014	04.11.2014	18.11.2014
Weight (g)	357		292	267	240
Hct (%)	60.8	59.7	60.7	61.2	61.8
Hb (g/dl)	19.5	18.7	18.7	18.9	19.9
pH 22°C	6.94	6.71	6.57	6.47	6.46
pCO ₂ (mmHg)	49.5	61.5	55.5	59	47.5
pO ₂ (mmHg)	9	13	18	22	26
Potassium	2.2	26.8	41.8	46	52.5
Glucose	520	407	341	334	296
LDH	152	55	92	98	191
Lactate	8	16.49	26.07	27.29	29.61
Free Hb (g/l)	1.295	0.397	0.81	0.895	1.682
Hemolysis (%)	0.26	0.09	0.17	0.18	0.32
ATP (μmol/dl)	80.1/82.1	66.4/71.4	43.7/45.8	36.7/37.6	23.9/24.3

Tab. A-4. Measured biochemical values of the stored RBC units corresponding to the donor 1-4 during the monitoring.

Biochemical Values Donor 1-5. Blood Group AB-. Age: 29. Gender: M					
	Week 0	Week 2	Week 5	Week 6	Week 8
	23.09.2014	07.10.2014	28.10.2014	04.11.2014	18.11.2014
Weight (g)	406		345	320	293
Hct (%)	64.3	65.3	64.7	65.1	65.6
Hb (g/dl)	21.6	21.3	20.8	20.7	22
pH 22°C	7.01	6.73	6.6	6.5	6.46
pCO ₂ (mmHg)	48.6		61.3		62.8
pO ₂ (mmHg)	10	13	18	19	23
Potassium	2.3	29	44.4	48.8	58.2
Glucose	497	382	288	281	232
LDH	184	154	311	338	740
Lactate	8.01	20.42	30.79	32.02	33.62
Free Hb (g/l)	1.564	1.517	3.2	3.37	8.1
Hemolysis (%)	0.26	0.25	0.54	0.57	1.27
ATP (μmol/dl)	81.3/78.4	42.5/41.7	35.5/38.0	28.9/28.5	16.9/18.2

Tab. A-5. Measured biochemical values of the stored RBC units corresponding to the donor 1-5 during the monitoring.

Biochemical Values Donor 2-1. Blood Group O. Age: 59. Gender: M								
	Week 0	Week 2	Week 5	Week 6	Week 8	Week 10	Week 12	Week 13
	24.02.2015	11.03.2015	01.04.2015	08.04.2015	22.04.2015	07.05.2015	20.05.2015	27.05.2015
Weight (g)	352	340	324	299	277	256	234	214
Hct (%)	62.1	62.3	63.5	64.0	63.3	63.5	61	63
Hb (g/dl)	20.0	19.7	20.1	20.7	19.8	20.5	19.8	20.8
pH 22°C	7.10	6.77	6.49	6.43	6.36	6.31	6.25	6.24
pCO ₂ (mmHg)	30.1	48.7	66.1	65.7	65.9	51.4	48.2	33.7
pO ₂ (mmHg)	13	16	21	21	22	27	29	43
Potassium	4.5	29.9	47.6	51.7	55.3	56.4	52.3	61.7
Glucose	512	402	301	280	243	213	182	163
LDH	34	59	122	164	284	611	1396	2206
Lactate	5.6	19.96	27.69	30.66	32.63	34.37	34.18	31.81
Free Hb (g/l)	0.211	0.420	0.920	1.276	2.36	5.1	8.74	25.8
Hemolysis (%)	0.04	0.08	0.17	0.22	0.44	0.91	1.72	4.59
ATP (μmol/dl)	95.3	106.5	66.4	59.0	35.9	21.0	12	6.6

Tab. A-6. Measured biochemical values of the stored RBC units corresponding to the donor 2-1 during the monitoring.

Biochemical Values Donor 2-2. Blood Group AB. Age: 37. Gender: F								
	Week 0	Week 2	Week 5	Week 6	Week 8	Week 10	Week 12	Week 13
	24.02.2015	11.03.2015	01.04.2015	08.04.2015	22.04.2015	07.05.2015	20.05.2015	27.05.2015
Weight (g)	322	312	296	274	255	235	214	194
Hct (%)	58.6	60.8	59.1	59.3	61.0	60	61.9	59.9
Hb (g/dl)	18.6	18.8	18.7	19	18.5	18.8	19	18.7
pH 22°C	7.05	6.74	6.47	6.40	6.33	6.27	6.2	6.17
pCO ₂ (mmHg)	27.7	43.7	58.9	53.8	53.4	38.7	40.3	28.7
pO ₂ (mmHg)	11	15	20	20	23	32	40	83
Potassium	3.5	24.9	41.2	46.4	49.9	53.2	48.7	57.7
Glucose	548	429	352	333	315	269	243	227
LDH	38	59	85	103	140	228	402	646
Lactate	4.75	16.91	23.62	25.32	28.88	31.73	33.08	31.54
Free Hb (g/l)	0.261	0.435	0.604	0.760	1.125	1.873	3.71	6.36
Hemolysis (%)	0.06	0.09	0.13	0.16	0.24	0.40	0.74	1.36
ATP (μmol/dl)	86.7	105.2	74.7	59.4	42.5	25.2	18.2	9.5

Tab. A-7. Measured biochemical values of the stored RBC units corresponding to the donor 2-2 during the monitoring.

Biochemical Values Donor 2-3. Blood Group B. Age: 32. Gender: M								
	Week 0	Week 2	Week 5	Week 6	Week 8	Week 10	Week 12	Week 13
	24.02.2015	11.03.2015	01.04.2015	08.04.2015	22.04.2015	07.05.2015	20.05.2015	27.05.2015
Weight (g)	351	339	323	301	280	260	237	217
Hct (%)	59.7	61.6	61.9	61.6	63.6	60.8	59.5	59.2
Hb (g/dl)	20.5	20.3	20.9	21.2	20.9	20.9	20.5	20.2
pH 22°C	7.12	6.79	6.49	6.42	6.34	6.26	6.23	6.2
pCO ₂ (mmHg)	26.9	42.5	62.1	54.8	57.8	49.4	47.7	36.3
pO ₂ (mmHg)	16	21	30	34	42	50	72	144
Potassium	3.8	24.7	40	44.7	50.3	52.4	48.7	59.5
Glucose	560	409	300	273	230	203	168	153
LDH	30	53	89	122	215	500	1145	1829
Lactate	5.18	19.47	29.84	32.04	35.39	37.46	37.99	36.33
Free Hb (g/l)	0.232	0.437	0.795	1.057	2.03	4.75	11.99	18.9
Hemolysis (%)	0.05	0.08	0.14	0.19	0.35	0.89	2.37	3.82
ATP (μmol/dl)	69.3	81.7	57.0	50.3	32.2	13.2	9.5	4.1

Tab. A-8. Measured biochemical values of the stored RBC units corresponding to the donor 2-3 during the monitoring.

Biochemical Values Donor 2-4. Blood Group B. Age: 54. Gender: M								
	Week 0	Week 2	Week 5	Week 6	Week 8	Week 10	Week 12	Week 13
	24.02.2015	11.03.2015	01.04.2015	08.04.2015	22.04.2015	07.05.2015	20.05.2015	27.05.2015
Weight (g)	374	362	345	322	300	279	257	233
Hct (%)	62.0	64.0	63.6	62.9	67.2	64.7	65.7	57.6
Hb (g/dl)	20.7	20.5	21.1	21.5	21.5	21.1	21.3	20.7
pH 22°C	7.08	6.76	6.47	6.42	6.33	6.31	6.25	6.26
pCO ₂ (mmHg)	31.5	49.7	70.2	64.4	66.2	58.1	56.2	49.9
pO ₂ (mmHg)	14	16	21	20	22	72	24	27
Potassium	3.8	27.1	44.8	51.3	54.3	58.1	55.0	62
Glucose	514	392	296	274	231	199	173	158
LDH	34	52	94	122	200	388	814	1293
Lactate	5.99	20.14	29.22	29.21	33.72	35.19	35.25	34.21
Free Hb (g/l)	0.226	0.413	0.766	0.993	1.786	3.65	7.85	15.67
Hemolysis (%)	0.04	0.07	0.13	0.17	0.27	0.61	1.26	3.21
ATP (μmol/dl)	80.1	101.1	61.1	54.1	38.4	16.1	12.8	5.4

Tab. A-9. Measured biochemical values of the stored RBC units corresponding to the donor 2-4 during the monitoring.

Biochemical Values Donor 2-5. Blood Group A. Age: 22. Gender: F								
	Week 0	Week 2	Week 5	Week 6	Week 8	Week 10	Week 12	Week 13
	24.02.2015	11.03.2015	01.04.2015	08.04.2015	22.04.2015	07.05.2015	20.05.2015	27.05.2015
Weight (g)	300	289	273	250	228	207	183	158
Hct (%)	53.5	54.0	55.0	54.6	55.6	55.2	56.3	54.7
Hb (g/dl)	17.3	17.5	18.1	18.1	17.8	17.9	17.5	18.3
pH 22°C	6.98	6.64	6.37	6.31	6.23	6.14	6.12	6.15
pCO ₂ (mmHg)	26.5	42.6	57.3	55	46.6	47.3	34.4	29
pO ₂ (mmHg)	16	25	28	33	40	45	114	162
Potassium	1.3	20.9	34.7	38.7	44.6	47.4	51.2	51
Glucose	539	422	333	313	278	244	222	209
LDH	21	17.35	76	96	161	283	570	906
Lactate	6.02	32.00	24.92	27.12	28.87	30.67	32.34	30.15
Free Hb (g/l)	0.132	0.273	0.571	0.693	1.191	2.35	5.11	8.43
Hemolysis (%)	0.04	0.07	0.14	0.17	0.30	0.59	1.28	2.09
ATP (μmol/dl)	102.3	109	78	65.6	47.0	27.7	15.7	14.4

Tab. A-10. Measured biochemical values of the stored RBC units corresponding to the donor 2-5 during the monitoring.

Biochemical Values Donor 2-6. Blood Group B. Age: 51. Gender: F								
	Week 0	Week 2	Week 5	Week 6	Week 8	Week 10	Week 12	Week 13
	24.02.2015	11.03.2015	01.04.2015	08.04.2015	22.04.2015	07.05.2015	20.05.2015	27.05.2015
Weight (g)	332	321	303	281	260	241	216	193
Hct (%)	60.0	57.7	58.4	58.0	60.6	57.4	56.7	52.8
Hb (g/dl)	19.1	18.5	18.7	18.7	19.4	19.1	18.6	18.8
pH 22°C	7.03	6.76	6.49	6.42	6.36	6.29	6.25	6.3
pCO ₂ (mmHg)	30.1	39.5	56.5	56.9	52.0	45.5	33.6	33.1
pO ₂ (mmHg)	16	25	34	47	72	142	172	182
Potassium	1.5	24.6	40.8	45.4	49.8	52.3	58.3	56.8
Glucose	556	440	346	322	286	261	234	205
LDH	29	46	84	111	209	471	1187	2060
Lactate	5.49	17.28	25.87	28.14	30.19	31.24	31.85	30.65
Free Hb (g/l)	0.163	0.353	0.707	0.946	1.808	4.58		21.2
Hemolysis (%)	0.03	0.08	0.16	0.21	0.37	1.02		5.32
ATP (μmol/dl)	80.9	80.1	54.9	47.5	31.4	15.7	10.3	9.1

Tab. A-11. Measured biochemical values of the stored RBC units corresponding to the donor 2-6 during the monitoring.

Biochemical Values Donor 2-7. Blood Group AB. Age: 35. Gender: M								
	Week 0	Week 2	Week 5	Week 6	Week 8	Week 10	Week 12	Week 13
	24.02.2015	11.03.2015	01.04.2015	08.04.2015	22.04.2015	07.05.2015	20.05.2015	27.05.2015
Weight (g)	388	378	360	338	317	294	274	250
Hct (%)	64.0	65.7	64.3	63.3	68.4	63.8	65.6	60.8
Hb (g/dl)	21.6	22.1	21.5	21.4	22.4	21.9	22.5	22.5
pH 22°C	7.09	6.77	6.51	6.45	6.38	6.31	6.28	6.27
pCO ₂ (mmHg)	31.8	51.0	66.4	64.1	65.7	64	52.4	49.4
pO ₂ (mmHg)	15	20	22	23	24	25	31	36
Potassium	1.7	31.3	46.5	50.9	56.4	58.6	64.4	63.1
Glucose	485	346	240	216	175	137	107	87
LDH	25	66	144	199	371	781	1774	2801
Lactate	6.13	20.99	30.34	33.08	34.52	35.49	39.00	34.23
Free Hb (g/l)	0.179	0.503	1.098	1.488	2.96	6.82		23.5
Hemolysis (%)	0.03	0.08	0.18	0.26	0.42	1.13		4.09
ATP (μmol/dl)	90.4	86.7	54.9	49.1	33.0	16.5	2.9	7.8

Tab. A-12. Measured biochemical values of the stored RBC units corresponding to the donor 2-7 during the monitoring.

Biochemical Values Donor 3-1. Blood Group AB+. Age: 34. Gender: M								
	Week 0	Week 2	Week 5	Week 6	Week 8	Week 10	Week 12	Week 13
	29.01.2016	09.02.2016	01.03.2016	08.03.2016	22.03.2016	05.04.2016	19.04.2016	26.04.2016
Weight (g)	374	354	333	316	295	276	253	230
Hct (%)	65	66.2	64.4	66.8	65.2	64	0.578	0.569
Hb (g/dl)	20.7	21	20.3	20.1	20.4	20.5	20.5	20.8
pH 22°C	6.89	6.66	6.46	6.39	6.31	6.27	6.16	6.16
pCO ₂ (mmHg)	38.8	58	55.2	62.4	59.5	50	51.9	40.8
pO ₂ (mmHg)	14.0	18	23	24	26	30	35	41
Potassium	9.2	54.8	60.7	68.2	69.2	63.6	70.5	68.6
Glucose	479	390	276	250	203	177	126	103
LDH	41	147	715	874	1752	2967		8630
Lactate	13.02	21.56	30.16	32.16	32.75	35.09	36.55	35.88
Free Hb (g/l)	0.276	1.312	6.530	7.42	15.14	31.1	31.8	195
Hemolysis (%)	0.05	0.21	1.15	1.23	2.58	5.46	15.42	93.22
ATP (μmol/dl)	103.6	91.2	49.1	44.2	26.4	15.3	5	

Tab. A-13. Measured biochemical values of the stored RBC units corresponding to the donor 3-1 during the monitoring.

Biochemical Values Donor 3-2. Blood Group A+. Age: 51. Gender: M								
	Week 0	Week 2	Week 5	Week 6	Week 8	Week 10	Week 12	Week 13
	29.01.2016	09.02.2016	01.03.2016	08.03.2016	22.03.2016	05.04.2016	19.04.2016	26.04.2016
Weight (g)	355	335	314	293	273	257	234	213
Hct (%)	62.4	61.5	60.6	62.5	63.3	65	0.593	0.58
Hb (g/dl)	19.5	19.1	19.5	19.2	19.5	20.2	18.8	19.7
pH 22°C	6.86	6.63	6.44	6.41	6.32	6.25	6.13	6.15
pCO ₂ (mmHg)	39.3	54.5	55.7	49.3	53.4	47.8	46.2	36.3
pO ₂ (mmHg)	11	14	19	22	24	25	36	55
Potassium	7.1	25.5	42.6	49.3	54.5	54.6	61.9	62.5
Glucose	473	377	286	265	225	205	170	138
LDH	31	58	150	176	395	890	2125	3798
Lactate	11.93	19.32	27.78	28.93	32.1	31.76	33.06	34.24
Free Hb (g/l)	0.189	0.498	1.195	1.477	3.41	8.5	18.7	11.24
Hemolysis (%)	0.04	0.10	0.24	0.29	0.64	1.48	9.89	5.67
ATP (μmol/dl)	101.1	96.6	62.3	55.3	35.5	19.8	7.4	

Tab. A-14. Measured biochemical values of the stored RBC units corresponding to the donor 3-2 during the monitoring.

Biochemical Values Donor 3-3. Blood Group AB+. Age: 46. Gender: M								
	Week 0	Week 2	Week 5	Week 6	Week 8	Week 10	Week 12	Week 13
	29.01.2016	09.02.2016	01.03.2016	08.03.2016	22.03.2016	05.04.2016	19.04.2016	26.04.2016
Weight (g)	362	341	321	303	281	266	243	222
Hct (%)	64.6	62.8	62.0	61.7	64.9	63	0.625	0.518
Hb (g/dl)	20.2	19.8	20	19.9	20.8	20.3	20.3	18.6
pH 22°C	6.91	6.73	6.57	6.53	6.45	6.4	6.34	6.36
pCO ₂ (mmHg)	43.7	57.6	58	53.7	51.7	45.9	40	33.3
pO ₂ (mmHg)	9.0	13	18	20	24	33	50	66
Potassium	6.5	23.9	38.8	47.5	54.6	54.8	61.4	61.7
Glucose	473	401	315	287	249	236	199	177
LDH	30	51	137	162	375	799	1742	2821
Lactate	10.37	16.58	25.4	26.73	30.03	30.24	30.78	32.11
Free Hb (g/l)	0.242	0.477	1.352	1.612	4.11	9.6	18.41	60.9
Hemolysis (%)	0.04	0.09	0.26	0.31	0.69	1.76	9.01	32.57
ATP (μmol/dl)	88.7	78	51.6	44.6	31	17.7	5.4	

Tab. A-15. Measured biochemical values of the stored RBC units corresponding to the donor 3-3 during the monitoring.

Biochemical Values Donor 3-4. Blood Group AB+. Age: 44. Gender: M								
	Week 0	Week 2	Week 5	Week 6	Week 8	Week 10	Week 12	Week 13
	29.01.2016	09.02.2016	01.03.2016	08.03.2016	22.03.2016	05.04.2016	19.04.2016	26.04.2016
Weight (g)	374	354	333	314	292	276	254	232
Hct (%)	64.3	63.5	63.4	63.0	64	63	0.599	0.385
Hb (g/dl)	21.2	20.8	20.9	21	21	21	21.2	21.4
pH 22°C	6.87	6.7	6.49	6.43	6.36	6.3	6.2	6.26
pCO ₂ (mmHg)	44	52.8	62.9	59.2	56.8	49.3	49.1	34.5
pO ₂ (mmHg)	13	16	20	27	33	41	59	114
Potassium	7.2	26.5	42	50.8	55.6	61.2	63.4	62.4
Glucose	481	389	287	262	224	192	152	123
LDH	34	66	183	271	639	1423	3074	6060
Lactate	11.35	18.92	n.T.	30.19	32.81	32.83	33.73	36.67
Free Hb (g/l)	0.257	0.570	1.892	2.36	6.07	15.6	32.6	100.2
Hemolysis (%)	0.04	0.10	0.33	0.42	1.04	2.75	15.29	46.64
ATP (μmol/dl)	92	85	48.7	45.8	27.7	14.4	4.1	

Tab. A-16. Measured biochemical values of the stored RBC units corresponding to the donor 3-4 during the monitoring.

Biochemical Values Donor 3-5. Blood Group B+. Age: 26. Gender: M								
	Week 0	Week 2	Week 5	Week 6	Week 8	Week 10	Week 12	Week 13
	29.01.2016	09.02.2016	01.03.2016	08.03.2016	22.03.2016	05.04.2016	19.04.2016	26.04.2016
Weight (g)	349	329	309	291	271	251	227	204
Hct (%)	61.8	61.4	59.2	59.8	60.8	64	0.588	0.566
Hb (g/dl)	19.9	19.1	19.3	19.3	19.3	20.1	19.1	19.5
pH 22°C	6.87	6.7	6.51	6.45	6.35	6.29	6.2	6.2
pCO ₂ (mmHg)	44.2	49.8	54.8	52.0	55.4	48.4	44.7	32.3
pO ₂ (mmHg)	12	19	22	27	32	51	102	146
Potassium	5.7	20.7	36.5	43.9	50.1	51.3	59.2	60.5
Glucose	496	419	318	291	253	227	193	171
LDH	66	54	89	94	146	306	756	1412
Lactate	10.13	16.9	25.51	27.89	30.88	30.94	34.08	34.49
Free Hb (g/l)	0.555	0.442	0.781	0.899	1.509	3.6	9.16	16.7
Hemolysis (%)	0.11	0.09	0.17	0.19	0.31	0.65	4.77	8.52
ATP (μmol/dl)	97.8	90	56.1	49.9	31.8	18.6	5	

Tab. A-17. Measured biochemical values of the stored RBC units corresponding to the donor 3-5 during the monitoring.

E-percentage range ($E_{\min} - E_{\max}$)				
	Week 0	Week 5	Week 8	Week 13
Group 1	1.6% - 6.5%	6.0% - 36.6%	9.8% - 39.9%	19.1% - 34.0%
Group 2	2.7% - 9.7%	8.0% - 21.1%	9.0% - 23.5%	13.9% - 28.8%
Group 3	3.2% - 4.6%	17.8% - 28.4%	17.8% - 33.5%	14.0% - 3.9%

Tab. A-18 Proportion of echinocytes (%) of the three donor groups at specific points of time. The E-percentage range ($E_{\min} - E_{\max}$) is defined as the minimal and maximal intra-group proportion of echinocytes measured in a specific week.

S-percentage range ($S_{\min} - S_{\max}$)				
	Week 0	Week 5	Week 8	Week 13
Group 1	0.0% - 2.4%	1.0% - 12.8%	5.6% - 21.1%	34.6% - 64.9%
Group 2	0.1% - 2.3%	1.8% - 7.0%	3.8% - 9.9%	24.7% - 52.6%
Group 3	0.8% - 2.9%	4.2% - 8.9%	8.2% - 15.2%	37.8% - 52.7%

Tab. A-19 Proportion of spherocytes (%) of the three donor groups at specific points of time. The S-percentage range ($S_{\min} - S_{\max}$) is defined as the minimal and maximal intra-group proportion of spherocytes measured in a specific week.

Hemolysis range ($H_{\min} - H_{\max}$)				
	Week 0	Week 5	Week 8	Week 13
Group 1	0.4 % - 0.21%	0.15% - 0.54%	0.2% - 1.3%	--
Group 2	0.03% - 0.06%	0.13% - 0.18%	0.2% - 0.4%	1.4% - 5.3%
Group 3	0.04% - 0.11%	0.17% - 0.33%	0.3% - 1.0%	3.7% - 28.8%

Tab. A-20 Hemolysis percentages of the three donor groups at specific points of time. The hemolysis range ($H_{\min} - H_{\max}$) is defined as the minimal and maximal intra-group hemolysis measured in a specific week.

ATP range ($ATP_{\min} - ATP_{\max}$)				
	Week 0	Week 5	Week 8	Week 13
Group 1	60.0 - 90.0	24.0 - 60.3	10.5 - 32.2	--
Group 2	69.3 - 102.3	54.9 - 78.0	31.4 - 47.0	4.1 - 14.4
Group 3	88.7 - 101.1	48.7 - 62.3	27.7 - 35.5	--

Tab. A-21 ATP values of the three donor groups at specific points of time. The ATP range ($ATP_{\min} - ATP_{\max}$) is defined as the minimal and maximal intra-group ATP level measured in a specific week.

Measurement variability of MI (mean±SD)						
	Week 2	Week 5	Week 6	Week 8	Week 10	Week 12
Donor 3-1	0.81 ± 0.04	1.58 ± 0.1	1.71 ± 0.14	1.84 ± 0.0	1.81 ± 0.13	2.69 ± 0.03
Donor 3-2	0.54 ± 0.14	1.01 ± 0.17	1.32 ± 0.01	1.35 ± 0.13	1.5 ± 0.2	2.16 ± 0.13
Donor 3-3	0.21 ± 0.03	0.68 ± 0.04	0.78 ± 0.08	1.21 ± 0.09	1.67 ± 0.06	2.41 ± 0.21
Donor 3-4	0.39 ± 0.12	1.01 ± 0.17	1.14 ± 0.05	1.49 ± 0.09	1.76 ± 0.16	2.44 ± 0.07
Donor 3-5	0.55 ± 0.11	1.09 ± 0.14	1.15 ± 0.15	1.18 ± 0.13	1.35 ± 0.05	2.28 ± 0.23

Tab. A-22. Measurement variability of MI for RBC units of the donor group 3. Each value expresses the mean value and the corresponding standard deviation of three replicates at each measurement point.

Measurement variability of E-percentages (mean±SD)						
	Week 2	Week 5	Week 6	Week 8	Week 10	Week 12
Donor 3-1	23.4 ± 1.5	26.0 ± 2.1	22.8 ± 1.3	18.8 ± 2.0	13.9 ± 0.8	12.6 ± 0.4
Donor 3-2	13.8 ± 3.9	22.1 ± 4.6	29.8 ± 2.3	24.6 ± 0.9	23.7 ± 3.9	23.1 ± 2.3
Donor 3-3	6.7 ± 0.4	17.8 ± 2.2	16.1 ± 1.6	17.9 ± 1.7	16.2 ± 1.0	17.9 ± 1.6
Donor 3-4	12.9 ± 3.5	24.6 ± 6.3	30.7 ± 1.2	33.5 ± 3.5	29.0 ± 5.1	27.7 ± 2.0
Donor 3-5	18.2 ± 2.1	28.4 ± 2.7	34.0 ± 2.5	30.8 ± 3.5	23.8 ± 2.8	22.7 ± 1.9

Tab. A-23. Measurement variability of E-percentages for RBC units of the donor group 3. Each value expresses the mean value and the corresponding standard deviation of three replicates at each measurement point.

Measurement variability of S-percentages (mean±SD)						
	Week 2	Week 5	Week 6	Week 8	Week 10	Week 12
Donor 3-1	4.6 ± 0.2	18.7 ± 1.9	23.0 ± 2.3	27.4 ± 2.7	29.3 ± 2.5	47.5 ± 0.7
Donor 3-2	4.0 ± 1.0	9.3 ± 1.5	11.6 ± 1.4	14.8 ± 2.1	18.1 ± 2.7	31.8 ± 1.8
Donor 3-3	1.0 ± 0.6	4.8 ± 0.4	7.5 ± 1.8	15.3 ± 1.1	24.3 ± 1.5	39.4 ± 5.0
Donor 3-4	1.4 ± 1.1	8.0 ± 0.5	7.5 ± 0.7	13.0 ± 0.1	20.8 ± 2.2	35.1 ± 2.4
Donor 3-5	2.0 ± 1.8	7.6 ± 2.2	6.0 ± 1.9	8.2 ± 0.8	15.1 ± 0.4	34.4 ± 4.1

Tab. A-24. Measurement variability of S-percentages for RBC units of the donor group 3. Each value expresses the mean value and the corresponding standard deviation of three replicates at each measurement point.

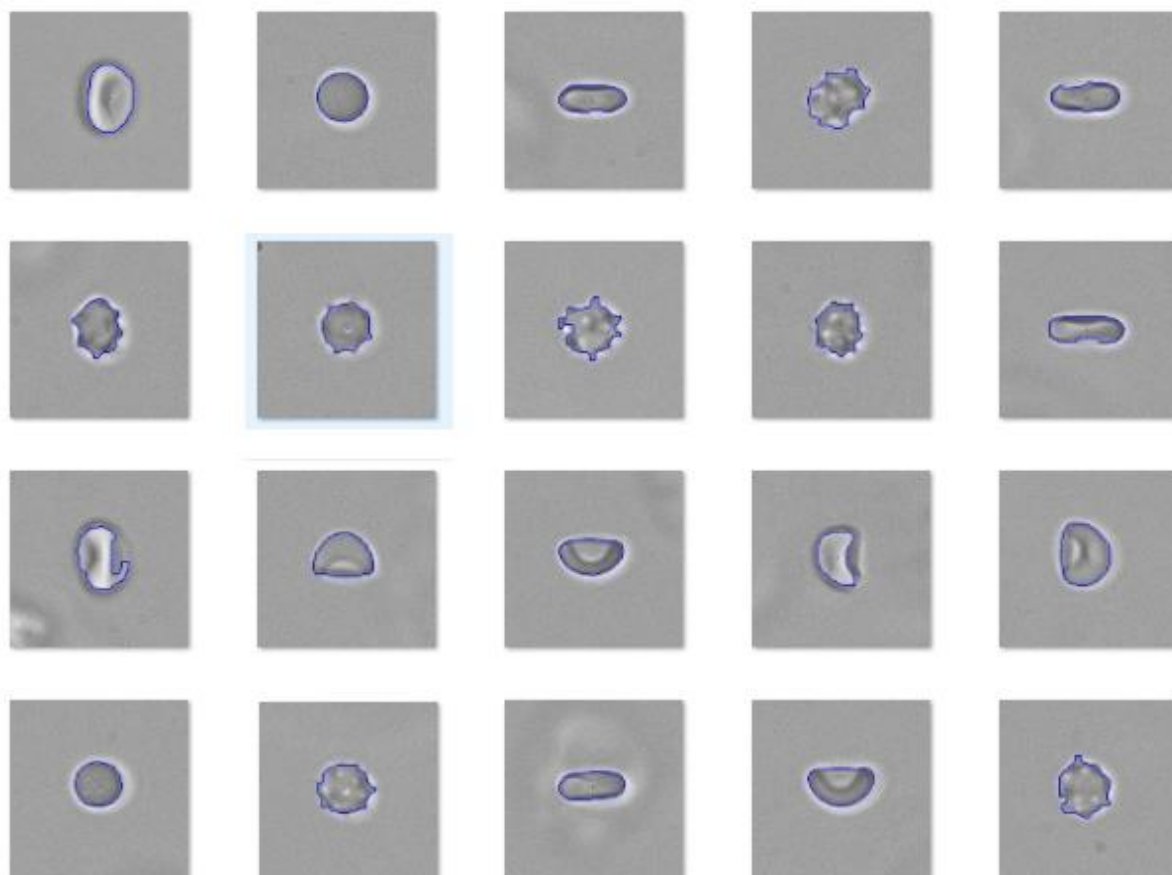


Fig. A-1 Examples of the segmentation results after the contour fitting process (see corresponding section) for the three morphological classes (D, E and S). Cell micrographs were generated from real moving cells captured with in situ microscopy. Discocytes exhibit different orientations.

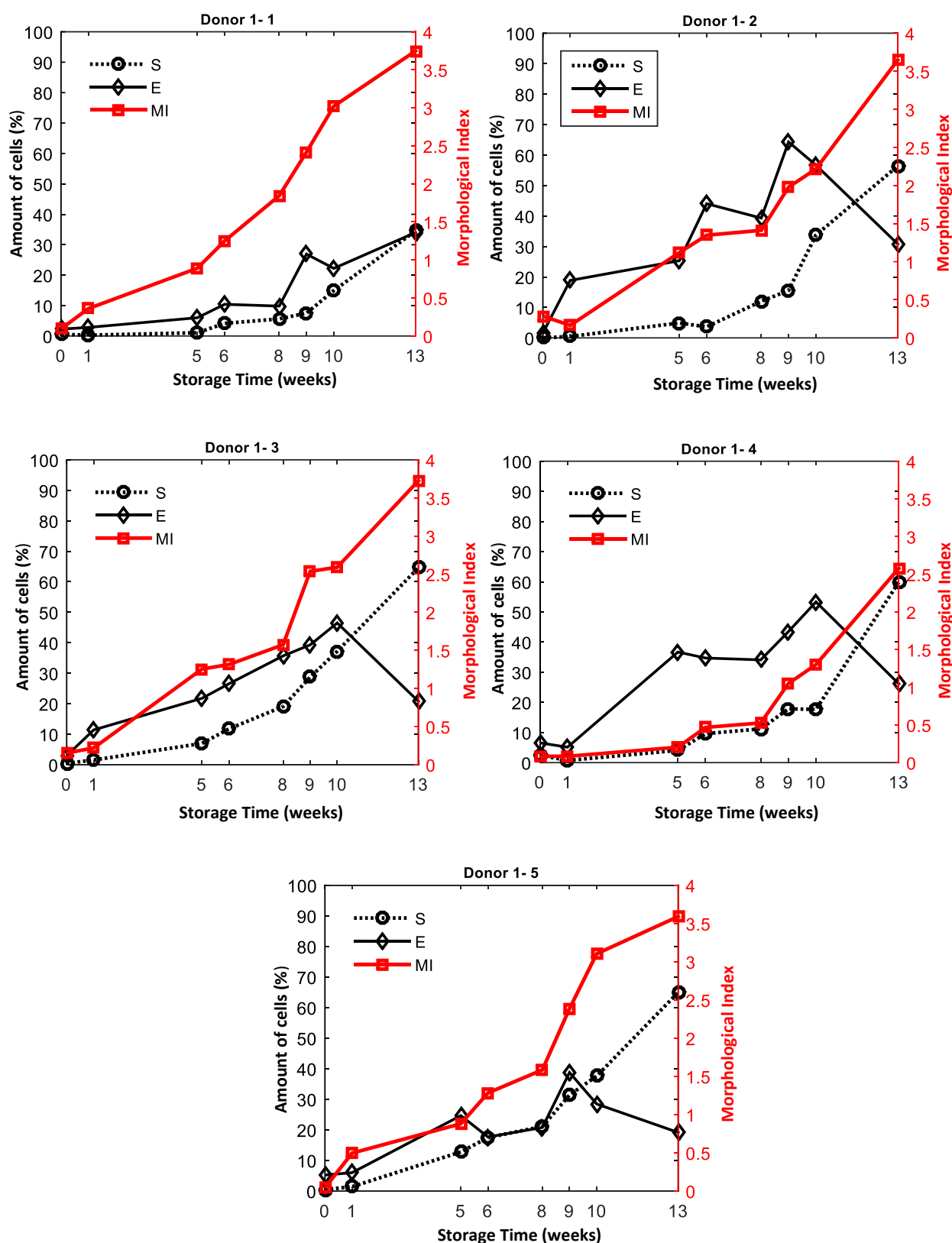
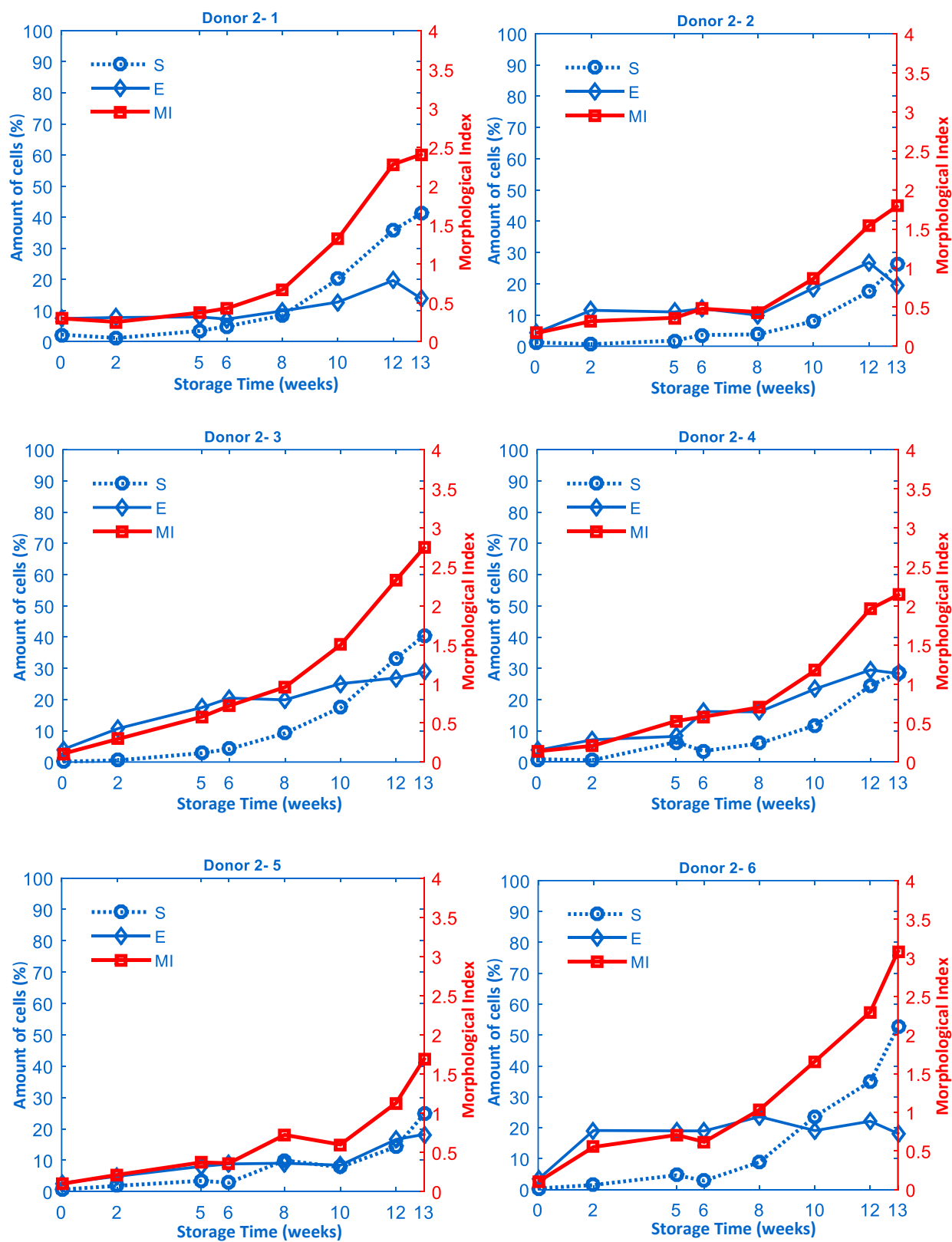


Fig. A-2. Damage curves (E, S and MI) of RBC units over 13 weeks corresponding to the donor group 1 (five donors).

Group 2.



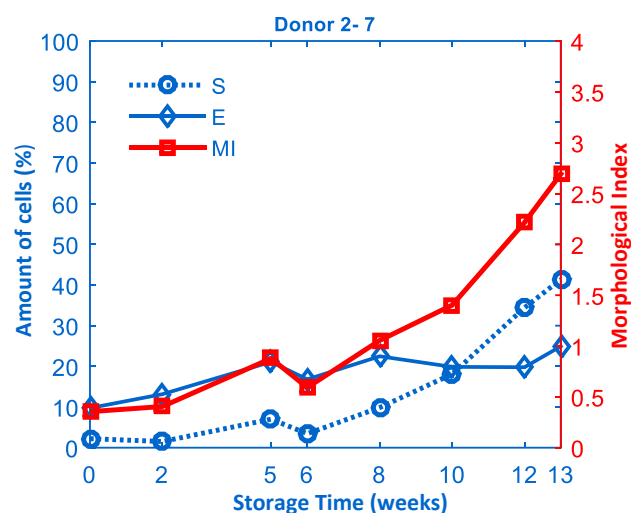
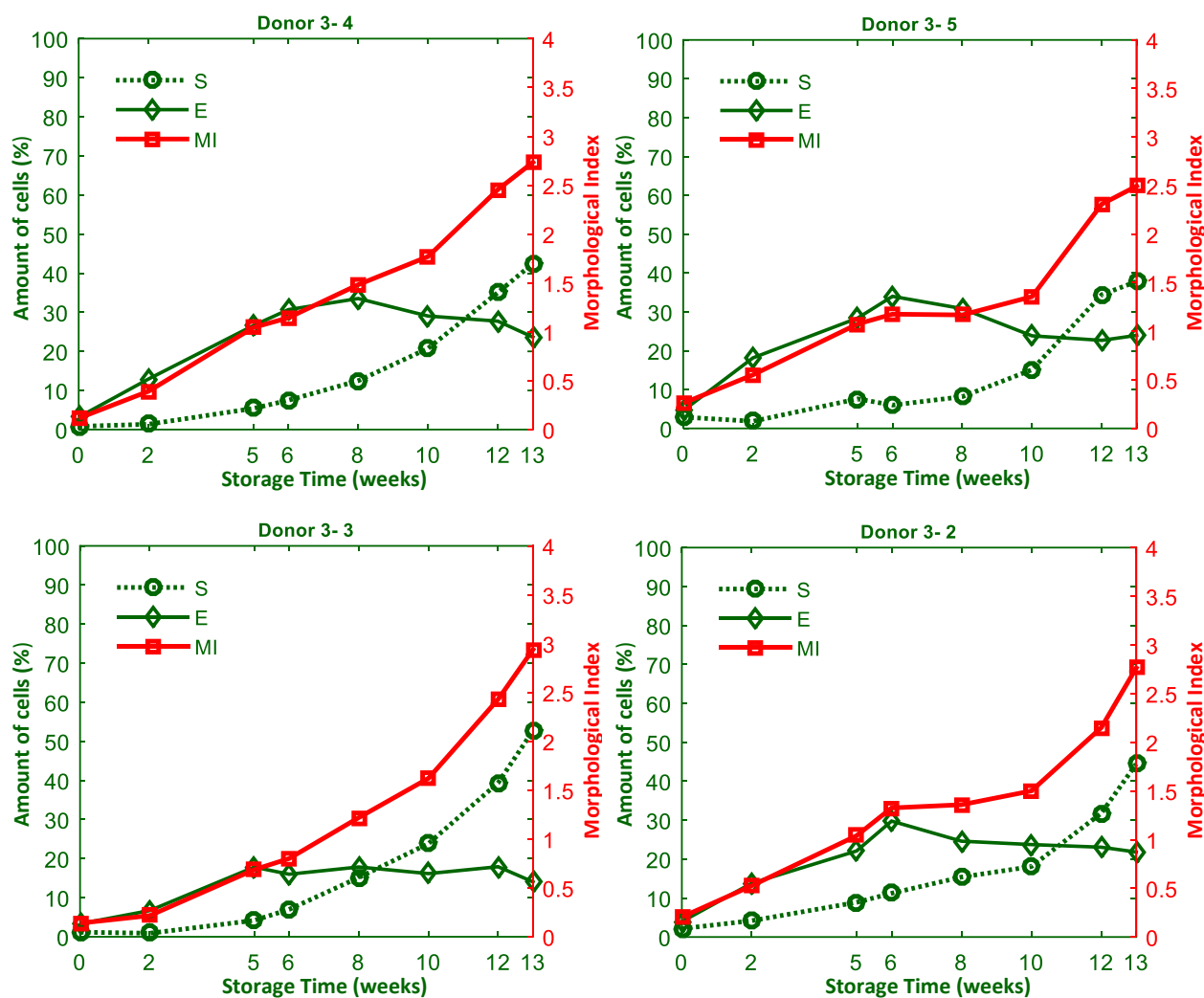


Fig. A-3. Damage curves (E, S and MI) of RBC units over 13 weeks corresponding to the donor group 2 (seven donors)



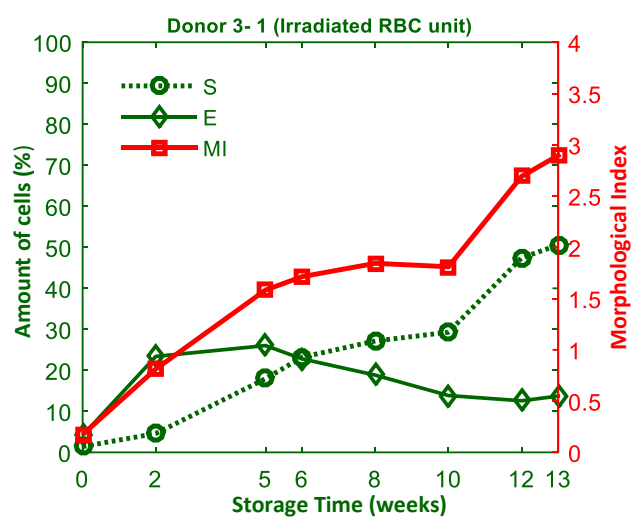


Fig. A-4. Damage curves (E, S and MI) of RBC units corresponding to the donor group 3.

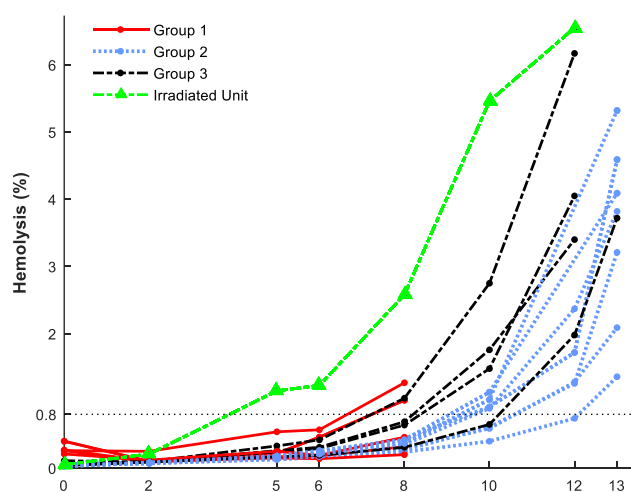


Fig A-5. Full progress of hemolysis over storage time for all RBC units of the three donor groups

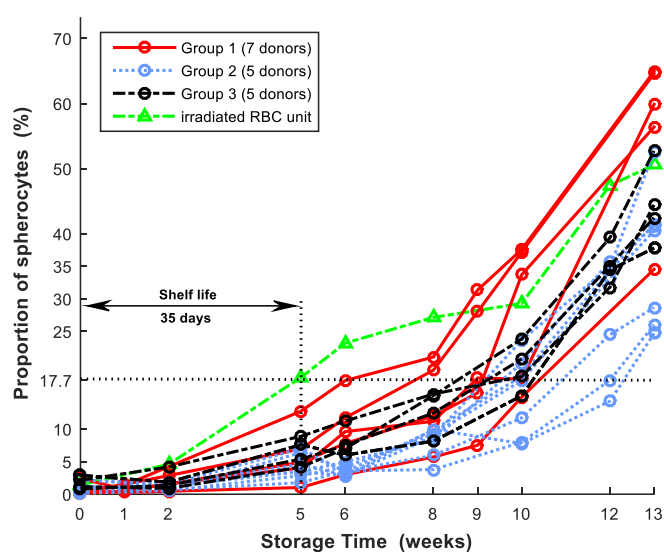


Fig A-6. Full progress of S-percentages over storage time for all RBC units of the three donor groups

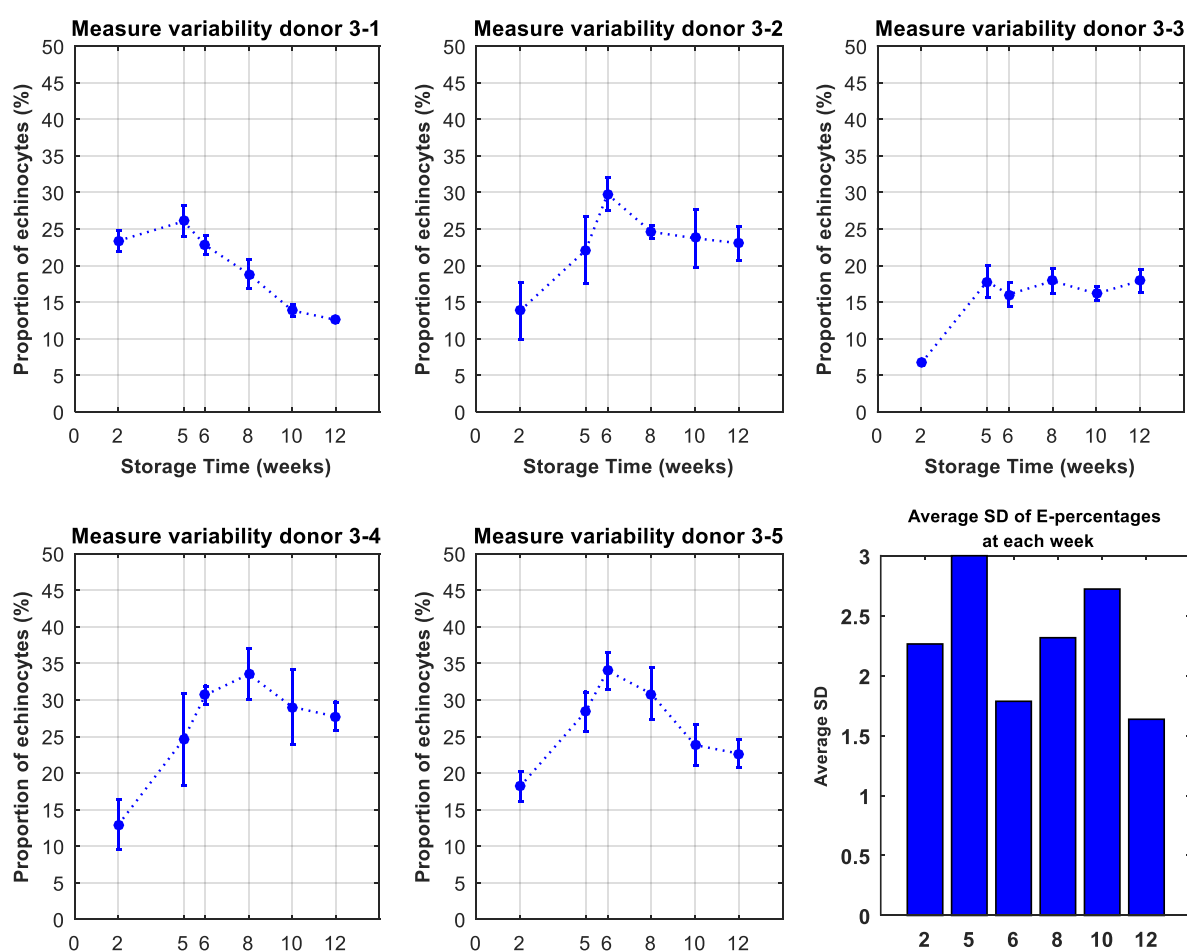


Fig. A-7. Measurement variability of E-percentages during the monitoring of five RBC units. Curves connect the mean values of the three-replicate measurements. Vertical bars along the curves represent the corresponding standard deviation. Bar diagram shows the average SD at each week.

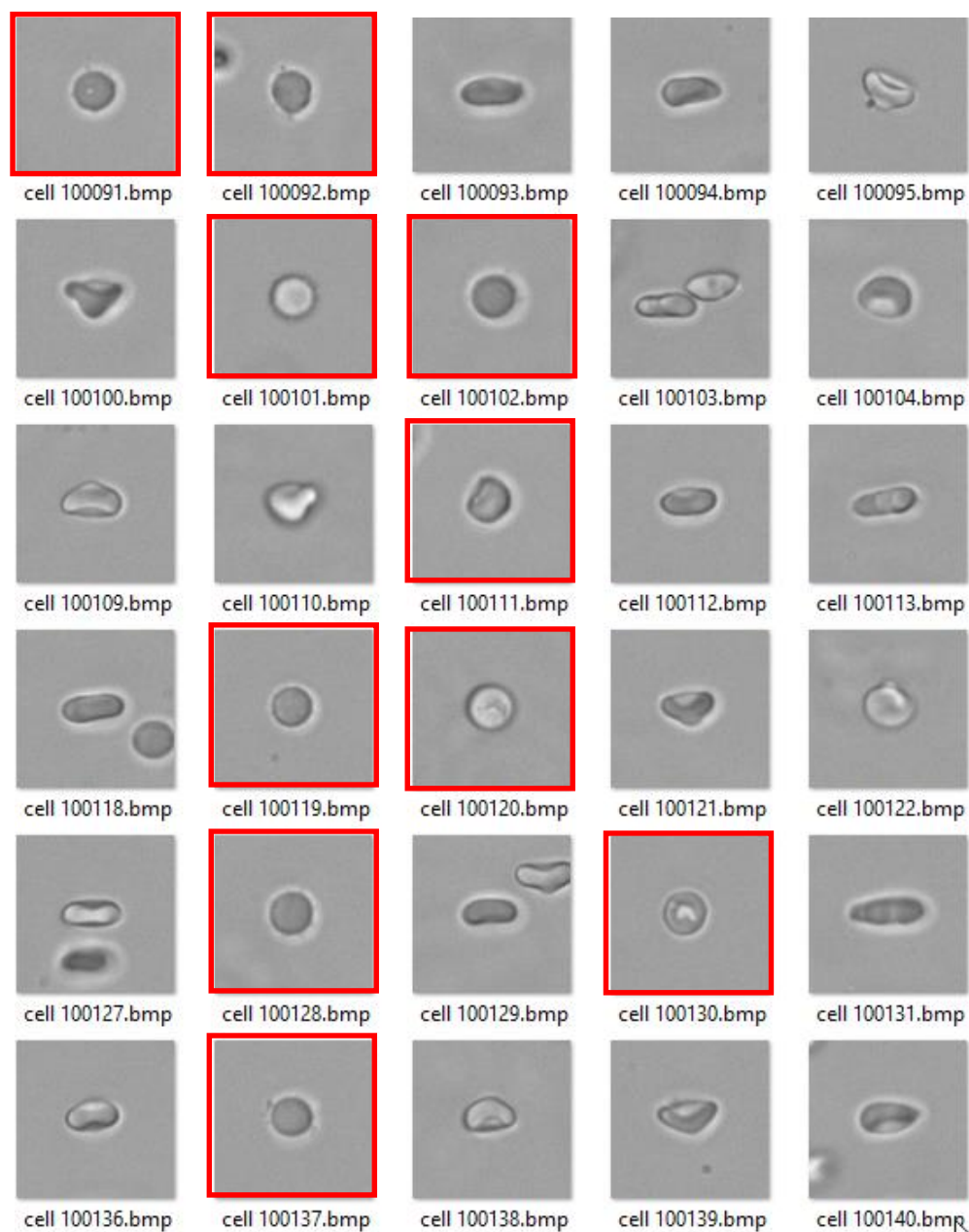


Fig. A-8. Examples of imaged RBCs after induced thermal shock (20min @44°C) in waterbed. Spherocytosis appears after the shock (micrographs with red outlines)

8 CURRICULUM VITAE

Diego Sierra

Born on 26.02 in Bogotá, Colombia

Education

- | | |
|-------------------------|-----------------------------------------------------------------------------------------------------------------------------|
| 9/2013 - 10/2016 | Ph.D – Heidelberg University
Medical Faculty Mannheim, Institute for Transfusion Medicine and Immunology. Germany |
| 03/2009 - 8/2011 | Master of Science in Information Technology
Mannheim University of Applied Sciences, Germany |
| 8/2001 – 2/2006 | Bachelor of Electronic Engineering
Pontificia Universidad Javeriana, Colombia |
-

Work History

- | | |
|-------------------------|------------------------------------------------------------------------------------------------------------------------------------------------------------------------------------------------------------------------------------------------------------------------------------------------------------------------------------------------------------------------------------------------------------------------------------------------------------------------------------------------------------------------------|
| 11/2016 - 4/2017 | Post-doctoral Researcher , Universitätsklinikum Mannheim, Institute for Transfusion Medicine and Immunology. Germany

Clinical data analysis for validation of an image-based blood diagnosis. <ul style="list-style-type: none">○ Statistical data analysis from experimental measurements. (Data-Mining: statistische Analyse, Assoziation- und Regressionsanalyse).○ Data Visualisation (Power BI)○ Software Development (MATLAB-C#) for real-time blood measurement. |
|-------------------------|------------------------------------------------------------------------------------------------------------------------------------------------------------------------------------------------------------------------------------------------------------------------------------------------------------------------------------------------------------------------------------------------------------------------------------------------------------------------------------------------------------------------------|

04/2013 - 10/2017 **Research Associate**, Institute of Molecular and Cell Biology - Mannheim University of Applied Sciences, Germany

- Data-Mining (patter recognition: Clustering, ID3 Classification).
- Statistic data analysis (correlation and regression analysis).
- Image processing – algorithm development (feature extraction).
- Development of a micro-hydraulic system for cell imaging.
- 3D Modeling (AutoCAD) – microscope system construction.

10/2009 - 8/2011 **Research Associate**. Institute of Digital Technology- Mannheim University of Applied Sciences, Germany.

Development of image-based methods for automatic analysis of microscope images.

- Computer-Vision programming, Object detection (C++, OPEN CV).
- Software development (C#)
- Pattern Recognition (MATLAB), Classification through SOM neuronal networks.

Publications

- | | |
|------|------------------------------------------------------------------------------------------------------------------------------------------------------------------------------------------------------------------|
| 2017 | Flow morphometry to assess the red blood cell storage lesion. <i>Cytometry Part A</i> . 2017; DOI: 10.1002/cyto.a.23127 |
| 2016 | Image processing for identification and quantification of filamentous bacteria in in situ acquired images. <i>BioMed Eng OnLine</i> . 2016;15:64, DOI: 10.1186/s12938-016-0197-7 |
| 2016 | In situ microscopy as a tool for the monitoring of filamentous bacteria: a case study in an industrial activated sludge system dominated by <i>M. parvicella</i> . <i>Water Sci Technol</i> . 2016;73(6):1333-40 |
| 2015 | Automated microscopic evaluation of Red Blood Cell storage lesion, Transfusion Medicine and Hemotherapy 2015;42 (suppl 1) DOI:10.1159/000438503 FV-10-4 |

9 ACKNOWLEDGMENTS

This project was carried out during 2013-2016 at the Faculties of Information Technology and Biotechnology, Mannheim University of Applied Science and at the quality laboratory of the Blood Donor Service Mannheim.

This work would not have been possible without the funding of the Ministry of Science, Research and Arts Baden Württemberg as well as the Albert-and-Anneliese-Konanz Foundation of the Mannheim University of Applied Sciences.

I owe my deepest gratitude to my supervisor Prof. Dr. rer. nat. Karen Bieback for proposing the topic of this study and for the opportunity to carry out this interesting doctoral research. Her willingness to resolve all concerns and provide promptly all necessary means for the attainment of this project were an invaluable help. Besides this, her optimism and uncomplicated approaches created an extraordinary work atmosphere.

I also owe a great debt of gratitude to Prof. Dr. Phillip Wiedemann for the excellent conduction of all instances of this project. His structural vision to coordinate the academic and operational issues were essential for the development of this project. In addition, he provided me valuable support in all concepts related with cell biology.

I am deeply grateful to Prof. Dr. Hajo Suhr at the Mannheim University of Applied Science for the opportunity to work with in situ microscope in his laboratory during the last years. His teachings helped me not only achieve analytical and scientific thinking but also grow as person.

I want to express my gratitude to Prof. Dr. med. Harald Klüter for letting me carry out this PhD project in his institute. Furthermore, I owe gratitude to Prof. Dr. Karin Janetzko for providing the expertise of her laboratory in the area of hematology and quality control in the Blood Donor Service Mannheim. I also want to thank Dr. Kathryn Melzak at the Karlsruhe Institute of Technology for her great contribution to the understanding of the erythrocyte biology.

I wish to thank Ms. Kirsten Fischer and all the staff of the quality control laboratory of the Blood Donor Service Mannheim for performing the experiments, the biochemical measurements and the logistics to carry out the monitoring of the RBC units. In the same way, I am indebted to Mr. Peter Schneider for his invaluable help with all hardware and electronic related questions throughout this project.

I would like to thank Ms. Stefanie Uhlig at the institute of Transfusion Medicine and Immunology, Medical Faculty Mannheim, for the support with flow cytometry measurements during the initial phase of this project.